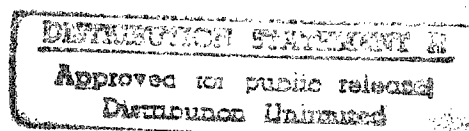


The Pennsylvania State University
The Graduate School
College of Earth and Mineral Science

**MICROSTRUCTURAL DEVELOPMENT IN AL-LI-CU-MG
ALLOYS AND METAL MATRIX COMPOSITES**

A Thesis in
Materials Science and Engineering
by
Xiaoli Tang



Submitted in Partial Fulfillment
of the Requirements
for the Degree of

Doctor of Philosophy

December 1995

19970602 020

The Pennsylvania State University
The Graduate School
College of Earth and Mineral Science

**MICROSTRUCTURAL DEVELOPMENT IN AL-LI-CU-MG
ALLOYS AND METAL MATRIX COMPOSITES**

A Thesis in
Materials Science and Engineering
by
Xiaoli Tang

Submitted in Partial Fulfillment
of the Requirements
for the Degree of

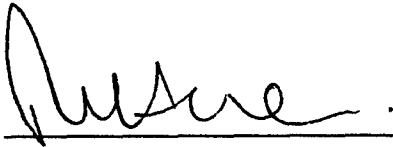
Doctor of Philosophy

December 1995

DTIC QUALITY INSPECTED 1


We approve the thesis of Xiaoli Tang.

Date of Signature



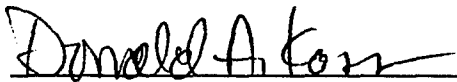
Paul R. Howell
Professor of Metallurgy
Thesis Advisor
Chair of Committee

9/12/95



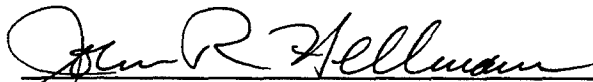
William R. Bitler
Professor of Metallurgy

12 September 1995



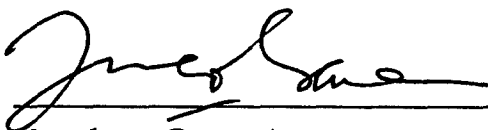
Donald A. Koss
Professor of Materials Science and Engineering

9/12/95



John R. Hellmann
Associate Professor of Ceramic Science and Engineering

13 September 1995



Kwadwo Osseo-Asare
Professor of Metallurgy
Professor in Charge of Metals Science and Engineering Option

9/12/95

ABSTRACT

The aging responses of both an 8090 alloy and a SiC reinforced 8090 alloy matrix composite, at 190°C, have been fully characterized for the first time using various analytical techniques. Two stage hardening was observed in both materials and somewhat unexpectedly, the aging response of the composite was unchanged as compared to the unreinforced 8090 alloy. Microstructural development during the aging of both materials was studied using electron microscopy and differential scanning calorimetry (DSC). Transmission electron microscopy (TEM) examination indicated that the δ' phase (Al_3Li) and the S' phase (Al_2CuMg) were the two principal strengthening phases in both materials. These two phases formed at different stages during aging and caused the two stage strengthening. Although the precipitation of the δ' phase was not affected by the high density of dislocations in the composite, acceleration of the S' precipitation was indicated by DSC.

The dislocation distribution in the composite was quantitatively compared with that in the unreinforced 8090 alloy. The addition of SiC to the 8090 alloy caused a highly non-uniform dislocation distribution in the composite. This non-uniform dislocation distribution is directly responsible for the unchanged aging response in the composite as indicated by microhardness tests.

Grain boundary and SiC/matrix interfacial microstructural development in the composite was studied using TEM. The T2 (Al_6CuLi_3) phase was found at both grain boundaries and SiC/matrix interfaces and the T2 phase caused δ'

precipitate free zones along these interfaces. The distribution of the S' phase was less affected by the precipitation at grain boundaries and the SiC/matrix interfaces. However, the depletion of vacancies along both grain boundaries and SiC/matrix interfaces eliminated S' nucleation sites and decreased precipitation of the S' phase in the vicinities of both these interfaces.

The precipitation behavior of the S' phase was studied in detail. S' precipitates were observed as corrugated sheets nucleated at dislocations and dispersed laths within the matrix. According to the morphology and the preferential nucleation sites, the S' precipitates in Al-Li-Cu-Mg alloys have been unambiguously classified as type A, B and C. Type A precipitates nucleate at dislocations and exhibit a "sheet" morphology, type B likely nucleate at vacancy clusters and exhibit the lath morphology, type C nucleate at δ' /matrix interfaces at the latter aging stage and are distributed uniformly within the matrix as fine laths.

The atomic matching across S'/ α interfaces was re-evaluated. The results indicate that the S'/ α interfaces are coherent at the $(010)_{S'}/(021)_{\alpha}$ interface and semi-coherent at the $(001)_{S'}/(0\bar{1}2)_{\alpha}$ interface. As a result, the S' grows preferentially along $[100]_{S'}$ direction and exhibits a lath morphology.

Dislocation helices and loops were observed in the 8090 alloy which had been naturally aged for ~ 6 months, although the strong affiliation between Li atoms and vacancies limits the mobility of vacancies and eliminates dislocation helices and loops in the as-quenched materials. The observation of e.g., loops in naturally aged material indicates that vacancy condensation is not negligible after long time natural aging. Unlike the dislocation loops observed in other aluminum alloys, which lie on $\{110\}$ plane, the loops in the present study lie predominantly on $\{210\}$ planes. It has been suggested

that prismatic loop glide driven by the precipitation of S' precipitates nucleated at loops is the cause of these {210} loops. It is also suggested that {210} loops may be unique to the Al-Li-Cu-Mg alloys.

TABLE OF CONTENTS

LIST OF FIGURES	x
LIST OF TABLES	xv
GLOSSARY	xvi
ACKNOWLEDGMENTS	xviii
CHAPTER 1. INTRODUCTION	1
1.1. BACKGROUND	1
1.2. RESEARCH OBJECTIVES	3
1.3. ORGANIZATION OF THE THESIS	4
1.4. REFERENCES	4
CHAPTER 2 AGING RESPONSE OF 8090 ALLOY AT 190°C	6
2.1. BACKGROUND	6
2.2. EXPERIMENTAL	9
2.2.1. Hardness Test	10
2.2.2. Microstructural Examination	10
2.3. RESULTS	11
2.3.1. Aging Response Characterized by Hardness Change	11
2.3.1.1. Microhardness	11
2.3.1.2. Macrohardness	13
2.3.2. Microstructural Development at 190°C	13
2.3.2.1. The δ' Phase	13
2.3.2.2. Quantitative Analysis of the δ' Phase	19
2.3.2.3. The S' Phase	21

2.3.2.4. Other Phases	32
2.3.2.5. Grain Boundary Structural Development	40
2.4. DISCUSSION	51
2.4.1. Aging Response	51
2.4.2. Principal Strengthening Precipitates in 8090 Alloy	53
2.4.2.1. The δ' Phase Strengthening Potency	53
2.4.2.2. Strengthening Effects of the S' Phase	57
2.4. CONCLUSIONS	62
2.5. REFERENCES	63
CHAPTER 3 A STUDY OF THE PRECIPITATION BEHAVIOR OF THE S' (Al_2CuMg) PHASE	67
3.1 BACKGROUND	67
3.2 INTERFACIAL COHERENCY AND THE GEOMETRIC SHAPE OF THE S' PHASE	68
3.2.1 S'/ α Interfacial Coherency	68
3.2.2. Kinetic Shape of the S' Phase	81
3.3. S' NUCLEATION AT DISLOCATIONS	81
3.3.1. S' Variants Nucleated at a Dislocation	83
3.3.2. S' Precipitation at Dislocation Loops	84
3.3.2.1 Dislocation Loop Orientation	84
3.3.2.2. Relative Orientation of S' Precipitates with respect to Dislocation Loops	92
3.4. MULTIPLE S' PRECIPITATION MODES	94
3.5. CONCLUSIONS	104
3.6. REFERENCES	106

CHAPTER 4 AGING RESPONSE OF A PARTICULATE REINFORCED METAL

MATRIX COMPOSITE	108
4.1. BACKGROUND	108
4.2. AGING KINETICS OF THE COMPOSITE	111
4.2.1. Experimental	111
4.2.2. Results	113
4.3. DISLOCATION CHARACTERISTICS OF THE COMPOSITE	115
4.3.1. Experimental	115
4.3.2. Results	118
4.3.2.1. Dislocation Distribution	118
4.3.2.2. Dislocation Density Measurement	123
4.4. PRECIPITATION CHARACTERISTICS OF THE COMPOSITE	124
4.4.1. Precipitation of the δ' Phase	124
4.4.2. S' Precipitation	127
4.5. DIFFERENTIAL SCANNING CALORIMETRY (DSC) ANALYSIS	130
4.5.1. Experimental	133
4.5.2. Results	133
4.6. GRAIN BOUNDARY AND SiC/ α INTERFACIAL MICROSTRUCTURAL CHANGES	139
4.6.1. Experimental	139
4.6.2. Results	139
4.6.2.1. Interfacial precipitation and δ' PFZs	140
4.6.2.2. S' Distribution along SiC/ α Interfaces	142
4.7. DISCUSSION	142
4.7.1. Aging Kinetics of the Composite	142
4.7.2. Dislocation Distribution in the Composite	149

4.7.3. Precipitation in the Composite	152
4.7.3.1. δ' Precipitation	152
4.7.3.2. S' Refinement	153
4.7.4. Precipitation Sequence	154
4.7.5. Interfaces	157
4.8. CONCLUSIONS	158
4.9. REFERENCES	159
CHAPTER 5 SUMMARY AND FUTURE WORK	163
5.1 SUMMARY	163
5.2 FUTURE WORK	165
APPENDIX I QUANTITATIVE ANALYSIS OF THE δ' PHASE IN THE 8090 ALLOY	168
APPENDIX II ELECTRON DIFFRACTION PATTERNS AND INDEXING OF THE S' PHASE	173
APPENDIX III TRACE ANALYSIS	179

LIST OF FIGURES

Figure 2.1	Microhardness of the 8090 alloy at different aging time at 190°C	12
Figure 2.2	Macrohardness change upon aging at 190°C	14
Figure 2.3	δ' precipitates in the 8090 alloy after 1 hour aging	15
Figure 2.4	δ' phase coarsening with the increase of aging times	16-18
Figure 2.5	Average δ' precipitate size as a function of aging time	20
Figure 2.6	δ' coarsening kinetics	22
Figure 2.7	δ' volume number density as a function of aging time	23
Figure 2.8	δ' phase volume fraction as a function of aging time	23
Figure 2.9	S' precipitates after 16 hours of aging	24
Figure 2.10	Morphology and orientation of a S' lath	27-28
Figure 2.11	Three types of S' precipitates	29
Figure 2.12	S' precipitates nucleated at dislocations	30
Figure 2.13	S' growth kinetics at 190°C	33
Figure 2.14	S' and T ₁ in an 8090 sample aged for 120 hours	34
Figure 2.15	[112] _α stereographic projection showing the orientation relationship between the S' phase and the T ₁ phase	35
Figure 2.16	T ₂ phase and the associated δ' PFZs at a grain boundary	37
Figure 2.17	CBED pattern from the T ₂ phase	38
Figure 2.18	Decomposed T ₂ phase and the associated δ' PFZ	39
Figure 2.19	δ precipitate and the CBED pattern	41
Figure 2.20	δ precipitate and SAD pattern	42
Figure 2.21	Grain boundary precipitates and δ' PFZ after 1 hour	43

Figure 2.22	Grain boundary precipitates and δ' PFZ after 20 hours	44
Figure 2.23	δ' PFZ development as a function of aging time	46
Figure 2.24	S' precipitation and δ' PFZ in the vicinity of a grain boundary	47
Figure 2.25	Dislocation loop and S' free zones along grain boundaries . . .	48
Figure 2.26	δ' PFZs and the distribution of S' phase after 120 hours . . .	49-50
Figure 2.27	Converted results from microhardness to HRB	52
Figure 2.28	Strengthening contribution of the δ' phase to CRSS	56
Figure 2.29	Slip line trace in a sample aged for 12 hours	58
Figure 2.30	S' laths viewed with beam direction parallel to the longitudinal axis of the precipitates	60
Figure 3.1	Model of a S' lath	69
Figure 3.2	Unit cells of the S' phase and the α matrix	73
Figure 3.3	$(100)_S / (100)_\alpha$ atom maps	74
Figure 3.4	$(001)_S / (0\bar{1}2)_\alpha$ atom maps	75
Figure 3.5	$(010)_S / (021)_\alpha$ atom maps	76
Figure 3.6	High magnification image of the S' precipitates at a dislocation	79
Figure 3.7	Broad faces and growth ledges in S' precipitates	80
Figure 3.8	S' sheet formed by S' nucleated at dislocations	82
Figure 3.9	Upright view of S' precipitates nucleated at a dislocation loop	82
Figure 3.10	S' sheets parallel to dislocation loop plane, $(110)_\alpha$	85
Figure 3.11	S' sheets parallel to $(210)_\alpha$ loop plane	87
Figure 3.12	Relation of the dislocation loops on (210) planes and dislocation helices	89
Figure 3.13	Loops on $(011)_\alpha$ and $(0\bar{1}2)_\alpha$ planes	90
Figure 3.14	S' sheets inclined to dislocation loops	91

Figure 3.15	Model of S' nucleated at dislocation loops on $(110)_\alpha$ or $(210)_\alpha$ planes	93
Figure 3.16	Single variant of S' precipitates formed at $\{210\}_\alpha$ loops	95
Figure 3.17	S' precipitates at a dislocation loop viewed at different orientations by tilting the sample	96
Figure 3.18	Upright view of S' precipitates of type B	98
Figure 3.19	Microstructure of a as-quenched 8090 sample	99
Figure 3.20	Dislocations in a 8090 sample naturally aged for 6 months	99
Figure 3.21	S' precipitates of type A and type C after 48 hour aging	101
Figure 3.22	S' precipitates of type A nucleated at a dislocation helix and type C in the background	103
Figure 3.23	Small dark regions are shown to be precipitate laths/rods	105
Figure 4.1	SEM image of the 8090/SiC composite	112
Figure 4.2	Aging kinetics (represented by microhardness changes) of the matrix for both the composite and the control alloy	114
Figure 4.3	Macrohardness changes upon aging at 190°C for the composite and the control alloy	114
Figure 4.4	Comparison of hardness change of the pre-deformed 8090 material with the non-deformed material	116
Figure 4.5	Dislocation distribution in the matrix of the composite between two SiC Particles	119
Figure 4.6	High magnification WB image of dislocations in the vicinity of a SiC particle	120
Figure 4.7	Dislocations in a SiC free region of the composite	121
Figure 4.8	Dislocations in the control alloy	122
Figure 4.9	δ' radius, \bar{r} , as a function of $\sqrt[3]{t}$	126

Figure 4.10	S' precipitates in an area next to a SiC particle after 4 hours of aging	128
Figure 4.11	S' precipitation behavior changes as the distance from the SiC/matrix interface increases	129
Figure 4.12	S' precipitates in the pre-deformed 8090 sample after 25 hours of aging	131
Figure 4.13	S' precipitates in the vicinity of a SiC particle in the composite after 25 hours of aging	131
Figure 4.14	S' precipitates in a SiC free region of the composite after 25 hours of aging	132
Figure 4.15	S' precipitates in the control alloy after 25 hours of aging . . .	132
Figure 4.16	DSC thermogram of the as-quenched 8090 alloy	134
Figure 4.17	DSC thermogram of the as-quenched composite	136
Figure 4.18	DSC thermogram of the pre-deformed 8090 alloy	137
Figure 4.19	DSC thermogram of the 8090 alloy naturally aged for 26 hours	138
Figure 4.20	δ' PFZs in the composite after 1 hour aging	141
Figure 4.21	Precipitates at a high angle grain boundary in the composite after 1 hour aging	143
Figure 4.22	SiC/ α interface after 1 hour aging	143
Figure 4.23	Precipitation at different type of triple junctions	144
Figure 4.24	Comparison of the distribution of the δ' phase and the S' phase near a SiC/ α interface	145
Figure 4.25	S' precipitation in the control alloy after 4 hours of aging . . .	148
Figure 4.26	S' precipitates in a 8090 sample aged for 16 hours at 190°C immediately after solution treatment	150
Figure 4.27	Plastic deformation zones in the matrix around reinforcement	151

Figure I-1	δ' size distribution after 8 hour aging	169
Figure I-2	Illustration of the quantitative measurement of the δ' phase	170
Figure II-1	S' laths from groups I and II and the corresponding SAD pattern	174
Figure II-2	Simulated SAD pattern of S' laths including 8 variants lying normal to beam direction	175
Figure II-3	S' precipitates from all the 3 orientation groups	177
Figure II-4	Simulated SAD pattern of S' laths including all the 12 variants	178
Figure III-1	Relationship between the $\langle 100 \rangle$ projections and the plane of projection with $[\mathbf{B}] = [001]$	180
Figure III-2	Relationship between $\{hk0\}$ and $\langle hk0 \rangle$ projections and the plane of projection with $[\mathbf{B}] = [001]$	181
Figure III-3	$\{110\}$ plane orientation	183
Figure III-4	Projection orientation relationship of dislocation loops on $\{110\}$ planes and $\{11L\}$ planes	184

LIST OF TABLES

Table 2.1	δ' Diameter at Different Aging Time	19
Table 2.2	Orientation of the 12 Variants of the S' Phase	26
Table 3.1	Quoted Misfits between the S' Phase and the α Matrix	70
Table 3.2	Atoms in the S' Unit Cell	72
Table 3.3	Misfits between the S' Phase and the α Matrix along a, b and c Axes of the S' Phase	77
Table 4.1	Dislocation Densities	123
Table 4.2	δ' Precipitate Size Development	125
Table 4.3	δ' PFZ Development with Aging Times	140

GLOSSARY

artificial aging: in the present study, artificial aging was carried out at 190°C.

natural aging: aging at room temperature.

β' phase: Al_3Zr

BF: bright field.

CBED: convergent beam electron diffraction.

CDF: centered dark field.

composite: a 8090/SiC composite containing ~ 17%vol SiC particles.

control alloy: the unreinforced 8090 alloy which has been naturally aged for ~ 6 months.

CRSS: critical resolved shear stress.

δ phase: AlLi .

δ' phase: Al_3Li

DSC: differential scanning calorimetry.

8090 alloy: an aluminum alloy with the nominal composition of Al-2.4w/oLi-1.3w/oCu-0.8w/oMg-0.12w/oZr.

GP zone: solute segregated zone.

GPB zone: Al-Cu-Mg rich zone.

HREM: high resolution electron microscopy.

HVEM: high voltage electron microscopy.

non-deformed material: solution treated and artificially aged at 190°C for various times without natural aging.

PFZ: precipitate free zone.

pre-deformed material: solution treated, deformed to ~ 3% and immediately artificially aged at 190°C for various times.

S' phase: Al_2CuMg .

SAD: selected area diffraction.

T1 Phase: Al_2CuLi .

T2 phase: Al_6CuLi_3 .

T6 treatment: solution heat treated and artificially aged.

TEM: transmission electron microscopy.

θ' phase: Al_2Cu

WB: weak beam.

ACKNOWLEDGMENTS

I would like to express my sincere gratitude and appreciation to the members of my thesis committee for their suggestion and guidance during the course of this research. In particular, I would like to thank my thesis advisor, Dr. Paul. R. Howell for his support and encouragement as well as his keen scientific input.

Special thanks are extended to my colleagues: Atul S. Ramani, Marjorie McGaughey, Dana Goto and John Breedis. Their unselfish help during the past 4 years is greatly appreciated. Acknowledgments are also due to Tom Rusnak for his patient technical assistance.

This research program is supported by the Office of Naval Research. I am grateful for the financial assistance from this office as well as from the COOP funding of the Metals Science and Engineering Program of The Pennsylvania State University.

Finally, I would like to thank my parents and my sister for all the love they have given to me. Without their support and understanding, I would not be able to present this thesis here.

CHAPTER 1

INTRODUCTION

1.1. BACKGROUND

The effort to bring aluminum-lithium alloys to commercialization has been considered as the single largest alloy-development effort in the history of aluminum metallurgy. It has been known for many years that as an alloying element in aluminum alloys, lithium has an extraordinary effect on reducing material density, enhancing precipitation hardening capacity, and most remarkably, significantly increasing the elastic stiffness. In as early as 1957, Alcoa developed the Al-1.1Li-4.5Cu-0.5Mn-0.2Cd alloy X2020 based on LeBaron's 1945 patent [1], which is considered the earliest commercialized Al-Li alloy. However, the early development of Al-Li alloys was stranded by Al-Li alloys' poorest fracture-toughness of all commercially available aerospace alloys.

The great impetus for the development of Al-Li alloys came in late 70s. The increase in the price of jet fuel provided the primary driving force for the weight reduction of aerospace vehicles. With the recognition that the reduction in density of materials has a bigger influence on reducing the weight of aerospace vehicles than any other mechanical property improvement, there was a growing belief that polymer-matrix composites might substitute for aluminum alloys as the primary materials in aerospace industry, if significant advancement in aluminum metallurgy did not occur. This stimulated the studies on the development of aluminum-lithium alloys

which have improved properties and might finally replace conventional aluminum alloys in aerospace industry and anywhere where weight saving is a concern. In the last two decades, significant progress has been made in aluminum-lithium alloys. Through proper alloying and thermomechanical processing, mechanical properties, especially fracture toughness of these materials have been improved greatly. This leads to many applications of these alloys. Among these, products from Al-Li-Cu-Mg alloys, such as 2091, 8090, 8091 and weldalite (2095) have received the most attention [2].

The density of 8090 alloy (nominal composition of Al-2.4Li-1.3Cu-0.8Mg-0.12Zr) is the lowest (2.54 g/cm^3) in Al-Li alloys. The Young's modulus of 8090 alloy is as high as 80 GPa [3] vs. the modulus of 69 GPa in 6061 alloy. Through proper thermomechanical processing, a large variety of moderate-to high strength-level tempers can be obtained. This alloy is reported to have an outstanding plane-stress fracture toughness, even superior to 2024-T351 when at an equivalent strength level [4]. Therefore, this alloy has a wide application in aerospace and other similar industries [5,6].

With the incorporation of reinforcements, aluminum alloys can be further strengthened without a significant rise of the density. According to the form of the reinforcement, composites are classified as continuously reinforced which have continuous filaments as the reinforcement, and discontinuously reinforced which could contain either whiskers or particulates in the matrix. Discontinuously reinforced composites have the advantages over filament reinforced materials, such as less anisotropic properties, easy to process and form by traditional fabrication and machining methods. These make discontinuously reinforced composites the most available composites for practical applications.

Silicon carbide discontinuously reinforced aluminum alloys show promise for their high stiffness, high strength and low density. These composites also have the advantages of excellent thermal conductivity, reasonable cost, high machinability and good workability. SiC is chemically compatible with aluminum and can form an adequate bond without developing intermetallic phases at the SiC/matrix interfaces.

1.2. RESEARCH OBJECTIVES

The overall goal of this thesis study is to obtain an in-depth understanding of the aging behavior of a SiC particulate reinforced Al-Li-Cu-Mg alloy matrix composite. As is well known, the mechanical properties of discontinuously reinforced metal matrix composites largely depend on the properties of the matrix. In addition, the SiC/matrix interfacial properties play a critical role in determining the occurrence of fracture and the failure mode of the composites. The present study has been focused on the following aspects:

- (1) the aging kinetics of the composite as compared to the unreinforced alloy;
- (2) the change of precipitation behavior of various phases in metal matrix composites;
- (3) the dislocation distribution in metal matrix composites and its effect on different type of strengthening phases;
- (4) interfacial microstructural development during aging, including the precipitation at the SiC/matrix interfaces and the distribution of strengthening phases in the vicinities of the interfaces.

1.3. ORGANIZATION OF THE THESIS

The major research in the present study is presented in the following three chapters. Some of the experimental details are supplied in Appendices I, II and III. The Al-Li-Cu-Mg/SiC system was chosen for this thesis study because of its industrial application potential. The 8090 alloy is considered a good candidate with respect to the goal of this study, because it contains several types of strengthening precipitates and these precipitates exhibit different precipitation characteristics during aging. To fully understand the aging behavior of the metal matrix composite, the aging response and the associated microstructural development of the 8090 alloy were first characterized. The results on the aging behavior of the 8090 alloy are presented in Chapter 2. During the study on the aging behavior of the 8090 alloy, interesting features have been observed on the precipitation of one of the principal strengthening phases in the 8090 alloy, the S' (Al₂CuMg) phase. Chapter 3 is concerned with the details of the precipitation of the S' (Al₂CuMg) phase. Finally, the aging behavior of the 8090/SiC composite, the effect of the dislocation distribution on various precipitates and the SiC/matrix interfacial microstructure, are discussed in chapter 4.

1.4. REFERENCES

1. I. M. LeBaron: U.S. Patent no. 2,381,219, application date 1942, granted 1945.
2. R. H. Graham, R. J. Rioja and J. M. Newman: *Aluminum-Lithium*, Paper presented at 6th International Aluminum-Lithium Conference,

- M. Peter and P.-J. Winkler, eds., Garmisch-Partenkirchen, Germany, 1991, p15.
3. M. Hunt: *Mater. Eng.*, June, (1991), p27.
 4. R. Grimes, W. S. Miller and M. A. Reynolds: *Aluminum-Lithium Alloys, Design, Development and Application Update*, R. J. Kar, S. P. Agrawal and W. E. Quist eds., Proceeding of the 1987 Aluminum-Lithium Symposium, Los Angeles, CA, March 25-26, 1987, p41.
 5. P. O. Wakeling, S. D Forness, and E. A. W. Heckman: *ibid.*, p339.
 6. J. Waldman, R. Mahapatra, C. Neu, and A. P. Divecha: *ibid.*, p341

CHAPTER 2

AGING RESPONSE OF THE 8090 ALLOY AT 190°C

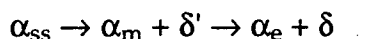
2.1. BACKGROUND

The mechanical properties of aluminum alloys can be adjusted significantly by different thermomechanical processes. Artificial aging is a frequently used method to modify the properties of these alloys and to achieve a desirable combination. Following solution treatment, the material is reheated to an appropriate temperature. As the microstructure changes, especially with the formation of different precipitates, the mechanical properties of the materials can vary over a large range. In Al-Li-Cu-Mg alloys, age hardening is usually carried out over the temperature range of 150-200°C in order to obtain desirable properties in a reasonable time period. The major microstructural changes in this temperature range have been the objectives of many previous studies.

In Al-Li alloys, the δ' phase (Al_3Li) is the primary phase when the Li content is > 7 at %. The δ' phase has the Li_2 structure and a very similar lattice parameter (4.01Å) as compared to the α matrix (4.05Å) [1]. δ' forms within the α matrix homogeneously with a cube-cube orientation relationship (OR) with respect to the matrix. The δ'/α interface has been examined using high resolution electron microscopy (HREM) and is fully coherent with ledges on the interface [2,3]. Although the δ' phase has been reported to form during quenching following solution treatment, both differential scanning calorimetry (DSC) and high resolution electron

microscopy (HREM) studies have suggested that the decomposition product of the supersaturated α matrix during quenching is a precursor to the δ' phase, which might be formed by congruent ordering [3,4]. During artificial aging, these ordered domains further decompose into spherical δ' precipitates through either classic nucleation [4-6] or spinodal decomposition [7-9] mechanisms. δ' precipitates contribute significantly to the precipitation hardening of Al-Li alloys and can be the primary source of high strength in these alloys. However, because these precipitates can be easily sheared during plastic deformation, the subsequent plastic deformation localization is a major factor responsible for the low ductility and low fracture toughness in Al-Li alloys.

The δ' phase is metastable in the Al-Li system. After holding at elevated temperature, the following transformation will occur:



where α_{ss} , α_m and α_e refer to the supersaturated, metastable and the equilibrium α solid solution, respectively. Although the δ (AlLi) phase is most frequently observed at grain boundaries, it also forms within the α matrix [10-12]. With the precipitation of the δ phase at grain boundaries, δ' precipitate free zones (PFZs) are observed in the vicinities of these boundaries. These soft PFZs are the locations where localized deformation can easily take place. The precipitation of the δ phase at grain boundaries has been proven to be the primary cause of the poor mechanical properties in Al-Li alloys [11].

In order to improve the ductility and fracture toughness of Al-Li alloys, Al-Li-Cu alloys (2090 type) and Al-Li-Cu-Mg alloys (8090 type) have been introduced, hoping that multiple precipitation will delay the formation of

grain boundary precipitates and reduce the localized deformation which is observed in binary Al-Li alloys. In Al-Li-Cu alloys, the θ' (Al_2Cu) and T_1 (Al_2CuLi) phases can be formed in addition to the δ' phase. The θ' phase is a metastable precipitate formed during artificial age treatment in Al-Cu alloys and Al-Li-Cu alloys with a high Cu:Li ratio. It has a tetragonal crystal structure with $a = b = 4.04\text{\AA}$, $c = 5.8\text{\AA}$ and tends to form as platelets with broad coherent interfaces on the $\{100\}$ planes of the matrix. It is the primary strengthening phase in Al-Cu alloys.

In Al-Li-Cu alloy with a high Li:Cu ratio, the T_1 phase will substitute for the θ' phase as the primary Cu bearing phase. The T_1 phase, an equilibrium phase in the Al-Li-Cu system, has a hexagonal structure and forms as platelets on the $\{111\}$ planes of the matrix. The T_1 phase is reported as a strong hardening agent in Al-Li-Cu alloys [13,14]. The precipitation of T_1 is suggested to be able to stabilize Li and Cu within the matrix, and hence delay the formation of grain boundary precipitates [15], such as, the δ phase and the T_2 (Al_6CuLi_3) phase.

The S' (Al_2CuMg) phase is expected to form in quaternary Al-Li-Cu-Mg alloys when the atomic Mg:Cu ratio is >3 . The S' phase has an orthorhombic crystal structure with $a = 4.00\text{\AA}$, $b = 9.23\text{\AA}$ and $c = 7.14\text{\AA}$. It nucleates within the matrix with a $\{210\}_\alpha$ habit plane and develops a lath-like morphology with the longitudinal axis parallel to the $\langle 100 \rangle$ directions of the matrix. The S' phase has a strong hardening potency and is reported to be able to disperse slip during plastic deformation more effectively than the T_1 phase [16,17].

Both the T_1 and S' precipitates are preferentially nucleated at dislocations and sub-boundaries. It has been shown that a stretch prior to aging can accelerate the precipitation of these two phases and promote the

strengthening process [16-21]. Although the preferential nucleation of T_1 at sub-boundaries has been reported to cause δ' PFZs, S' precipitation has no effect on the distribution of the δ' phase.

In common with the δ phase, the T_2 (Al_6CuLi_3) phase is an equilibrium phase which has been found at high angle grain boundaries as well as within grains in Al-Li-Cu alloys after holding at high temperature. In Al-Cu-Li-Mg alloys, it has been claimed that Mg can substitute some of Li in the T_2 phase and the precipitate may have a stoichiometry of $Al_6CuLi_{3-x}Mg_x$ [22], which sometimes is called the I phase [23]. The T_2 phase displays icosahedral symmetry and can be exclusively identified by the "forbidden" five-fold symmetrical diffraction pattern. The precipitation of the T_2 phase at grain boundaries has a detrimental effect on the mechanical properties by initiating intergranular fracture through either microvoid nucleation near these grain boundary precipitates [24] or microcrack nucleation in these precipitates [20].

Although the various precipitation reactions which could take place in Al-Li-Cu-Mg alloys during artificial aging have been extensively studied, the relationships between precipitation characteristics and the aging response of practical Al-Li-Cu-Mg alloys are not well understood. For example, the roles of specific strengthening precipitates at different aging stages have not been characterized in these alloys. Hence, prior to investigating the microstructure of the composite, the contributions of various phases to the aging response of an unreinforced 8090 alloy have been examined in detail.

2.2. EXPERIMENTAL

The material used for this study is a spray-formed 8090 alloy which has a nominal composition of Al-2.4Li-1.3Cu-0.8Mg-0.12Zr, corresponding to

Al-4%atLi-0.2%atCu-0.4%atMg-0.04%atZr. After solidification, the material was extruded to a ratio of 17:1 to eliminate the porosity.

The material was solution treated at 536°C for 45 minutes followed by ice-water quenching. After ~ 6 month natural aging at room temperature, it was then artificially aged at 190°C for up to 120 hours.

2.2.1. Hardness Test

The aging response of the 8090 alloy was characterized by both the micro and macrohardness of the material. For macrohardness tests, the samples were finely ground on 600 grid SiC paper; the samples for microhardness tests were further polished with 0.01 μ m alumina powder. Macrohardness measurements were performed on a LECO RT-2400 Hardness Tester. The HRB hardness scale was chosen. Microhardness tests were carried out on a LECO M-400 Microhardness Tester with a 136° Vickers diamond indenter under a 10 gram load. The reason for using such a low load will be explained later when the experimental methodology for the composite material is described. Most of the macrohardness values were the arithmetic means of 10 readings at each aging condition. The microhardness results in this study are the arithmetic means of 30 readings at each aging condition.

2.2.2. Microstructural Examination

The microstructure of the alloy at different aging stages has been examined, aiming at a fundamental understanding of the strengthening mechanisms in the 8090 alloy and other Al-Li-Cu-Mg alloys. Because most of the microstructural changes during aging occur in the sub-micron scale, transmission electron microscopy (TEM) became the principal technique used in this thesis study.

TEM samples were made from thin sheets which had been thinned to below 50 μ m using a conventional mechanical thinning method. Discs of 3 mm diameter were then punched out of the sheets and subjected to electropolishing with a Fishioni twin-jet polisher. The electropolishing was conducted in a solution of 70%vol. methanol+30%vol. nitric acid at a temperature below -30°C, with a voltage of 15V and a current > 100mA.

TEM examination was performed on a Philips EM420 microscope with a working voltage of 120 kV. Centered dark field (CDF) imaging was the main method to characterize the different phases. Selected area diffraction patterns (SADP) were used to help identify the type of precipitates. In addition, convergent beam electron diffraction (CBED) was used to study some individual precipitates whose size and number density limited the applicability of SADP. Bright field (BF) imaging was also used as a supplementary method to examine the overall microstructure.

2.3. RESULTS

2.3.1. Aging Response Characterized By Hardness Change

2.3.1.1. Microhardness

The age hardening response of the 8090 alloy is presented in figure 2.1. The results indicate that:

- a) the material exhibited a initial hardness increase with aging time and achieved a peak hardness after about 8 hours;
- b) extended aging after 8 hours caused a decrease of the hardness which is similar to the overaging phenomenon observed in many aluminum alloys. After 16 hours of aging, the hardness started to climb up again, which resulted

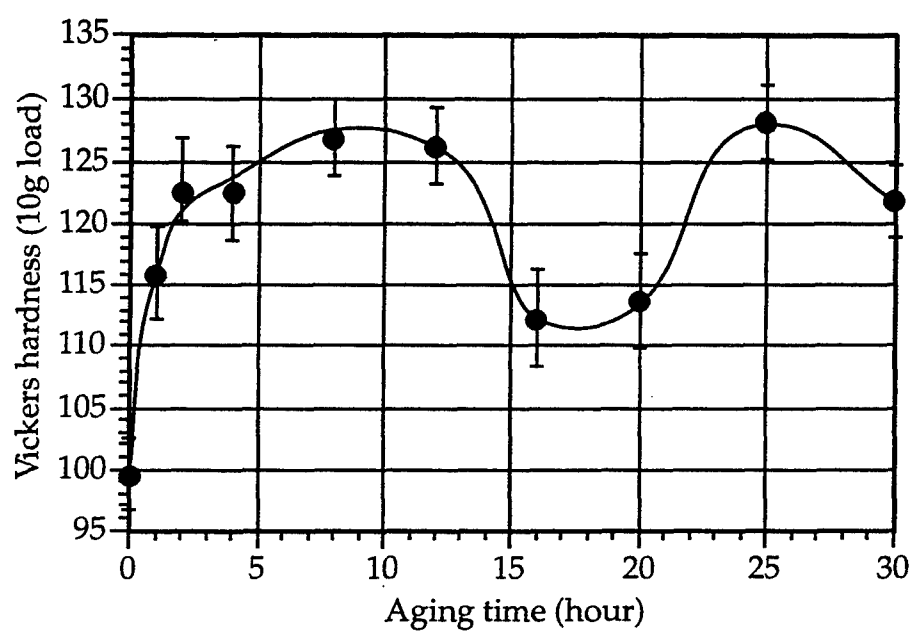


Figure 2.1 Microhardness of the 8090 alloy at different aging times when aged at 190°C. Testing load is 10 gram.

in the second aging peak at about 25 hours. A slight hardness decrease was caused again with 30 hours of aging.

Although two stage strengthening has never been reported in previous studies in the 8090 alloy, a similar age hardening feature had been observed in a study [25] on an Al-Li-Cu-Mg alloy with a slightly different composition from the 8090 alloy used in the present study. The two aging peaks were suggested in reference [25] to be the results of the δ' phase and the S' phase strengthening, respectively.

2.3.1.2. Macrohardness

Figure 2.2 is a plot of the macrohardness of the 8090 alloy vs. aging times. Most of the hardness increase occurred in the early stage (≤ 4 hours) of the aging process. Further increasing the aging time did not cause any other measurable hardness changes. There appears to be no significant peak aging and overaging. King et al [26] observed similar results when characterizing the aging response of the same alloy at 170°C using Vickers hardness.

2.3.2. Microstructural Development at 190°C

2.3.2.1. The δ' Phase

In common with other Al-Li alloys, the δ' phase is one of the predominant precipitates observed in the 8090 alloy. A homogeneous distribution and a high number density are the characteristics of δ' precipitates in this alloy, figure 2.3.

As the aging time increased, the δ' phase coarsened. Figures 2.4a-e are a series of micrographs of the δ' precipitates taken from samples aged for 8, 16, 20, 25 and 48 hours, respectively, and demonstrate the δ' coarsening process.

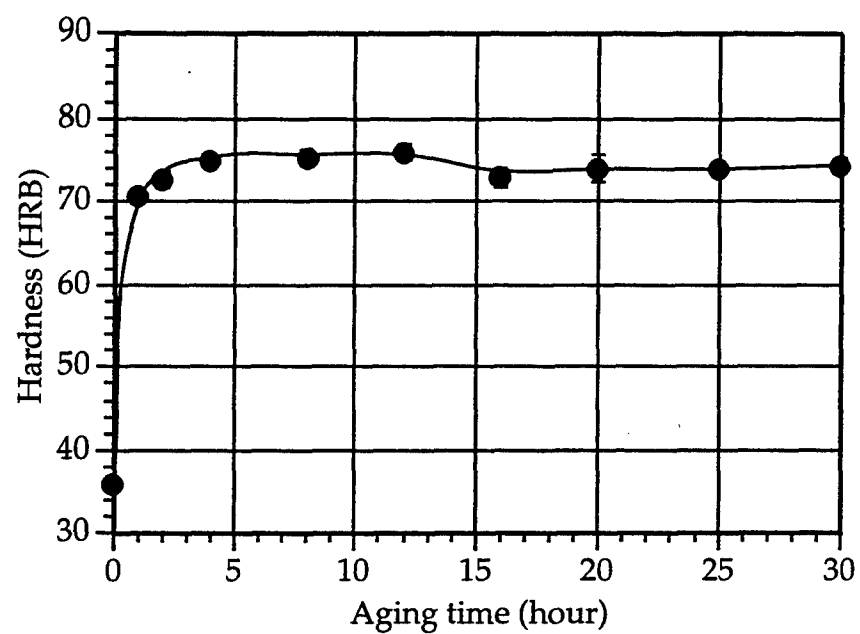


Figure 2.2 Macrohardness change upon aging at 190°C. No overaging phenomenon is observed up to 30 hours of aging.

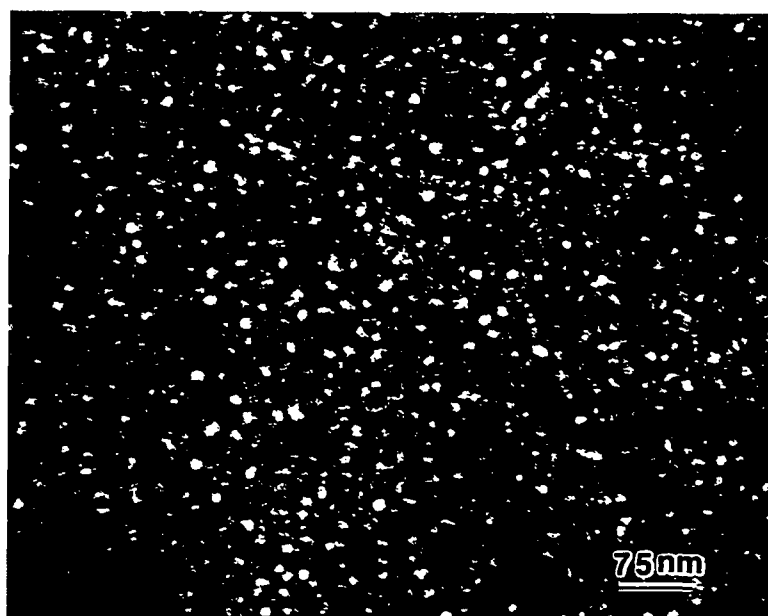


Figure 2.3 δ' precipitates in the 8090 alloy after 1 hour aging at 190°C (CDF image).

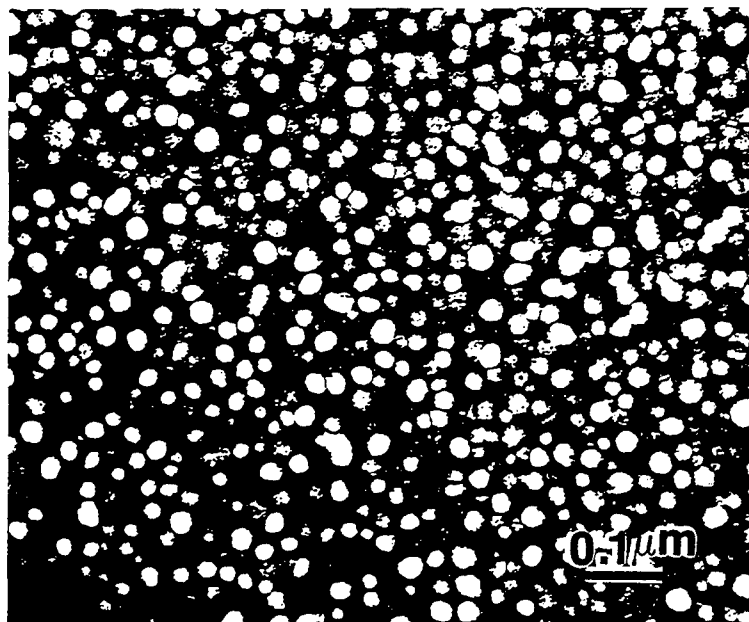


Figure 2.4a 8 hours

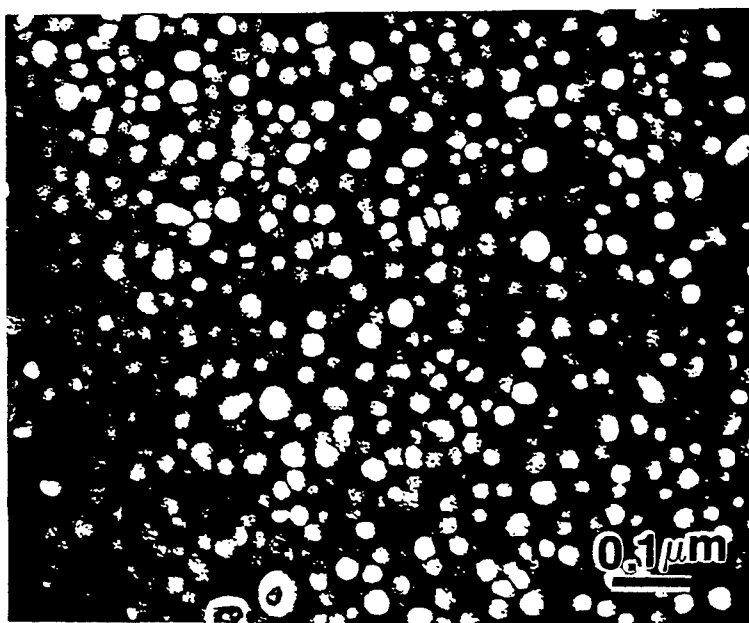


Figure 2.4b 16 hours

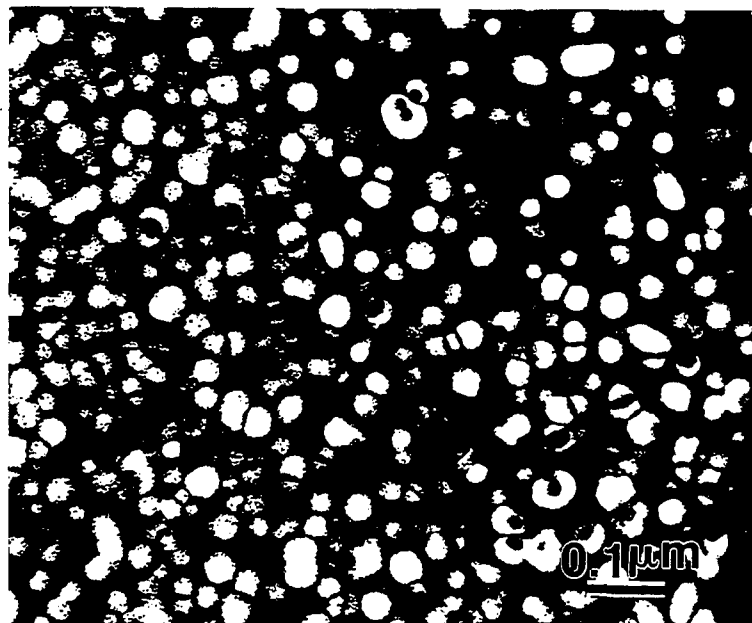


Figure 2.4c 20 hours

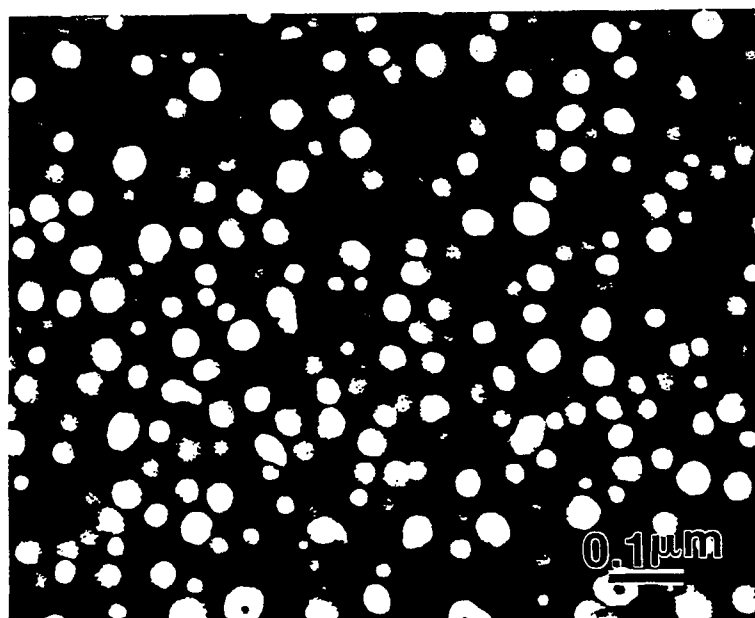


Figure 2.4d 25 hours

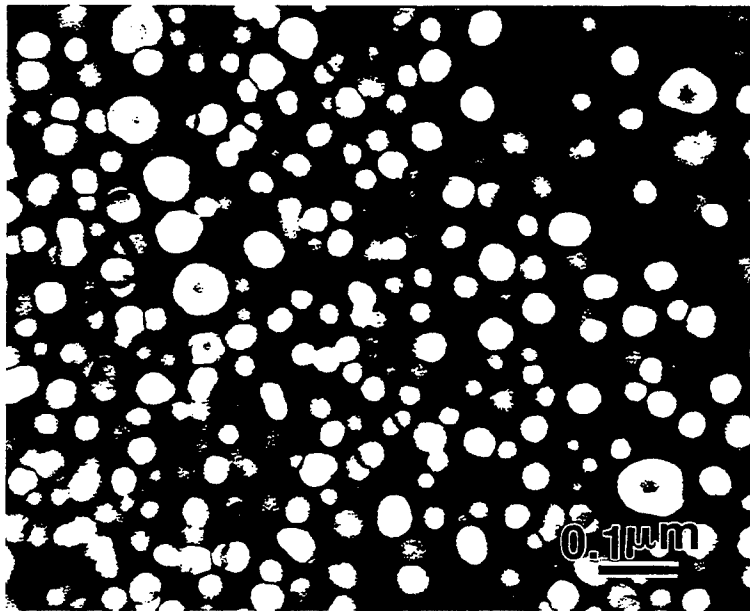


Figure 2.4e 48 hours

Figure 2.4 δ' phase coarsening with the increase of aging times.

In both figures 2.3 and 2.4, some "doughnut" shaped precipitates are observed. They are duplex δ'/β' precipitates which have been reported in previous studies [27-30]. β' (Al₃Zr) precipitates are formed during the solidification and the subsequent homogenization treatment. The β' phase also has a L1₂ structure and forms a cube-cube relationship with the α matrix. Because the δ' and β' phases are isostructural, an analysis based on classical nucleation theory has shown that the β'/α interface will act as a preferential nucleation site for the δ' phase [31]. After the δ' phase nucleates at the β'/α interface, it continues growing and finally forms an envelope around the β' core, hence the "doughnut" morphology. The duplex precipitation mode usually accelerates the coarsening of the δ' and causes a δ' PFZ around this duplex structure.

2.3.2.2. Quantitative Analysis of the δ' Phase

For the purpose of determining the strengthening potency of the δ' phase, the precipitation of the δ' phase has been quantitatively characterized as a function of aging time. The measurement results are presented below in table 2.1. The technical details of the measurement are given in Appendix I.

Table 2.1 δ' Diameter at Different Aging Time

time (hrs.)	1	2	4	8	12	16	20	25	30	48
\bar{d} (nm)	11.5	17.9	17.9	25.9	28.6	27.2	35.2	33.5	33.5	35.8

The average radii \bar{r} and aging time t are plotted as $\log \bar{r}$ vs. $\log t$ in figure 2.5. The slope of the line in figure 2.5 is 0.291 which, to a first approximation, yields:

$$\bar{r}^3 = k_1 t \quad (2.1)$$

with k_1 is a constant.

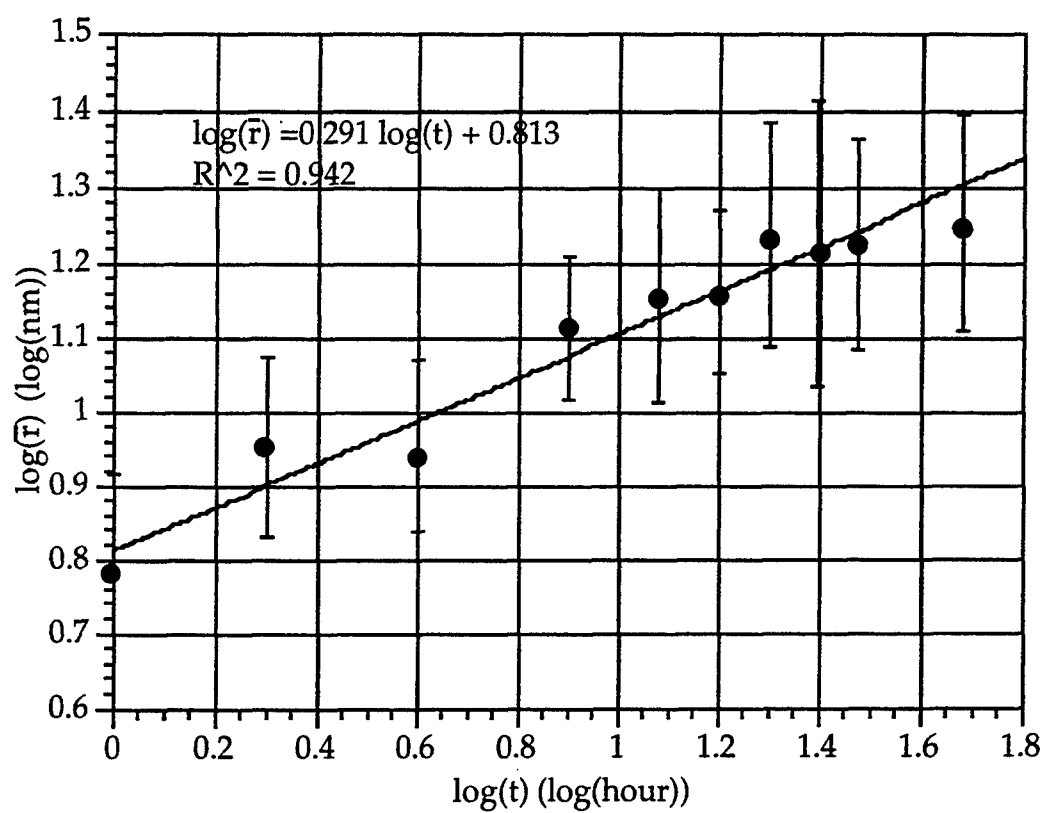


Figure 2.5 Average δ' precipitate size, \bar{r} , as a function of aging time, t .

Equation (2.1) should be viewed with caution since in general:

$$\bar{r}^n - \bar{r}_0^n = k't \quad (2.2)$$

and equation (2.1) can only be valid if \bar{r}_0 (the initial radius of the δ' precipitates) is equal to zero. Since the value of the exponent is close to 3 (which has been documented as the classical Lifshitz-Slyozov-Wagner (LSW) ($t^{1/3}$) rule [32, 33] by many previous studies[4, 17, 34-36]), the data were replotted as \bar{r} vs. $t^{1/3}$ (figure 2.6). The agreement is excellent. (Note: hereafter, R^2 in all the plots will be the squared correlation coefficient.)

Another parameter that has been quantitatively measured is the volume number density of the δ' precipitates, which is presented in figure 2.7 as a function of the aging times. The volume fraction of the δ' precipitates was then calculated and plotted in figure 2.8 as a function of aging time. The volume fraction of the δ' phase achieved a maximum at the aging time of 8 hours. It is interesting to notice that this is exactly the aging time where the first aging peak appears.

2.3.2.3. The S' Phase

In this study, the S' phase was observed as early as after 4 hours of aging. However, at this time, the precipitation of the S' phase is still at a very early stage. S' precipitates were only observed in a very few locations.

After 16 hours of aging, S' precipitates have become a striking microstructural component in the 8090 alloy, as shown in figure 2.9.

The S' phase exhibits a lath or rod morphology and has been reported as the predominant heterogeneously nucleated phase in Al-Cu-Mg alloys. Its orientation relationship (OR) with the α matrix has been reported by Bagaryatskii [37] and Silcock [38] as follows:

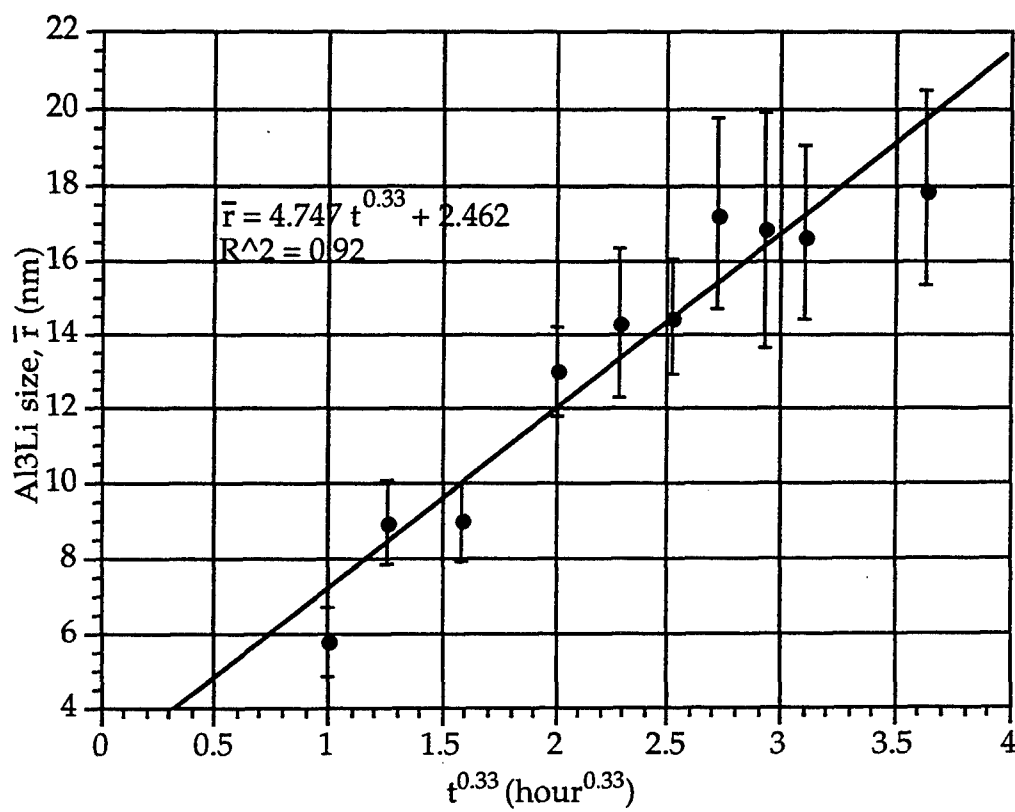


Figure 2.6 δ' coarsening kinetics.

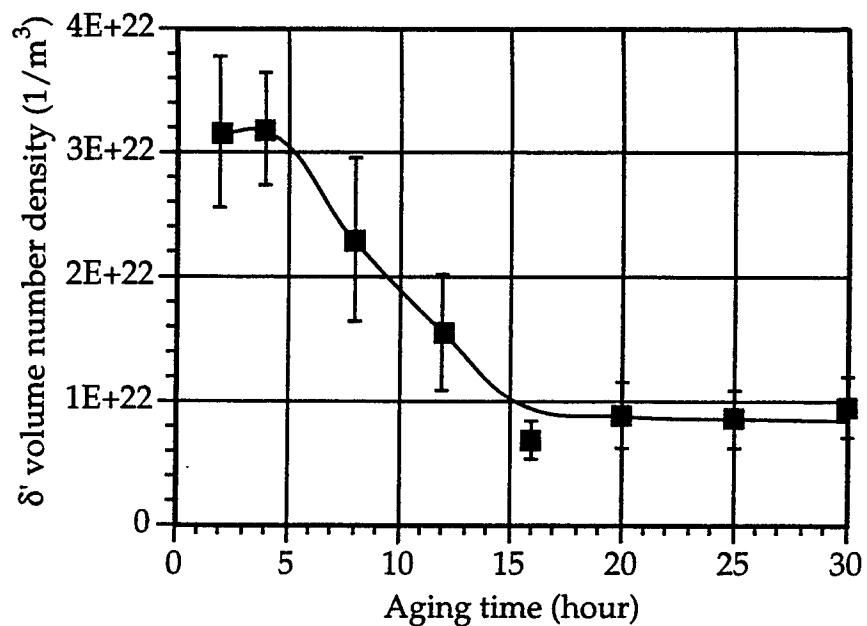


Figure 2.7 δ' volume number density as a function of aging time.

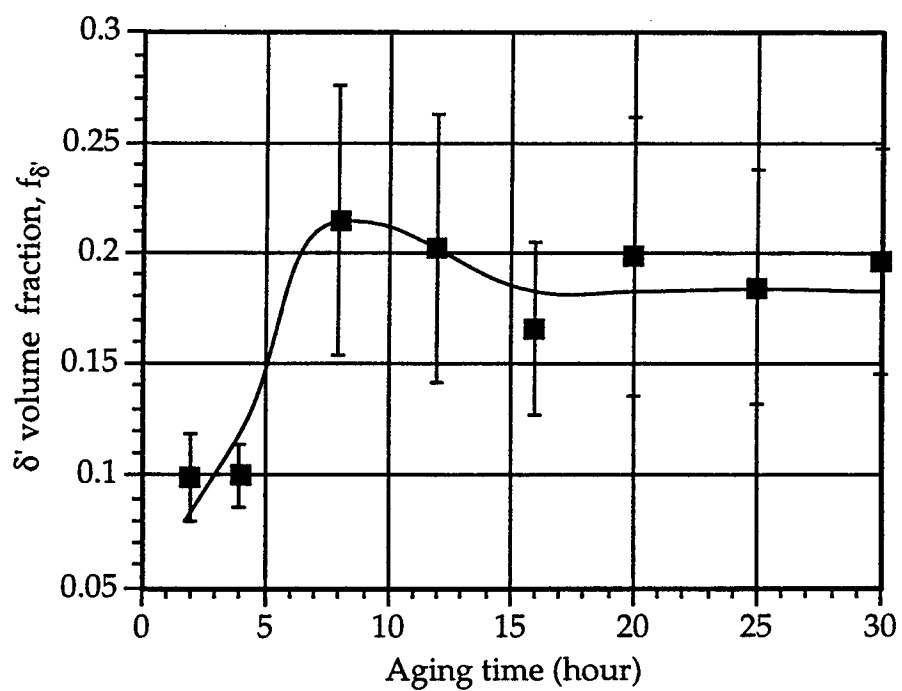


Figure 2.8 δ' phase volume fraction as a function of aging time.



Figure 2.9 S' precipitates after 16 hours of aging. There are three types of S': sheets (A), laths (B) and finely dispersed rods (C).

$$\{100\}_{S'} \parallel \{100\}_{\alpha}$$

$$\langle 010 \rangle_{S'} \parallel \langle 021 \rangle_{\alpha}$$

$$\langle 001 \rangle_{S'} \parallel \langle \bar{0}12 \rangle_{\alpha}$$

Based on this OR, there will be 12 S' variants precipitated in Al-Cu-Mg alloys. These 12 variants can be further divided into 3 groups according to their a axis, i.e., $[100]_{S'}$, orientation. The 3 groups and 12 variants of S' precipitates are listed in table 2.2. The geometric shape of a S' lath and the spatial orientation of 3 groups of S' precipitates are schematically illustrated in figures 2.10a and b.

The longitudinal direction of S' laths has been shown to be $[100]_{S'}$, or the a axis, which is parallel to $[100]_{\alpha}$ [39]. The habit planes of the S' phase have been shown to be $\{210\}_{\alpha}$, which are parallel to $(010)_{S'}$ and $(001)_{S'}$, by Yan [40] and Radmilovic et al [41]. As shown in figure 2.10b, all the S' laths from the same group lay with their a axes parallel to each other. The S' precipitates from different groups have their a axes perpendicular to each other, as shown in figure 2.9. Consequently, although there are 12 possible variants of S' precipitates in the α matrix, they may often be seen as only three differently oriented laths (according to their a axes). The different variants from the same group are very difficult to distinguish unless they are viewed upright, such as the 4 variants of S' in group III schematically shown in figure 2.10b.

Dislocations are the most potent nucleation sites for S'. The S' precipitates are often formed adjacent to each other and develop a "sheet" morphology as shown in figure 2.11a. To distinguish the S' nucleated at dislocations from the precipitates nucleated at other locations, the S' precipitates nucleated at dislocations will be designated as type A hereafter. The S' precipitates formed at dislocation loops and helices are shown in figures 12a and b.

Table 2.2 Orientation of the 12 Variants of the S' Phase

Group (according the a axis orientation)	Variant (b and c axes orientation)
Group I $[100]_{S'} \parallel [100]_{\alpha}$	$[010]_{S'} \parallel [021]_{\alpha} [001]_{S'} \parallel [\bar{0}\bar{1}2]_{\alpha}$
	$[010]_{S'} \parallel [012]_{\alpha} [001]_{S'} \parallel [0\bar{2}1]_{\alpha}$
	$[010]_{S'} \parallel [0\bar{2}1]_{\alpha} [001]_{S'} \parallel [012]_{\alpha}$
	$[010]_{S'} \parallel [0\bar{1}2]_{\alpha} [001]_{S'} \parallel [021]_{\alpha}$
Group II $[100]_{S'} \parallel [010]_{\alpha}$	$[010]_{S'} \parallel [102]_{\alpha} [001]_{S'} \parallel [201]_{\alpha}$
	$[010]_{S'} \parallel [201]_{\alpha} [001]_{S'} \parallel [10\bar{2}]_{\alpha}$
	$[010]_{S'} \parallel [10\bar{2}]_{\alpha} [001]_{S'} \parallel [201]_{\alpha}$
	$[010]_{S'} \parallel [20\bar{1}]_{\alpha} [001]_{S'} \parallel [102]_{\alpha}$
Group III $[100]_{S'} \parallel [001]_{\alpha}$	$[010]_{S'} \parallel [210]_{\alpha} [001]_{S'} \parallel [120]_{\alpha}$
	$[010]_{S'} \parallel [120]_{\alpha} [001]_{S'} \parallel [\bar{2}10]_{\alpha}$
	$[010]_{S'} \parallel [\bar{2}10]_{\alpha} [001]_{S'} \parallel [120]_{\alpha}$
	$[010]_{S'} \parallel [\bar{1}20]_{\alpha} [001]_{S'} \parallel [210]_{\alpha}$

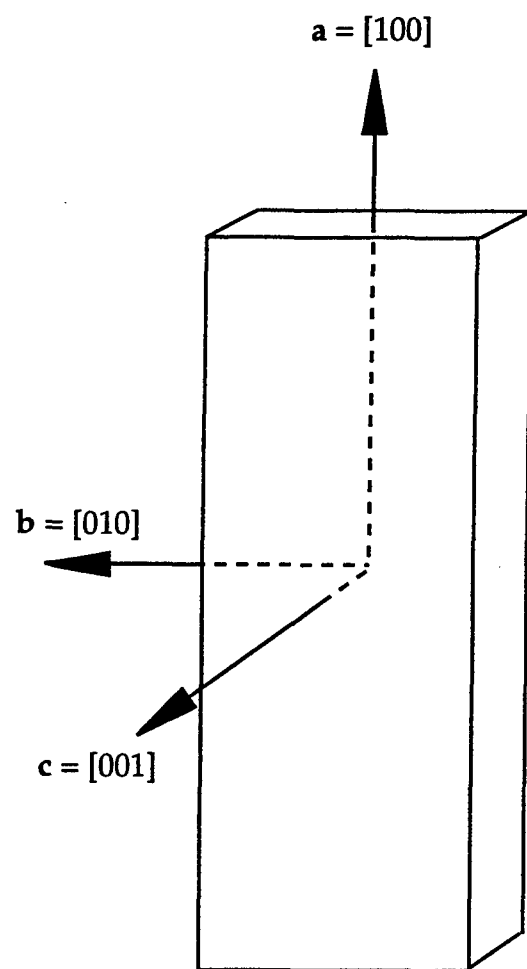


Figure 2.10a Morphology of a S' lath.

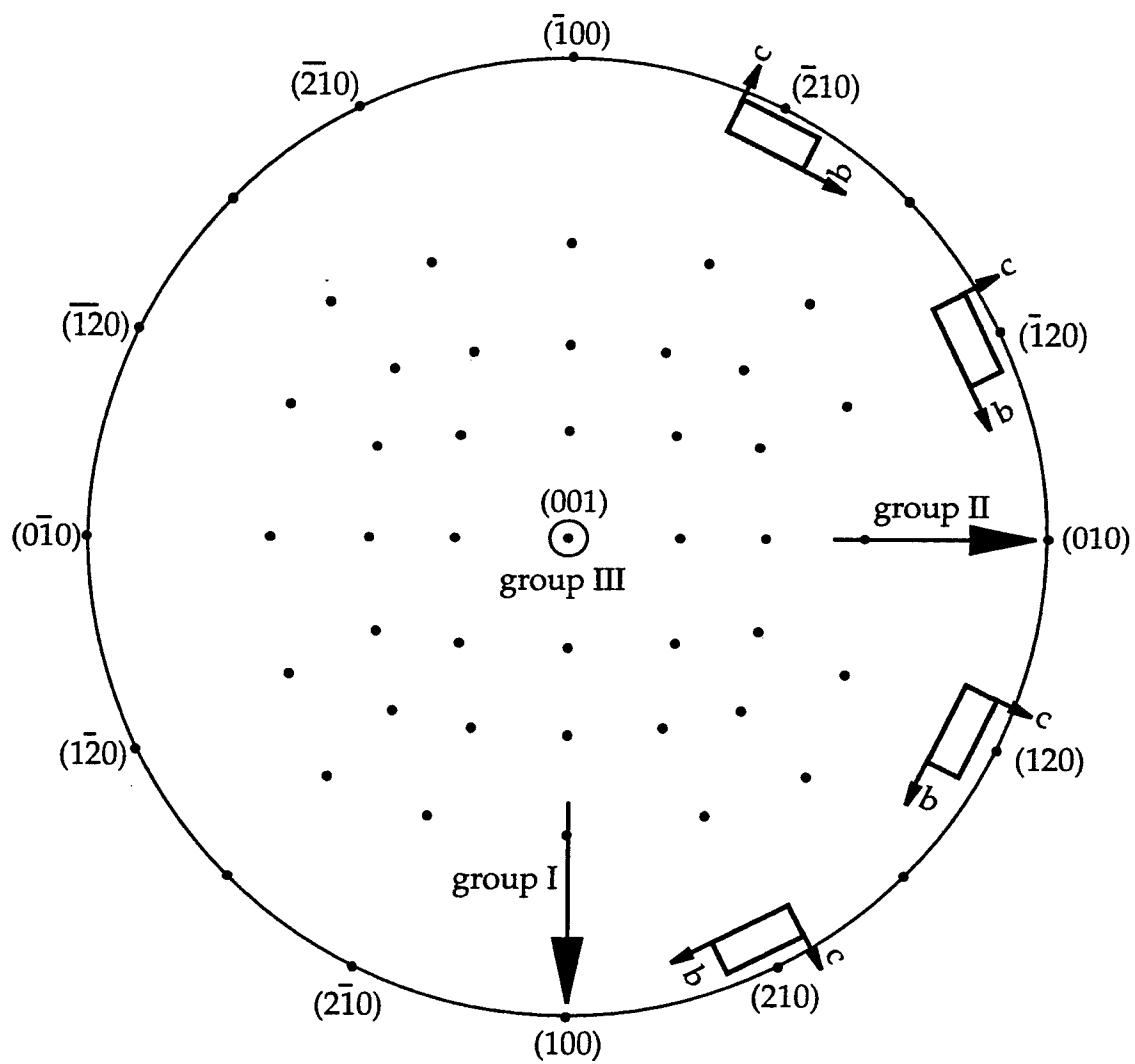
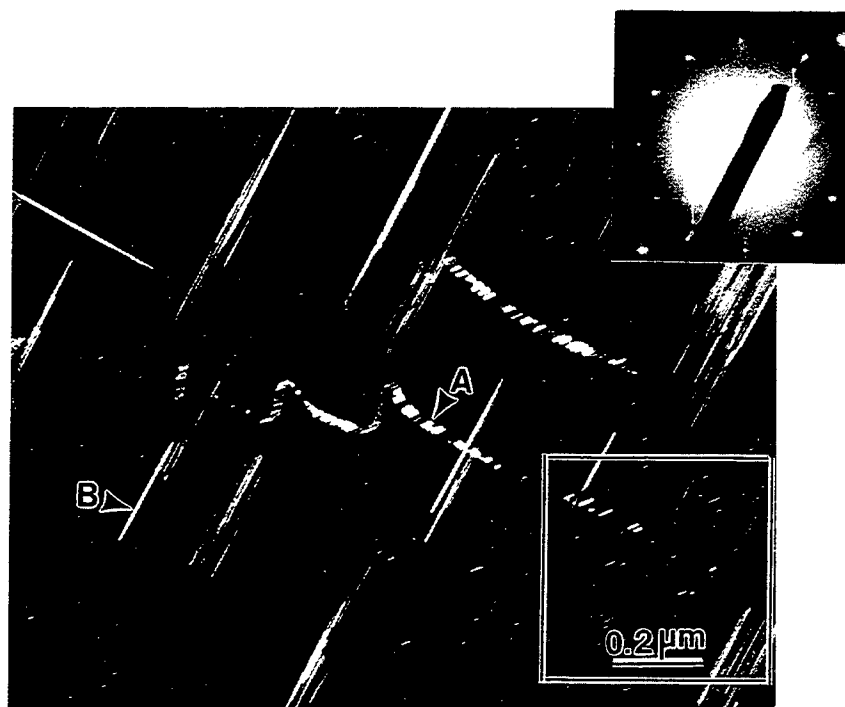
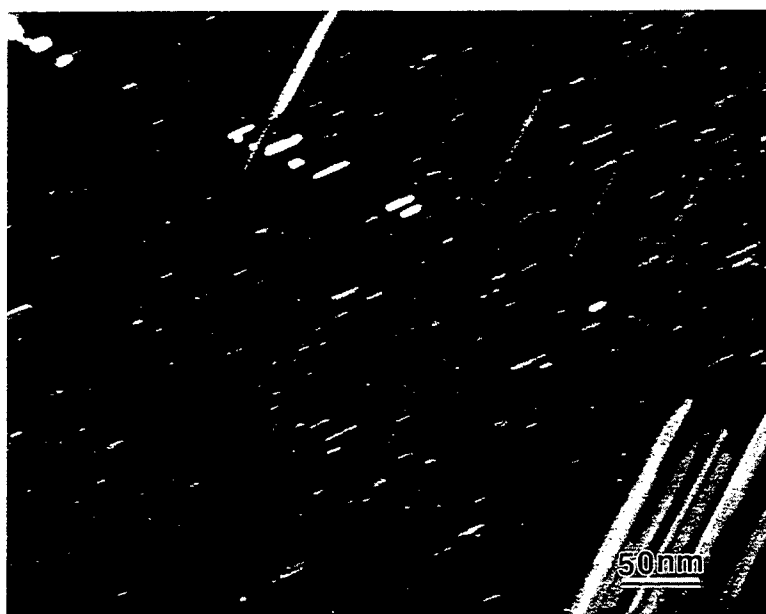


Figure 2.10b Spatial orientation of the 3 S' groups and the 4 variants (rectangles) in group III.



(a) S' precipitates nucleated at dislocations (type A) and independently (type B)

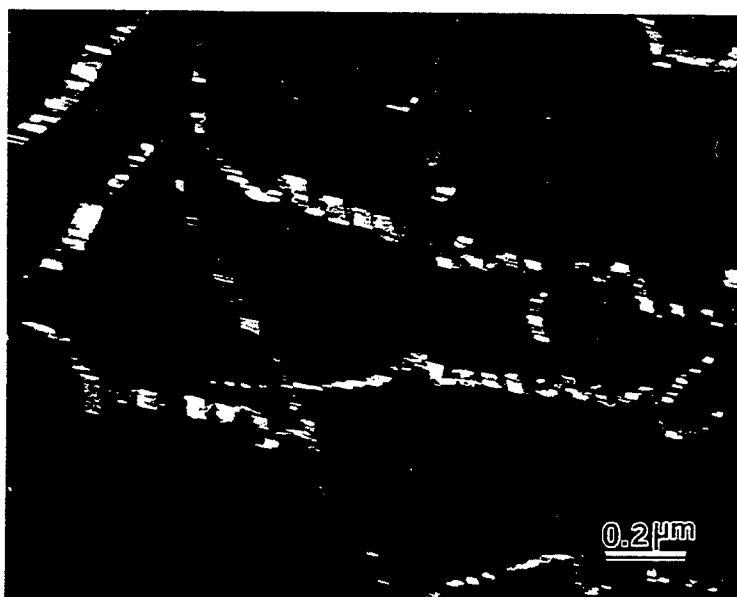


(b) enlargement of the framed area in (a) showing S' type C

Figure 2.11 Three types of S' precipitates, A, B, and C, in an 8090 sample.



(a)



(b)

Figure 2.12 S' precipitates nucleated at (a) dislocation loops, and (b) dislocation helices.

In the present study, in addition to those S' sheets nucleated at dislocations, S' laths which are apparently independent of dislocations have also been observed and termed type B, such as the precipitates marked as B in both figures 2.9 and 2.11a. These S' laths have a similar size and intensity, in the CDF images of figures 2.9 and 2.11a, as compared to the S' sheets in the same micrograph and possibly formed at vacancies and vacancy clusters within the matrix.

A detailed examination of figure 2.11a reveals that there are numerous finely distributed precipitates in the background in addition to the S' sheets (A) and laths (B). Figure 2.11b is a enlarged image of these fine precipitates. Because these fine precipitates are illuminated together with the S' precipitates A and B in a CDF image and appear to have the same orientation as the S' precipitate sheets (A), they are also identified as S' precipitates. As compared to the S' sheets (A) and laths (B), these scattered S' precipitates are much finer, which suggests that they formed at a later aging stage than both S' precipitate type A and type B and hence are named as type C. The nucleation mechanism of three types of S' precipitates will be discussed in Chapter 3.

The growth of the S' phase as a function of the aging times has been studied in this thesis study. Because the sizes of S' precipitates in *b* and *c* axes are both relatively small and very difficult to be measured accurately, the growth of the S' precipitates is characterized by the length change along *a* axis. For the similar reason, only the type A and type B of S' precipitates were measured. The average length *L* and aging times *t* are plotted as log *L* vs. log *t* in figure 2.13a. The slope of the line in figure 2.13a is 0.62 which yields:

$$L = k_2 t^{0.62} \quad (2.3)$$

with k_2 as a constant.

Since the value of the exponent is close to 0.5, the length change has been plotted vs. $t^{0.5}$ in figure 2.13b. The length increase of the S' precipitates follows the square root relationship with the aging times, which is usually observed in diffusion controlled processes.

2.3.2.4. Other Phases

I) The T_1 Phase

In the 8090 alloy, the precipitation of T_1 is suppressed by the existence of the S' phase, which is the major Cu bearing phase in this alloy. However, after a long time aging, T_1 was still observed. Figure 2.14 is a micrograph taken from a sample aged for 120 hours. In this micrograph, there are four types of differently oriented precipitates, which could be either lath/rod-like or plate-like with the electron beam lying within the plate. Precipitates A and B are oriented with a mutual angle of 100° in this micrograph. Both of them are at an angle of 130° to precipitates C. The images of all the precipitates in figure 2.14 are their projections on the image plane. The mutual angles are the angles between the precipitate projections instead of the angles between the real precipitates. To illustrate the relationship between the precipitate projection and the precipitates themselves, a stereographic projection (figure 2.15) is used. Because the beam direction in figure 2.14 is $[112]_\alpha$, a stereographic projection with $[112]_\alpha$ as the center was chosen for figure 2.15. From 2.15, the mutual angle between the projection of any directions on to the plane normal to the $[112]_\alpha$ can be determined. It was found that the mutual angles between precipitates A, B and C match the angles of the projections of the three $\langle 100 \rangle_\alpha$ directions. Hence, it can be concluded that precipitates A, B and C are the S' precipitates from the three groups described

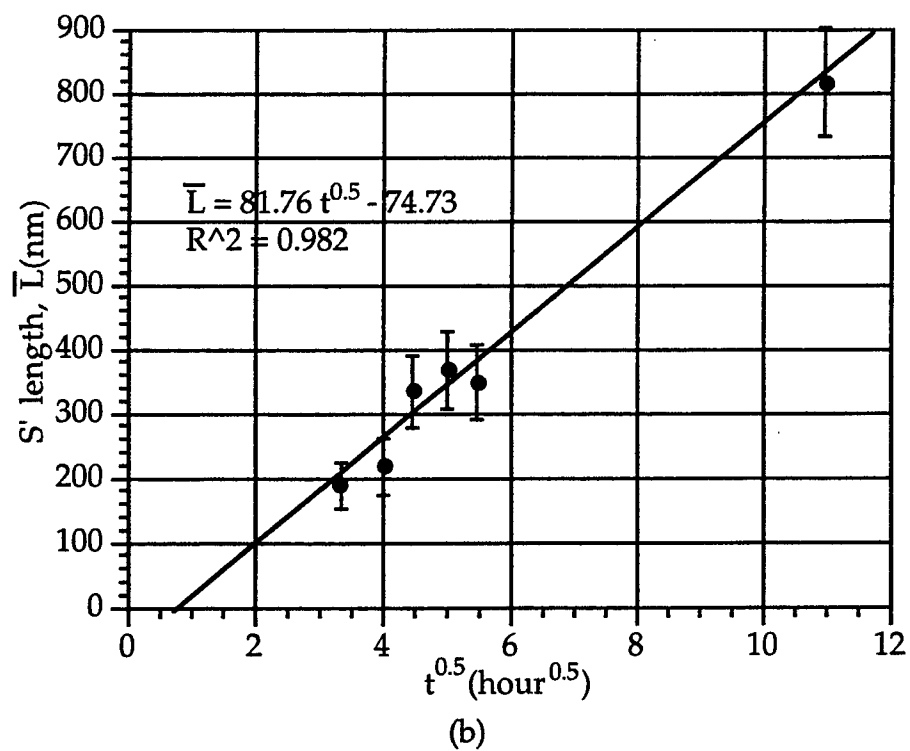
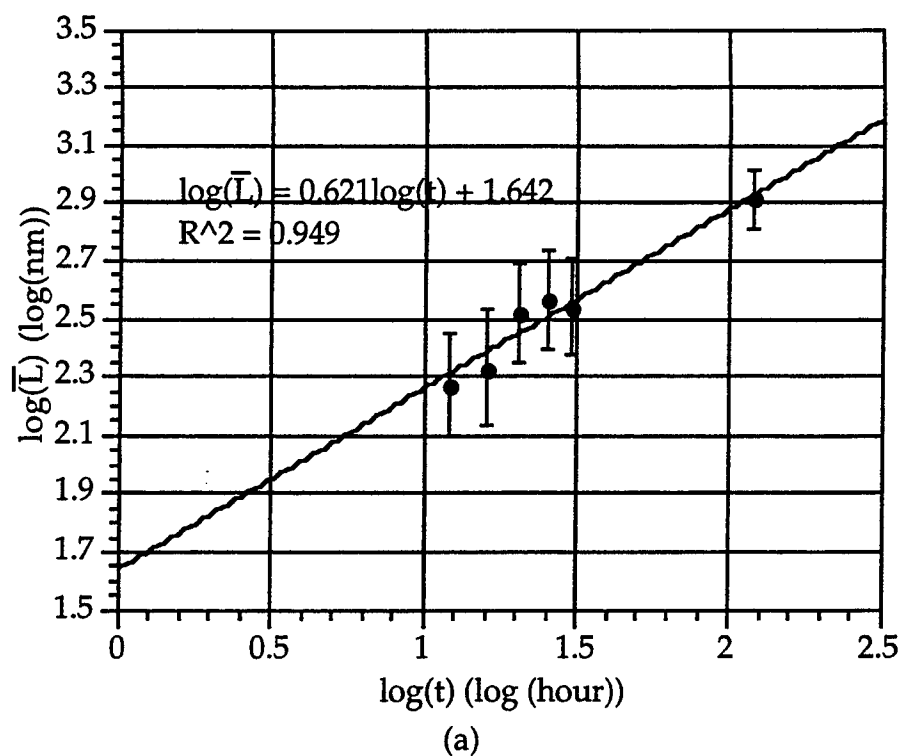


Figure 2.13 S' growth kinetics at 190°C

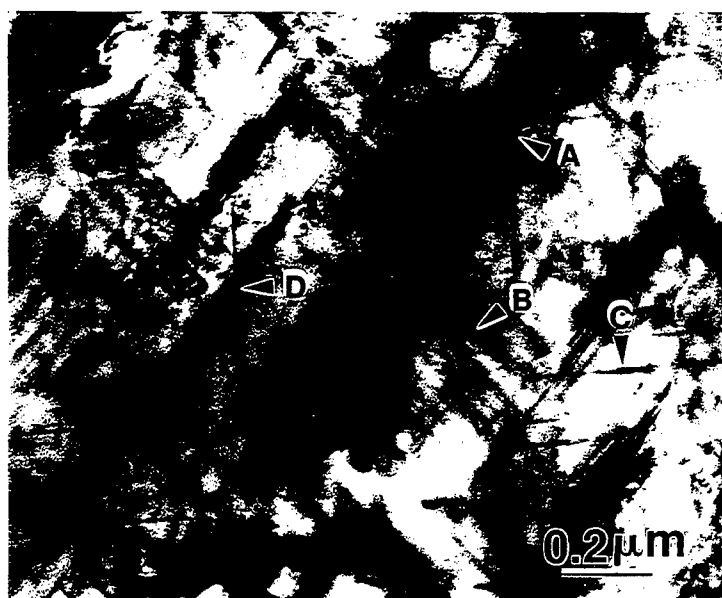


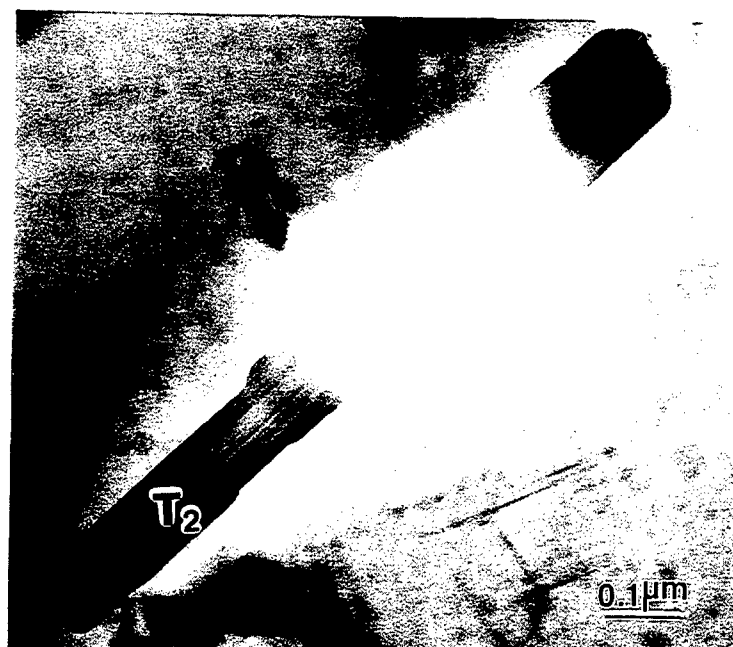
Figure 2.14 S' (A, B, C) and T1 (D) in an 8090 sample aged for 120 hours at 190°C.

in table 2.2. Because S' precipitates can only be divided into three groups, precipitates D have to be some other type of precipitates. The geometric shape and the composition of the 8090 alloy suggest that they are possibly the T_1 phase. Since the T_1 phase forms on $\{111\}_\alpha$ planes as plates, the morphology like precipitates D can only be seen if the T_1 phase has its plate normal perpendicular to the beam direction $[112]_\alpha$. Again, by examining the angles between precipitates D and the other three types in figure 2.14, and comparing these angles with the possible $\{111\}_\alpha$ plane projections and $\langle 100 \rangle_\alpha$ projections in figure 2.15, precipitates D were determined as T_1 precipitates formed on $(11\bar{1})_\alpha$ plane. It is interesting to notice that the number density of the T_1 phase is much lower than the S' phase, which means that the S' phase is still the predominant Cu bearing phase after 120 hour aging in the 8090 alloy.

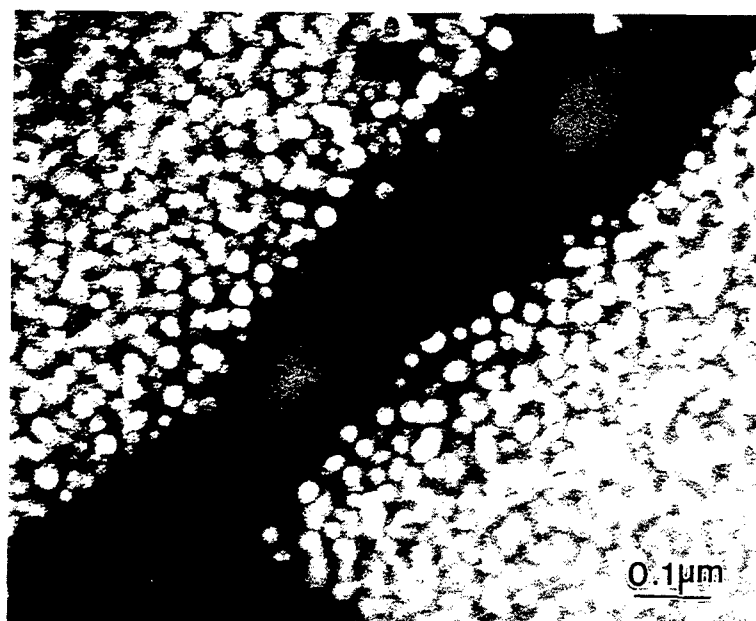
II) The T_2 phase

In this study, the T_2 phase was conclusively identified at a grain boundary after 8 hours of aging. Figures 2.16a and b are a BF and the δ' CDF images, respectively, at this location. A δ' PFZ can be seen at this grain boundary. Figure 2.17 is a convergent beam electron diffraction (CBED) pattern from the T_2 precipitate at the grain boundary in figure 2.16a. The ten-fold symmetry, which has been documented as a characteristic of the T_2 phase, is clearly seen in figure 2.17.

Figures 2.18a and b are a pair of micrographs showing a coarse precipitate within a grain after 20 hours of aging. This precipitate is microcrystalline which has been proved to belong to the decomposed T_2 phase [43,44]. In figure 2.18b, a δ' PFZ can be seen clearly in the vicinity of the decomposed T_2 . Since the formation of T_2 is a primary cause for the existence of the δ' PFZs, this, again, suggests that the precipitate in figure 2.18a is the T_2 phase.



(a)



(b)

Figure 2.16 T_2 phase and the associated δ' PFZs formed at a grain boundary after 8 hours of aging. (a) BF image and (b) δ' CDF image.

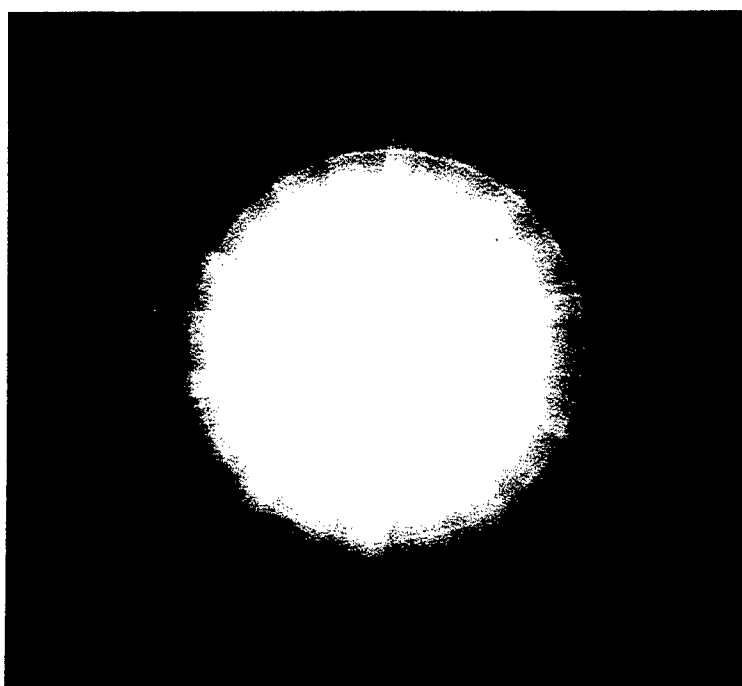
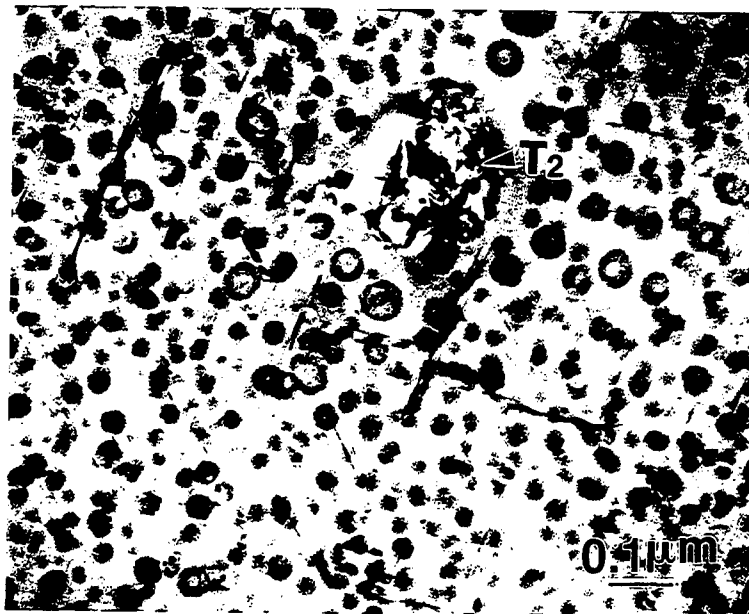
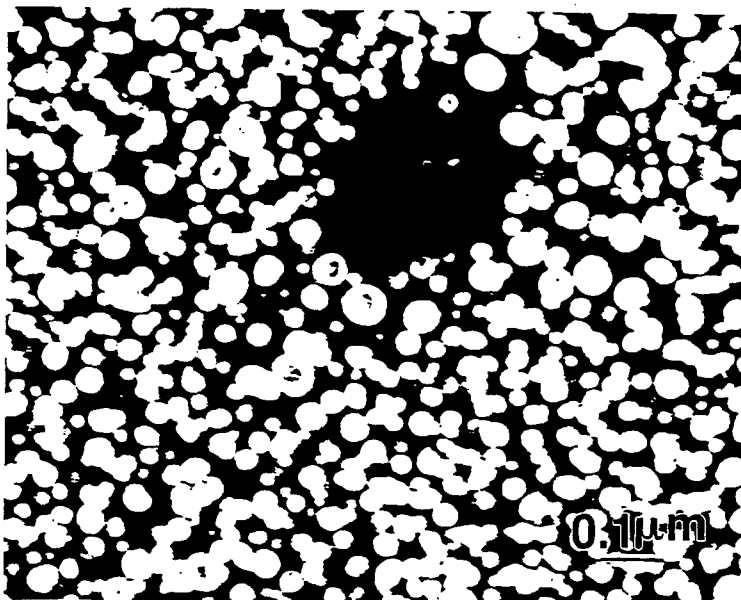


Figure 2.17 Low camera convergent beam electron diffraction (CBED) pattern from the T2 phase in figure 2.16.



(a)



(b)

Figure 2.18 (a) Decomposed T2 phase within matrix and
(b) associated δ' PFZ.

III) The δ Phase

The existence of the δ phase has been confirmed in this thesis study after extended aging. Figures 2.19a and b are a CDF image of a precipitate observed within the matrix in the 8090 alloy after 48 hour aging and the corresponding CBED pattern. The indexing of the CBED pattern indicates that the precipitate in figure 19a is the δ phase. Figure 20a is a CDF image formed from the indicated reflection in figure 20b. Using the matrix reflection as a reference, the reflection was indexed as the $[220]$ from the δ phase. From the CDF, it can be seen that around the δ phase, there is a δ' PFZ.

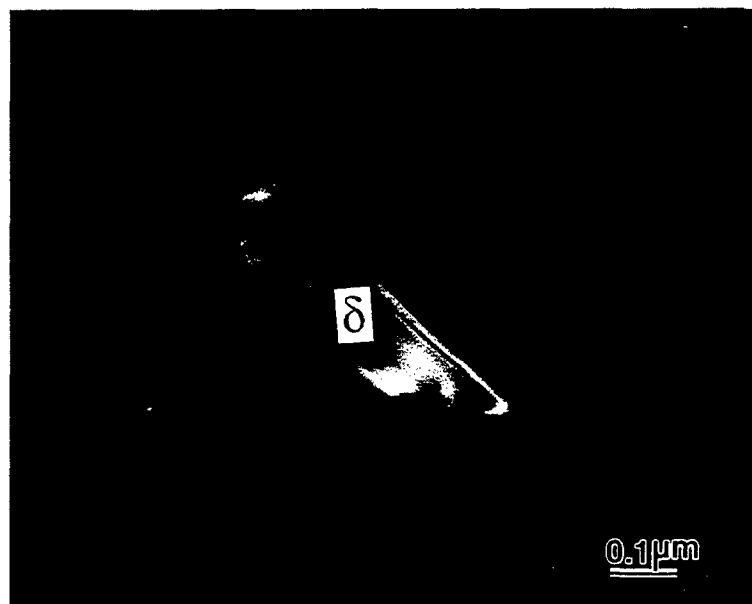
2.3.2.5 Grain Boundary Structural Development

I) δ' PFZs

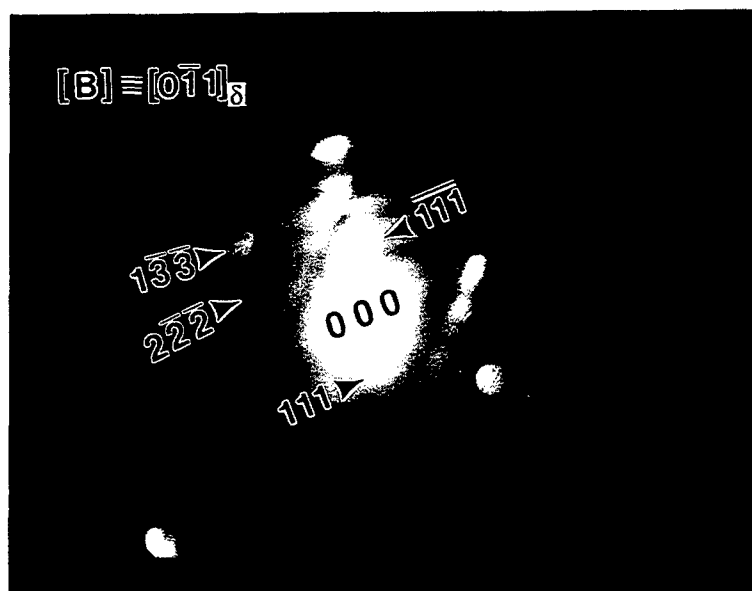
The T_2 phase was observed at grain boundaries in this study after 8 hours of aging. In fact, precipitates at grain boundaries and the associated δ' PFZs were observed as early as after 1 hour of aging, figure 2.21. However, at this aging stage, grain boundary precipitates and δ' PFZs are not well-developed yet. In many occasions, grain boundaries are still very clean and δ' precipitates extend up to the boundaries.

Both the grain boundary precipitation and δ' PFZs develop with the aging time. Figure 2.22 shows a grain boundary region in a sample after 20 hours of aging. The increase of the number density of grain boundary precipitates and the width of δ' PFZs is significant.

In the present study, the development of the δ' PFZs has been characterized quantitatively by its width change at different aging times. The results have been plotted in figure 2.23. The δ' PFZ width also follows a $t^{0.5}$ relationship with aging time, which has been reported earlier by Jha et al [45].

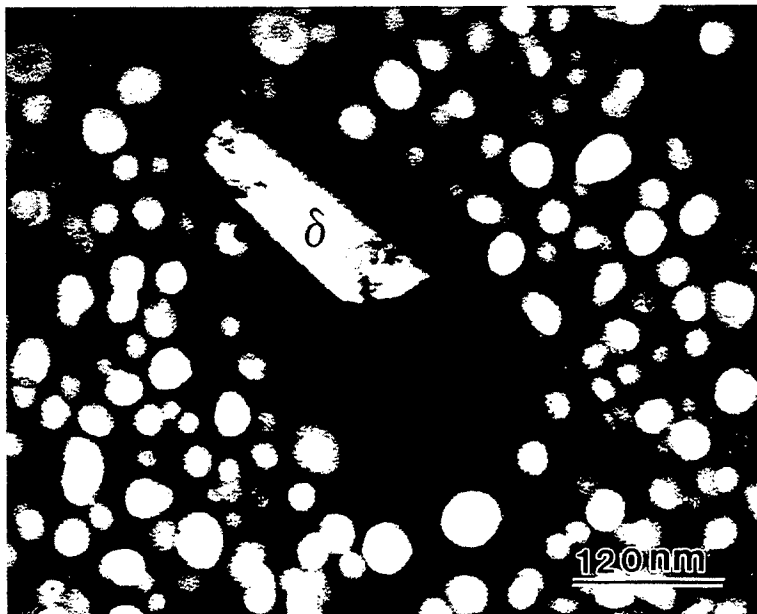


(a)



(b)

Figure 2.19 (a) δ precipitate, and (b) the CBED pattern from this phase.



(a)



(b)

Figure 2.20 δ precipitate and SAD pattern within the α matrix.

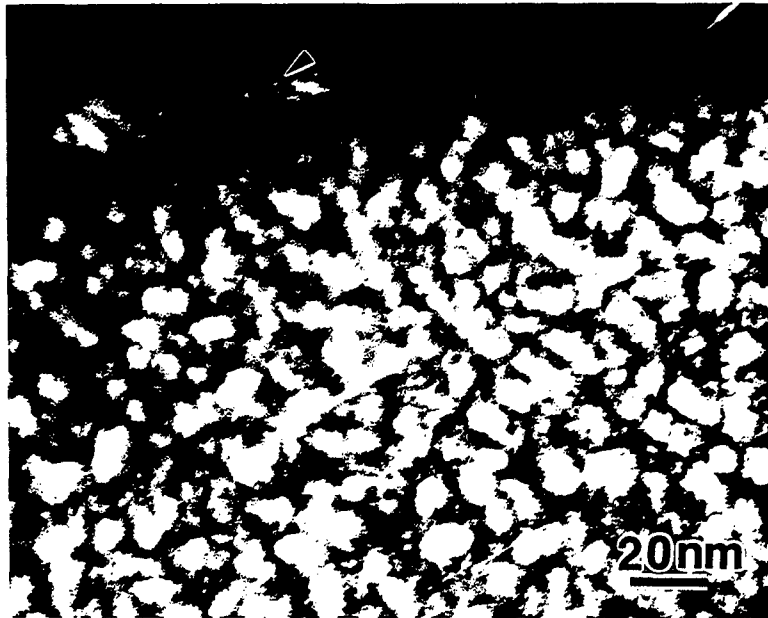
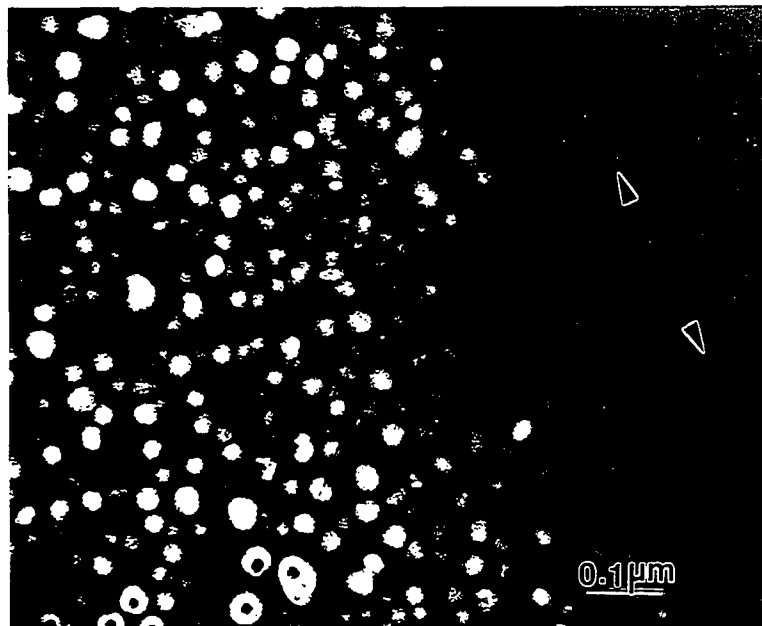
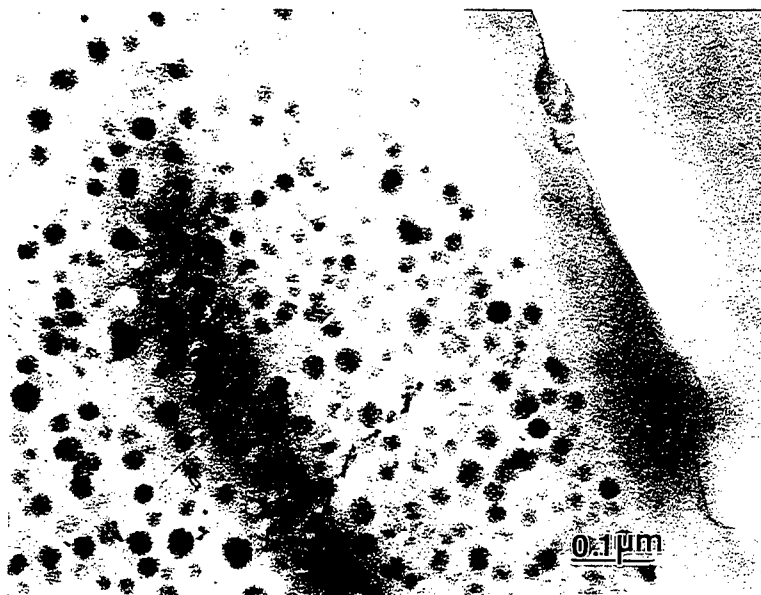


Figure 2.21 Grain boundary precipitate (arrowed) and δ' PFZ next to the grain boundary after 1 hour of aging.



(a) CDF (grain boundary is arrowed)



(b) BF

Figure 2.22 Grain boundary precipitates (probably T2) and the associated δ' PFZ in a sample aged for 20 hours. It is noticed that the δ' PFZ width has increased significantly.

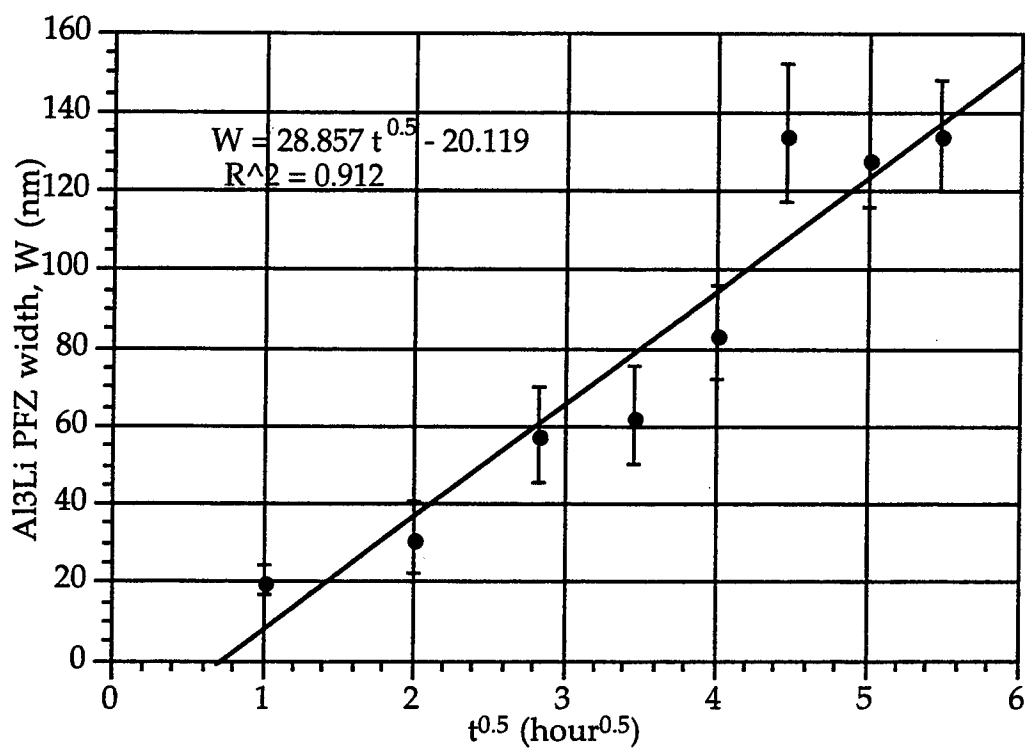
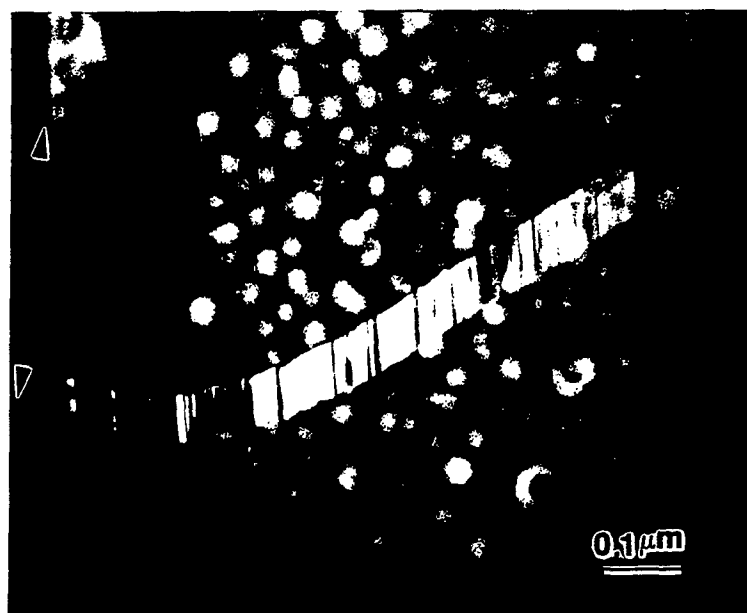


Figure 2.23 δ' PFZ development as a function of aging time t .

II) S' Precipitate Distribution along Grain Boundaries

Figures 2.24a and b show a grain boundary and its vicinity after 48 hours of aging. A δ' PFZ can be seen along the boundary in figure 2.24a. Since in this micrograph, both the δ' and the S' phases are illuminated at the same time, it can also be seen that the heterogeneously nucleated S' precipitates extend through the δ' PFZ almost to the boundary. In figures 2.24a, some finely dispersed S' precipitates can also be seen in the matrix. It is noticed that these fine S' precipitates are not seen in the vicinity of the boundary. Figure 2.24b is a lower magnification image of the same area and again shows that the heterogeneously nucleated S' does not contact the grain boundary. Figure 2.25 shows this more clearly. In this micrograph, in the interior of the grain, numerous dislocation loops decorated with S' precipitates can be seen together with a high density of fine precipitates of type B or C. However, in the vicinities of the grain boundaries in figure 2.25, there is a zone which is free of both types of precipitates. As will be discussed in Chapter 3, this is very likely due to vacancy annihilation at the boundary, which suppressed both the formation of dislocation loops and the precipitation of types B and C. The formation of dislocation loops and the nucleation mechanism of precipitates type B and type C will be discussed in Chapter 3.

To observe the effect of longer aging time on the precipitation of the S' phase near grain boundaries, a sample aged for 120 hours has also been examined. Figures 2.26a, b and c are the δ' CDF, S' CDF and the BF image at the same grain boundary region, respectively. In these micrographs, with the longer time aging, the δ' PFZs are not only limited in the boundaries, but also formed within grains as seen in figure 2.26a. As to the S' phase, although it did not develop a precipitate free zone as significant as the δ' phase, in



(a) CDF of both the δ' and S' phases (grain boundary is arrowed)



(b) BF image of lower magnification from the same area

Figure 2.24 S' precipitation and δ' PFZ in the vicinity of a grain boundary.

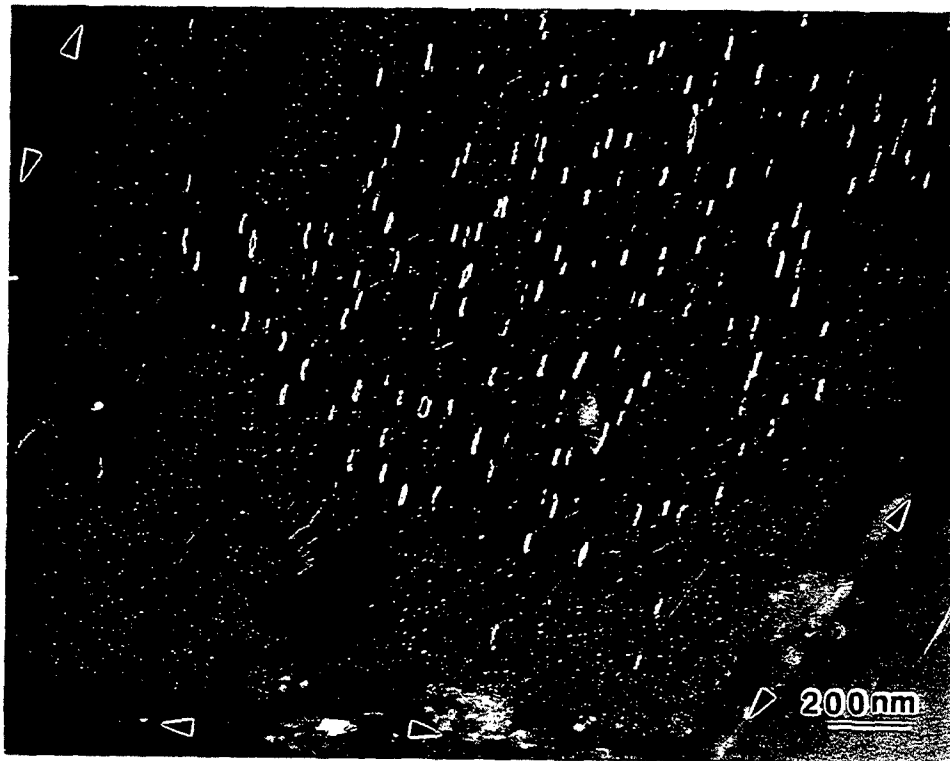
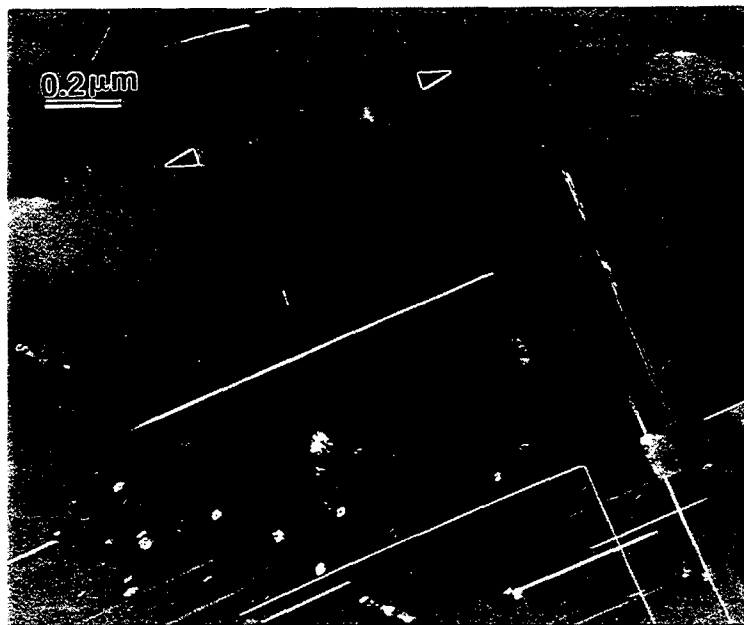


Figure 2.25 Dislocation loop (S' type A) free zone and S' type C free zone along grain boundaries (arrowed).



(a) CDF of the δ' phase (grain boundary is arrowed)



(b) CDF of the S' phase (grain boundary is arrowed)



(c) BF image of the same region shown in (a) and (b)

Figure 2.26 δ' PFZs and the distribution of S' phase in a sample aged for 120 hours.

common with the situation observed in figure 2.24, S' laths were not able to contact the grain boundary. In fact, there exists a very narrow S' free zone.

2.4. DISCUSSION

2.4.1. Aging Response

In § 2.2.2, the aging response of the 8090 alloy was presented in two forms: microhardness and macrohardness. A slight overaging was observed from the microhardness curve. On the other hand, the macrohardness results indicate that the strengthening effect is very stable. Up to 30 hours of aging, the alloy does not exhibit any visible overaging effect. These two sets of results look inconsistent at first glance. However, because the two sets of curves are presented on different scales, a direct comparison requires a single scale. For this purpose, the microhardness results presented in figure 1 were converted into HRB scale according to the chart in reference [46]. The converted results are presented in figure 2.27 together with the original microhardness data. From this curve, it can be seen that the overaging feature shown on the microhardness scale disappeared in the converted macrohardness data. It is believed that because the HRB scale is not as sensitive to minor property changes as is the microhardness scale, the slight overaging in the 8090 alloy between 8 and 25 hours is undetectable in HRB scale.

2.4.2. Principal Strengthening Precipitates in 8090 Alloy

The microhardness test indicates that the material experienced two strengthening stages in the 30 hour aging period, one achieved the peak effect after 8 hours of aging, the second exhibited maximum strengthening with 25

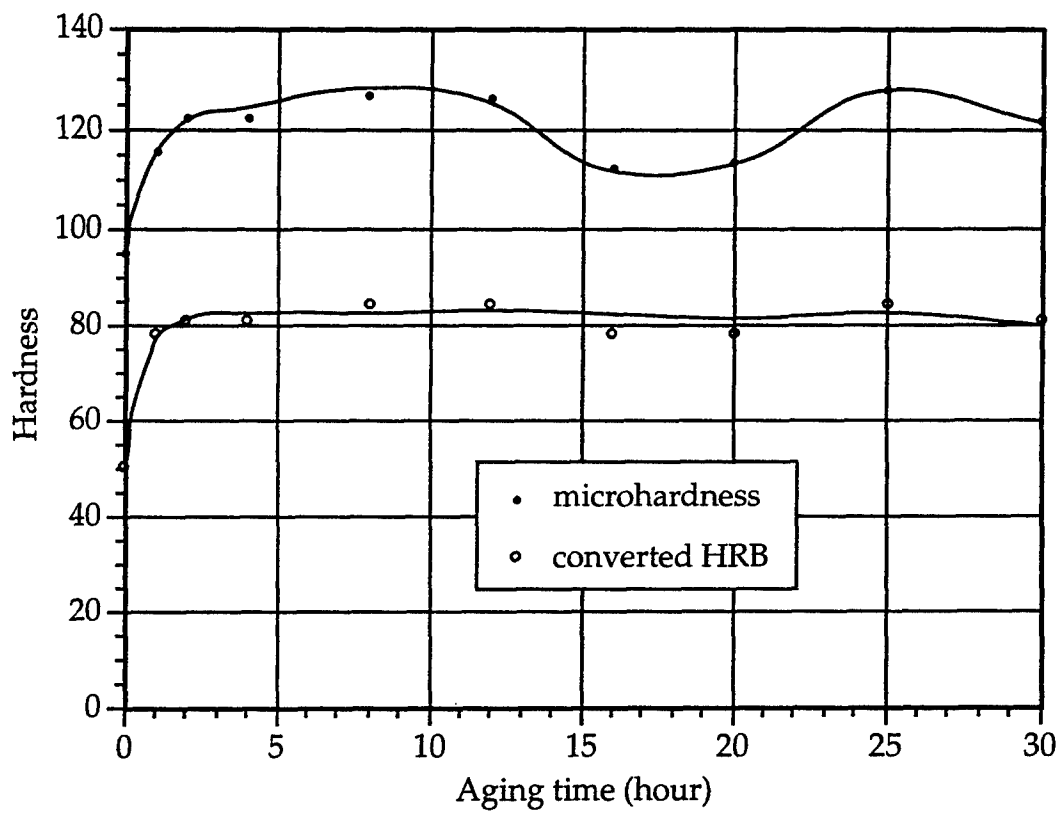


Figure 2.27 Converted results from microhardness (10 gram load) to HRB.

hour aging. Hence, it was assumed that there were at least two hardening agents which had precipitated in the matrix at different stages of the aging treatment. Although the δ' phase is a well known strengthening agent in Al-Li alloys, the contribution of the δ' phase to the strengthening of Al-Li-Cu-Mg alloys has sometimes been ignored as compared to the other strengthening phases, such as the S' phase. Because the δ' and S' phases form at different stages during aging, it is essential to distinguish the strengthening contribution from these two phases in order to fully understand the aging response of Al-Li-Cu-Mg Alloys.

2.4.2.1. The δ' Phase Strengthening Potency

As an ordered phase with a fully coherent interface with the α matrix in aluminum alloys, the δ' phase may strengthen the materials through three sources: coherency hardening (strain hardening), modulus hardening and ordering hardening. The magnitude of these hardening mechanisms varies in different types of precipitate. In the δ' phase, the effect of ordering hardening is well recognized. The coherency hardening is usually considered negligible because of the small constrained misfit ($\sim 0.08\%$) between the δ' phase and the α matrix. As to the modulus strengthening, although there is a considerable difference between the moduli of the δ' phase and the α matrix, there are different opinions on the effectiveness of modulus hardening for the δ' phase. Huang and Ardell [34] indicated that the modulus difference between the δ' phase and the α matrix could be as high as 6 GPa (with the α matrix modulus $G_m \sim 30$ GPa and the δ' phase modulus $G_{\delta'} \sim 35.85$ GPa). This could cause a maximum interaction force with dislocations, due to the difference of moduli, F_G , around 0.06 N/m which is about one third of the

interaction force provided by order hardening, F_O , 0.15 N/m (J/m²). Hence, by comparing the magnitudes of different strengthening mechanisms, the modulus strengthening effect of the δ' phase does not seem to be negligible. However, the analysis from Schueller et al [47] indicated that the strengthening effects from the different mechanisms were not simply additive if they functioned at different dislocation penetrating stages. In the early aging stage, the maximum order hardening result is obtained when the dislocations are near the center of the δ' precipitate. On the other hand, the modulus hardening occurs when the dislocations are near the interfaces of these precipitates. Therefore, these two strengthening results are not additive in the early stage of aging. The strengthening result depends on the stronger mechanism, which is order hardening. However, near peak aging stage, Huang and Ardell [34] argued that the dislocations are highly bowed inside the δ' particles and the maximum F_O can be achieved when most of the dislocation segment within the precipitates are still near the interfaces. Therefore, the modulus hardening should be added to order hardening. Hence, at peak aging stage, the overall resistance to the dislocation movement, F_m , is:

$$F_m = F_O + F_G \quad (2.4)$$

Brown and Ham [48] indicated that for strong, randomly spatially distributed point obstacles, the critical resolved shear stress (CRSS) τ is generally given by the equation:

$$\tau = \frac{F_m}{bL} \quad (2.5)$$

where b is the Burgers vector and L is the effective obstacle spacing along the dislocation as it shears the obstacles.

For practical estimation purpose, Huang and Ardell [34] indicated that the semi-empirical equation:

$$\Delta\tau_{\delta'} = \frac{0.95 \gamma_{apb} \sqrt{f_{\delta'}}}{(2.75 - 2 \sqrt{f_{\delta'}}) b} \quad (2.6)$$

closely describes the resistance to particle shearing near peak aging stage, where, γ_{apb} is the anti-phase boundary energy caused by δ' phase shearing and $f_{\delta'}$ is the volume fraction of δ' precipitates. In this equation, the δ' phase volume fraction is the only parameter which will change during aging. The volume fraction of the δ' phase has been measured and presented in figure 2.8. By substituting the data in figure 2.8 into equation (2.6), the strengthening effects at different aging times have been obtained. These results are presented in figure 2.28. A strengthening peak is clearly seen at the aging time of 8 hours, which is in excellent agreement with the microhardness results in figure 2.1.

The above argument is based on the particle shearing mechanism. Another possible mechanism for precipitate hardening is Orowan looping. This usually occurs at the later stage of hardening when the particles are too large to be sheared and the precipitate coarsening has left the interparticle spacing large enough for dislocations to by pass with less resistance. Theoretically, a strengthening peak occurs when the shearing mechanism is transferring to looping. To see if the first aging peak also corresponds to this transferring, the strengthening effect coming from the looping mechanism has also been calculated. For equiaxed particles of diameter, d , the Orowan looping resistance is given in the following [49]:

$$\Delta\tau_{loop} = \frac{0.81 G_m b}{2\pi \sqrt{(1-\nu)}} \left(\frac{\ln(d/b)}{0.615 d \sqrt{2\pi/3f} - d} \right) \quad (2.7)$$

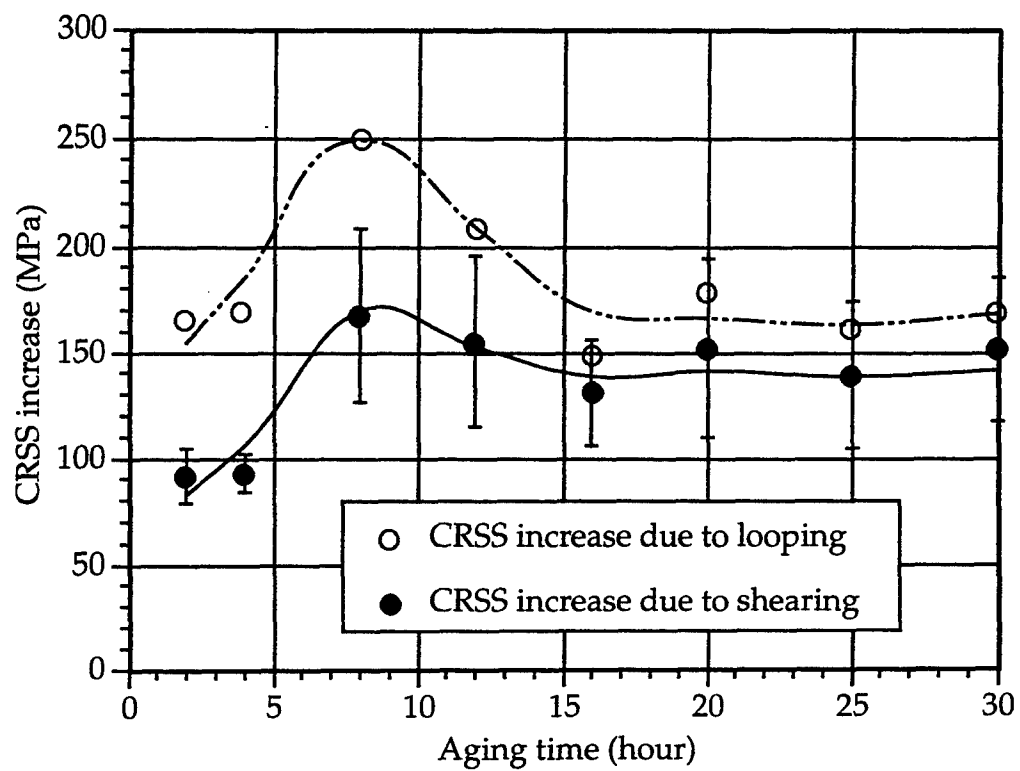


Figure 2.28 Strengthening contribution of the δ' phase to CRSS due to the shearing and the looping mechanisms.

where, $G_m = 30$ GPa is the shear modulus of the α matrix and $\nu=0.339$ is Poisson's ratio of the Al-Li α matrix [34]. The Orowan looping resistance, $\Delta\tau_{loop}$, changes with both the volume fraction and the size of the precipitates. $\Delta\tau_{loop}$ is plotted in figure 2.28 together with the shearing strengthening result $\Delta\tau_{\delta'}$. Somewhat unexpectedly, the looping mechanism always provides a higher resistance to dislocation movement for all aging times. Hence, it can be concluded that the peak strengthening is exclusively caused by the δ' volume fraction change. In addition, TEM examination also supports this finding of the shearing mechanism. Figure 2.29 is a CDF image of some sheared δ' particles taken from a sample aged for 12 hours, which corresponds to the overaging stage after the first aging peak. This sample was made from a specimen deformed to $\sim 3\%$ after 12 hours of aging. The slip plane traces are clearly seen in the δ' particles in figure 2.29.

The most important point is that the calculation results presented in figure 2.28 indicate that the precipitation of the δ' phase in 8090 can increase the CRSS by 100 MPa or more.

2.4.2.2. Strengthening Effects of the S' Phase

Figure 2.28 indicates that the strengthening of the δ' phase achieves a maximum at 8 hours of aging. After that, the strengthening effectiveness of the δ' precipitates decreases. In addition, as it has already been observed, the S' precipitates starts to form within the matrix after 4 hours, the content of Cu and Mg in the α matrix is expected to decrease. Considering the strong solid solution hardening function of Cu, this will further decrease the strength or hardness. Without contribution from other strengthening resources, a strength/hardness drop would be expected. In fact, as indicated by the

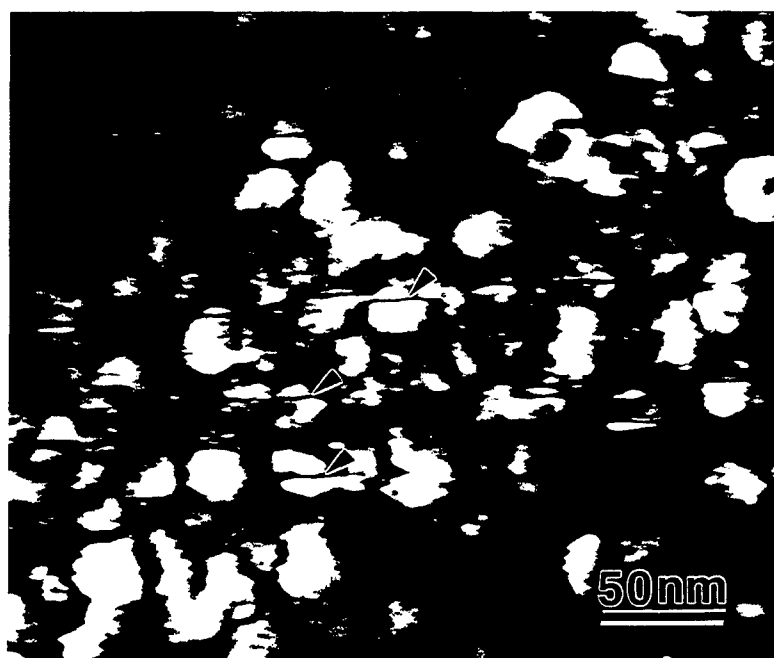


Figure 2.29 Slip line trace (arrowed) in a sample aged for 12 hours.

microhardness results in figure 2.1, there is indeed a slight hardness drop observed after 8 hours. However, the hardness started to climb up again quickly and exhibits the second aging peak at the aging time about 25 hours. TEM observation reveals that the S' phase is the only precipitate which can account for the second hardening. Besides the δ' and S' phase, the other possible strengthening phases in this alloy, such as, the T1 and θ' phases have not been observed in significant amount, especially before 25 hours. After 25 hours of aging, the S' laths have developed to a considerable size. Figure 2.30 shows the size of some S' laths by their cross section. According to the conclusion in Blankenship's study [50], when the "diameter" of the S' precipitates exceeds 2 nm, these precipitates will no longer be sheared by dislocations. Therefore, after 25 hour aging, the S' phase is expected to play an important role in the strengthening of the 8090 alloy.

It is also noticed that although the strengthening potency of the S' phase is very strong, the volume density of S' precipitates in this 8090 alloy is very low as compared to the δ' precipitates. In this study, the quantitative study on the volume fraction change as a function of aging times was not carried out because the inhomogeneous distribution of the S' precipitates made it very difficult to calculate the number density of this phase. However, Xia and Martin's work [21] provided some quantitative data on the precipitation of the S' phase. Their results indicate that for an 8090 alloy with a treatment close to the one in this thesis study, the volume fraction of the S' is 0.23% after 24 hour aging at 190°C. From figure 2.30, it can be estimated that the average cross section size of type B S' precipitates is around $5 \times 10 \text{ (nm)}^2$, which corresponds an equivalent circle diameter of $d = \sqrt{\frac{4 \times 5 \times 10}{\pi}} \approx 8 \text{ nm}$. For

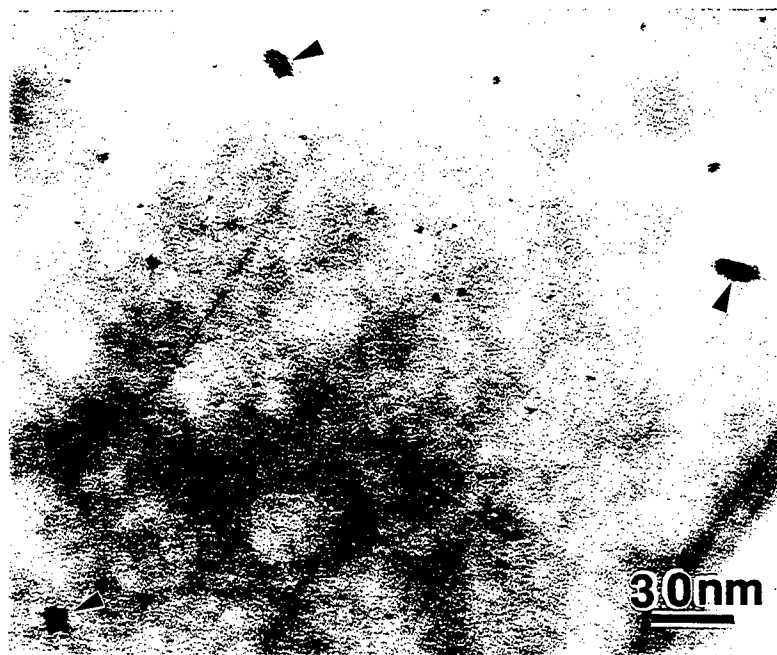


Figure 2.30 S' laths viewed with beam direction = $[100]_{\alpha}$ parallel to the longitudinal axis of the precipitates. The cross section size of S' precipitates is shown. 25 hour aging.

the same volume fraction and number density, the interparticle spacing is different for equiaxed particles and rod precipitates [51]. Equation (2.7) which is suitable for equiaxed precipitates is not applicable for the estimation of the strengthening of rod-like S' precipitates. The derivation of the calculation of S' strengthening starts with the Orowan equation for point obstacles [48, 52]

$$\tau_o = \frac{0.81(2\Gamma)}{bL_s} \quad (2.8)$$

where b is the Burgers vector. L_s is the square lattice spacing, which is defined as:

$$L_s = N_s^{-1/2} \quad (2.9)$$

and N_s is the number of precipitates per unit area intersecting the slip plane. For rod-like precipitates, Fullman's derivation [51] indicated that:

$$N_s = \frac{2f}{\pi d^2} \quad (2.10)$$

where f is the volume fraction of precipitates, d is the diameter of the precipitate rod. Γ in equation (2.8) is the line tension of the dislocations, which is given by Brown and Ham, [48] as:

$$\Gamma = \frac{Gb^2}{4\pi(1-\nu)^{1/2}} \ln \frac{R}{r_o} \quad (2.11)$$

where R and r_o are outer and inner cut-off radii. According to Ardell [52] and Kelly [53], $R \approx \sqrt{2} d$ for precipitate rods and $r_o \approx 2b$. Substituting equations (2.9) to (2.11) and the other parameters defined above into equation (2.8), the Orowan stress for precipitate rods becomes:

$$\tau_o = \frac{0.81G_m b}{2\pi(1-\nu)^{-1/2}} \left(\frac{2f}{\pi d^2} \right)^{1/2} \ln \left(\frac{\sqrt{2}d}{2b} \right) \quad (2.12)$$

with $f=0.23\%$ and $d=8.0$ nm, the Orowan strength generated by S' precipitates is approximately 20 MPa. In Xia and Martin's study [21], the S' precipitates

with the morphology of type C were never mentioned. Therefore, the 0.23% of S' precipitates after 24 hour aging very likely represents only S' precipitates belonging to type A and type B. Considering S' type C will also contribute to the strengthening of the 8090 alloy after 25 hour aging, the practical strengthening effect from the S' phase should be larger than 20 MPa. Comparing the strengthening result from the S' phase with that of the δ' phase at 25 hour aging, it can be seen that the δ' phase is still the primary strengthening phase in the 8090 alloy. The major contribution of the S' phase to the property improvement after 25 hour aging is dispersing plastic deformation in the material.

2.4. CONCLUSIONS

1. The δ' and S' phases are the principal strengthening precipitates in the 8090 alloy aged at 190°C.
2. The δ' phase is the only phase responsible for the strengthening effect at the earlier stage (<8 hours) of the aging. With the precipitation of the S' precipitates at the later aging stage, the strengthening effect has been sustained. This gives 8090 alloy good aging stability at 190°C.
3. The δ' precipitates can be sheared during plastic deformation even after its strengthening peak.
4. Due to the low volume fraction of the S' phase, S' is more considered as a localized deformation inhibitor than a strengthening phase in the aging range employed in the present study.
5. The T2 phase and its co-product, δ' PFZs, have been observed primarily at high angle grain boundaries. The S' distribution is not affected by grain

boundary precipitation although the depletion of vacancies near boundaries may suppress the S' precipitation at the later stage of aging.

2.5. REFERENCES

1. Pearson's Handbook of Crystallographic Data for Intermetallic Phases, 2, 2nd edition, (1991), P. Villars and L. D. Calvert eds.
2. R. Gronsmky: *Aluminum Alloys-Contemporary Research and Applications*, A. K. Vasudevan and R. D. Doherty, eds., p370.
3. T. Sato and A. Kamio: *Aluminum-Lithium*, Paper presented at 6th International Aluminum-Lithium Conference, M. Peter and P.-J. Winkler, eds., Garmisch-Partenkirchen, Germany, (1991), p57.
4. G. Schmitz and P. Haasen: *Acta metall.*, 40, (1992), p2209.
5. S. F. Baumann and D. B. Williams, *Metall. Trans.*, 16A, (1985), p1203.
6. V. Mahadev, K. Mahalingam, G. L. Liedl and T. H. Sanders Jr.: *Acta metall.*, 42, (1994), p1039.
7. D. de Fontaine, *Acta metall.*, 23, (1975), p553
8. W. A. Soffa and D. E. Laughlin: *Acta metall.*, 37, (1989), p3019
9. V. Radmilovic, A. G. Fox and G. Thomas; *Acta metall.*, 37, (1989), p2385.
10. O. Jensrud and N. Ryum: *Mater. Sci. Eng.*, 64, (1984), p229.
11. A. K. Vasudevan and R. D. Doherty: *Acta metall.*, 35, (1987), p1193.
12. K. S. Prasad, A. K. Mukhopadhyay, A. A. Gokhale, D. Banerjee and D. B. Goel: *Scratta Metall.*, 30, (1994), p1299.
13. P. Sainfort and P. Guyoy: *Aluminum-lithium Alloys III*, C. Baker, P. L. Gregson, S. J. Harris and C. J. Peel, eds., Inst. of Metals, London, (1986), p420

14. J. C. Huang and A. J. Ardell: *J. de Physique, supplément*, 48, C3, (1987), p373.
15. P. Sainfort and B. Dubost: *J. de Physique*, 47, C3, (1986), p321.
16. P. J. Gregson and H. M. Flower: *Acta metall.*, 33, (1985), p527.
17. W. S. Miller, M. P. Thomas, D. J. Lloyd and D. Creber: *Mater. Sci. Tech.*, 2, (1986), p1210.
18. F. S. Lin, S. B. Chakraborty, and E. A. Starke, Jr.: *Met. Trans.*, 13A, (1982), p401.
19. R. J. Rioja, P. E. Bretz, R. R. Sawtell, W. H. Hunt, and E. A. Ludwiczak: *Aluminum Alloys, Their Physical and Mechanical Properties*, III, E. A. Starke, Jr. and T. H. Sanders, Jr., eds. (1986), p1781.
20. M. Ahmad and T. Ericsson: *Aluminum-Lithium Alloys III*, Proc. 3rd International Aluminum-Lithium Conference, C. Baker, P. J. Gregson. S. J. Harris and C. J. Peel eds., Inst. of Metals, London, (1986), p509.
21. X. Xia and J. W. Martin: *Mater. Sci. Eng.*, A128, (1990), p113.
22. B. Dubost, J. M. Lang and F. Degreve: *Aluminum-Lithium III*, Proc. 3rd International Aluminum-Lithium Conference, C. Baker, P. J. Gregson. S. J. Harris and C. J. Peel eds., Inst. of Metals, London, (1986), p355.
23. P. J. Gregson and S. A. Court: *Scripta Metall.*, 30, (1994), p1359
24. S. Suresh, A. K. Vasudevan, M. Tosten and P. R. Howell: *Acta metall.*, 35, (1987), p25.
25. S. Song, W. Zhang, J. Cheng, E. R. Ryba and P. R. Howell: *Mater. Letters*, 2, (1990), p430.
26. D. M. Knowles and J. E. King: *Acta metall.*, 39, (1991), p793.
27. W. Stimson, M. H. Tosten, P. R. Howell and D. B. Williams: *Aluminum-Lithium Alloys III*, Proc. 3rd International Aluminum-Lithium

- Conference, C. Baker, P. J. Gregson, S. J. Harris and C. J. Peel eds., Inst. of Metals, London, (1986), p386
28. F. W. Gayle and J. B. Vander Sander, *Scripta Metall.*, 18, (1984), p473.
 29. P. L. Makin and B. Ralph, *J. Mater Sci.*, 19, (1984), p3835.
 30. P. J. Gregson and H. M. Flower: *J. Mater Sci. Letter.*, 3, (1984), p829.
 31. M. H. Tosten, J. M. Galbraith and P. R. Howell: *J. Mater Sci, Letters*, 6, (1987), p51.
 32. I. M. Lifshitz and V. V. Slyozov: *J. Phys. Chem. Solids*, 19, (1961), p35
 33. C. Wagner: *Zeitschrift fur Elektrochemie*, 65, (1961), p581.
 34. J. C. Huang and A. J. Ardell: *Acta metall.*, 36, (1988), p2995.
 35. P. Gomiero, F. Livet, Y. Brechet and F. Louchet: *Acta metall.*, 40, (1992), p847.
 36. K. Mahalingam, B. P. Gu, G. L. Liedl and T. H. Sanders Jr.: *Acta metall.*, 35, (1987), p483.
 37. Y. A. Bagaryatskii: *Zhm. Tekhn. Eiziki Fulmer Res. Inst. Trans. Nos.* 11, 12, 55, 66, (1948).
 38. J. M. Silcock: *J. Inst. Metals*, 89, (1961), p203
 39. G. C. Weatherly and R. B. Nicholson: *Phil. Mag.*, 17, (1968), p801.
 40. J. Yan: *J. Mater. Sci. Letters*, 10, (1991), p591.
 41. V. Radmilovic, G. Thomas, G. J. Shiflet, and E. A. Starke: *Scripta Metall*, 23, (1989), p1141.
 42. M. Ahmad and T. Ericsson: *Scripta Metall.*, 19, (1985), p457.
 43. P. R. Howell, D. J. Michel and E. Ryba: *Scripta Metall.*, 23, (1989), p825.
 44. M. H. Tosten, A. S. Ramani, C. W. Bartges, D. J. Michel, E. Ryba and P. R. Howell: *Scripta Metall.*, 23, (1989), p829.

45. S. C. Jha, T. H. Sanders, Jr., and M. A. Dayananda: *Acta metall.*, 35, (1987), p473.
46. LECO Hardness Relationship Scale Chart, Form No. 200-971 and 200-976-009.
47. R. D. Schueller, F. E. Wawner: *J. Mater. Sci.*, 29, (1994), p239.
48. L. M. Brown and R. K. Ham: *Strengthening Methods in Crystals*, A. Kelly and R. B. Nicholson eds., Halsted Press Div. Wiley, New York (1971), p9.
49. J. W. Martin: *Micromechanism in Particle-Hardened alloys*, Cambridge University Press, Cambridge, UK, (1980), p62.
50. C. P. Blankenship Jr.: *PhD dissertation*, University of Virginia, (1992).
51. R. L. Fullman: *Trans. AIME*, 197, (1953), p447.
52. A. J. Ardell: *Met. Trans.*, 16A, (1985), p2131.
53. P. M. Kelly: *Scripta Metall.*, 6, (1972), p647.

CHAPTER 3

A STUDY ON THE PRECIPITATION BEHAVIOR OF THE S' (Al₂CuMg) PHASE

3.1 BACKGROUND

The S' phase (Al₂CuMg) forms in Al-Cu-Mg alloys when the atomic ratio of Mg : Cu > 3. The strengthening potency of this phase has been proven by previous studies [1-4] and it has a powerful ability in dispersing localized deformation. These benefits from the S' phase have been used to design a series of Al-Li-Cu-Mg alloys, in the hope that the poor ductility and toughness of the binary Al-Li alloys would be improved with the formation of S' precipitates.

Because of its favorable effects on the mechanical properties of aluminum alloys, the precipitation of the S' phase has been the topic of many previous studies [4-11]. However, little attention has been paid to the details of the precipitation behavior. These details are examined in this chapter. As quoted earlier in chapter 2, the orientation relationship of the S' phase with respect to the α aluminum matrix was shown by Bagaryatskii [5] and Silcock [6] to be:

$$\{100\}_{S'} \parallel \{100\}_{\alpha}$$

$$\langle 010 \rangle_{S'} \parallel \langle 021 \rangle_{\alpha}$$

$$\langle 001 \rangle_{S'} \parallel \langle 0\bar{1}2 \rangle_{\alpha}$$

and it has been shown by high resolution electron microscopy (HREM) [10, 11] that the S' phase forms with $\{210\}_{\alpha}$ as habit planes. In Weatherly and Nicholson's study [8], the individual S' precipitates were observed to be rod-like and to have their longitudinal axes parallel to the $\langle 100 \rangle_{\alpha}$ directions. They suggested that the

lateral interfaces of these rods were fully coherent with the α matrix at the early stage of the precipitation reaction and that coherency loss occurred as the S' rods grew to a larger length. Interfacial strain always accompanies the precipitation of the S' phase because of the coherency at the S'/ α interfaces. Hence, S' precipitates tend to nucleate at e.g., dislocations and subboundaries. Wilson and Partridge [7] observed that S' precipitates at dislocations formed corrugated sheets due to the different variants nucleated at the same dislocation. Corrugated sheets are considered to be a typical feature of the S' phase in Al-Cu-Mg alloys. In Al-Li-Cu-Mg alloys, in addition to the S' precipitates nucleated at dislocations, Gregson et al. [4, 9] observed uniformly distributed S' within the matrix. These uniformly distributed S' precipitates were much finer as compared to those nucleated at dislocations.

During the present study of the aging behavior of the 8090 alloy, some new information regarding the precipitation of the S' phase has been obtained. The results and the related discussion are presented in the following sections.

3.2 INTERFACIAL COHERENCY AND THE GEOMETRIC SHAPE OF THE S' PHASE

3.2.1 S'/ α Interfacial Coherency

The geometric shape of individual S' precipitates has been observed as lath or rod-like in the present study as well as in other previous research [8]. A model of such an S' lath and the definition of the **a**, **b** and **c** axes were schematically shown earlier in figure 2.10 and is reproduced here, with its spatial orientation with respect to the α matrix, in figure 3.1. The factors determining the geometric shape of individual S' precipitates are discussed in the following. It should be noted that this is the first study to fully characterize the morphology of the S' phase.

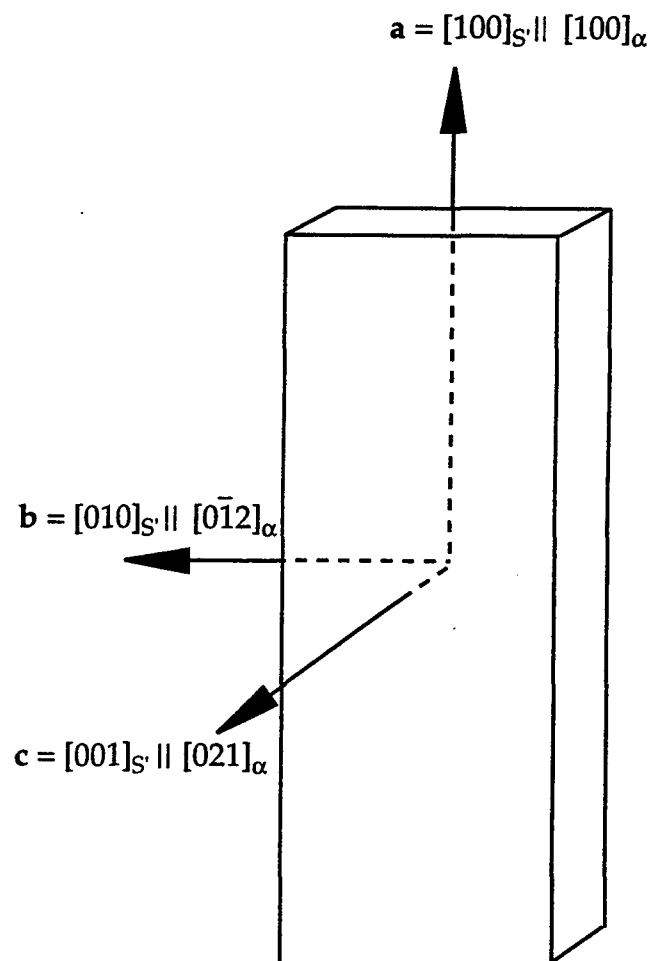


Figure 3.1 Model of a S' lath and its orientation with respect to the α matrix.

The geometric shape of a precipitate formed within the matrix largely depends on the precipitate/matrix interfacial coherency. Experiment evidence indicates that the S' phase has $\{210\}_\alpha$ as the habit planes [10, 11] and the lateral S'/ α interfaces are composed of $(010)_{S'}$ and $(001)_{S'}$ planes which are parallel to $(021)_\alpha$ and $(0\bar{1}2)_\alpha$ planes, respectively. The coherency of S'/ α interfaces has been evaluated by the misfit along the a, b and c axes of the S' phase in previous studies [7, 8]. For example, based on the quoted OR, Wilson and Partridge [7] calculated the periodicity values along the three axes of the S' phase and estimated the misfits in these directions as quoted in table 3.1

Table 3.1 Quoted Misfits between the S' Phase and the α Matrix [7]

Interplanar spacing (Å)		Misfit % relative to Al
Al	S'	$\delta = \left(\frac{nd_{Al} - d_{S'}}{nd_{Al}} \right) \times 100$
$d_{100}=4.05$	$a=4.00$	$(n=1) +1.23$
$d_{021}=0.906$	$b=9.23$	$(n=10) -1.88$
$d_{012}=0.906$	$c=7.14$	$(n=8) +1.49$

From these results, Wilson and Partridge concluded that except for the a axis of the S' phase, the misfits for the other two S' axes were considerable. Hence, the S' phase would grow faster along the a axis and develop a lath/rod-like shape.

However, since most intermetallic unit cells contain a large number of atoms and the exact location of these atoms are frequently not at the corners, face centers or cell centers of each unit cell, the conclusion about the coherency of the α /S' interfaces could be misleading if only the periodicity between limited directions were compared between the two phases. Interfacial coherency between two phases depends on the atom matching of all the atoms at the interfaces. To obtain a reliable conclusion on the interfacial coherency at S'/ α

interfaces, the atom matching on the $(100)_{S'}$, $(010)_{S'}$ and $(001)_{S'}$ planes and the corresponding planes in the α matrix has been evaluated by comparing atom maps on these three pairs of planes.

An S' unit cell with all the Al, Cu and Mg atoms in the proper positions and an f.c.c. unit cell of the α matrix are drawn in figures 3.2a and b, respectively. The coordination of each atom in the S' unit cell is listed in table 3.2. Atom matching on $(100)_{S'} \parallel (100)_{\alpha}$, $(010)_{S'} \parallel (021)_{\alpha}$ and $(001)_{S'} \parallel (0\bar{1}2)_{\alpha}$ planes is then evaluated.

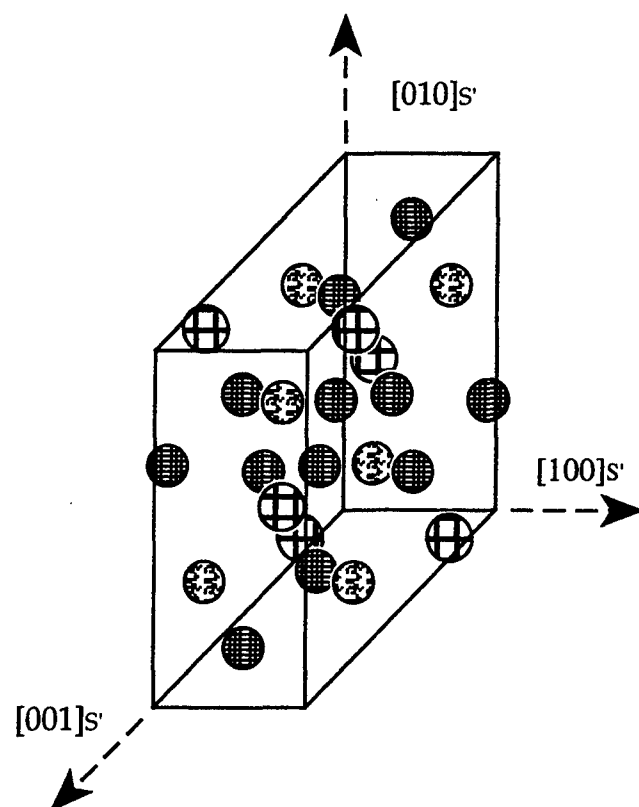
The atom arrangement on $(100)_{S'}$ and $(100)_{\alpha}$ planes is shown schematically in figures 3.3a and b. To make the comparison more directly, the planes shown in figure 3.3a are taken from one unit cell of the S' phase at different x coordination. Conversely, the plane in figure 3.3b crosses several α matrix unit cells. The comparison indicates that on this plane, although the misfit between $[010]_{S'}$ and $[021]_{\alpha}$ is $\sim 1.9\%$, the misfit is 21% between $[001]_{S'}$ and $[0\bar{1}2]_{\alpha}$. In addition, on the $(100)_{S'}$ planes, most of the atoms will not be able to match with the atoms on the $(100)_{\alpha}$ plane. The interface between $(100)_{S'}$ and $(100)_{\alpha}$ is not likely to be coherent.

Figures 3.4a and b compare the atom arrangement on $(001)_{S'}$ and $(0\bar{1}2)_{\alpha}$ planes. The misfit is 1.2% between $[100]_{S'}$ and $[100]_{\alpha}$ and 1.9% between $[010]_{S'}$ and $[021]_{\alpha}$. Of the two $(001)_{S'}$ planes shown in figure 3.4a, the atoms on $(0\bar{1}2)_{\alpha}$ are able to achieve a good match with the $(001)_{S'}$ at $z = 0.056$. The S' phase and the α matrix should be able to form a coherent interface during the nucleation and the early stage of growth. The interfacial energy is expected to be much lower than the just discussed interface between $(100)_{S'}$ and $(100)_{\alpha}$ planes.

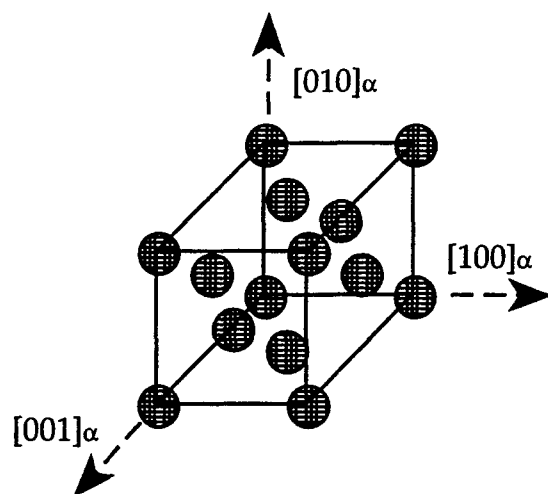
Finally, the atom matching between $(010)_{S'}$ and $(021)_{\alpha}$ is compared in figures 3.5a and b. The matching along the $[100]_{S'} \parallel [100]_{\alpha}$ yields misfit of 1.2% and no unmatched atoms left in this direction. The misfit along $[001]_{S'} \parallel [0\bar{1}2]_{\alpha}$ is 21%. In

Table 3.2 Atoms in the S' Unit Cell

Atom Number	x	y	z	Atom Type
1	0.0	0.778	0.25	Cu
2	0.0	-0.778	0.75	Cu
3	0.5	0.278	0.25	Cu
4	0.5	-0.278	0.75	Cu
5	0.0	0.072	0.25	Mg
6	0.0	-0.072	0.75	Mg
7	0.5	0.572	0.25	Mg
8	0.5	0.428	0.75	Mg
9	0.0	0.356	0.056	Al
10	0.0	-0.356	-0.056	Al
11	0.0	0.356	0.444	Al
12	0.0	-0.356	0.556	Al
13	0.5	0.856	0.056	Al
14	0.5	0.144	-0.056	Al
15	0.5	0.856	0.444	Al
16	0.5	0.144	0.556	Al



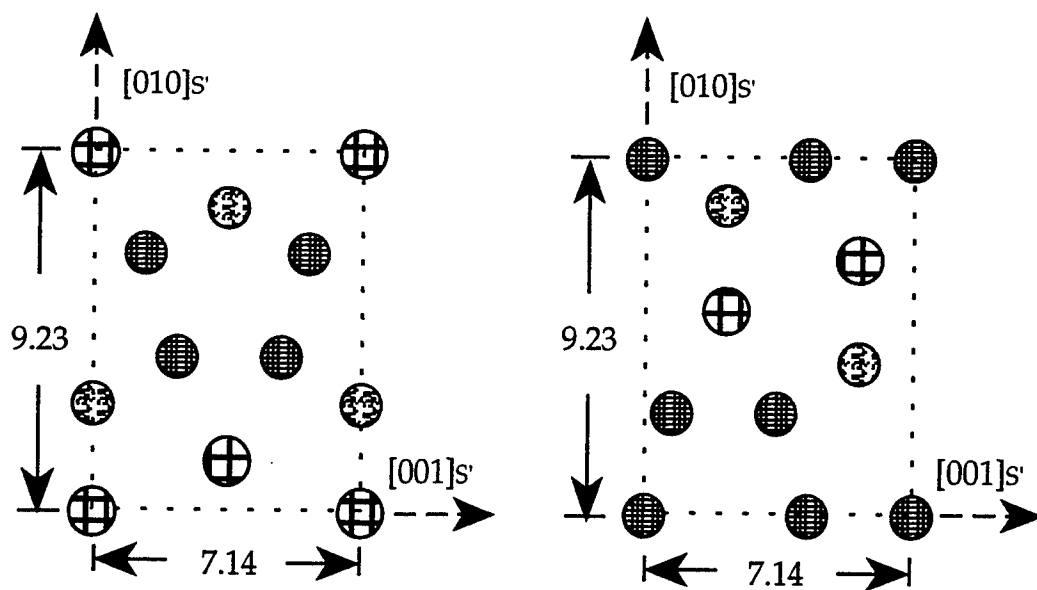
(a) orthorhombic unit cell of the S' phase, $a = 4.00\text{\AA}$, $b = 9.23\text{\AA}$, $c = 7.14\text{\AA}$



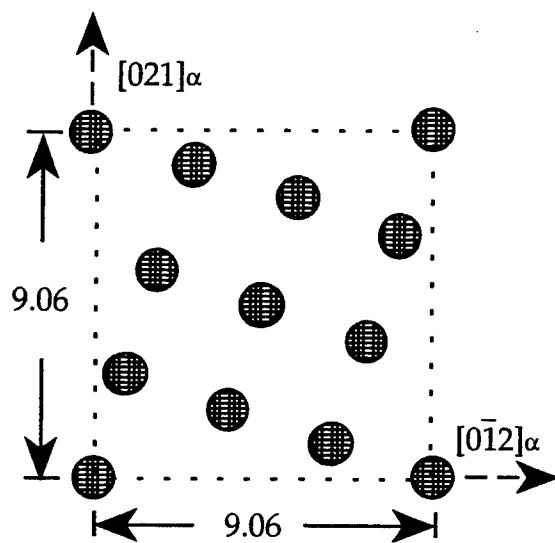
(b) f.c.c. unit cell of the α matrix, $a = b = c = 4.05\text{\AA}$

Figure 3.2 Unit cells of the S' phase and the α matrix

Atom type:  Al,  Cu,  Mg.



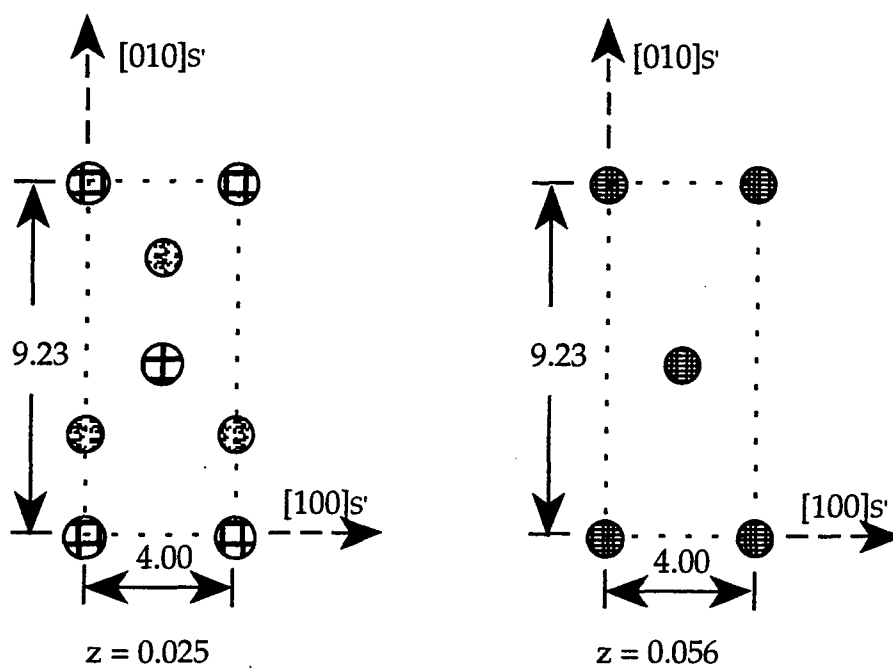
(a) atom location patterns on $(100)_{s'}$ planes



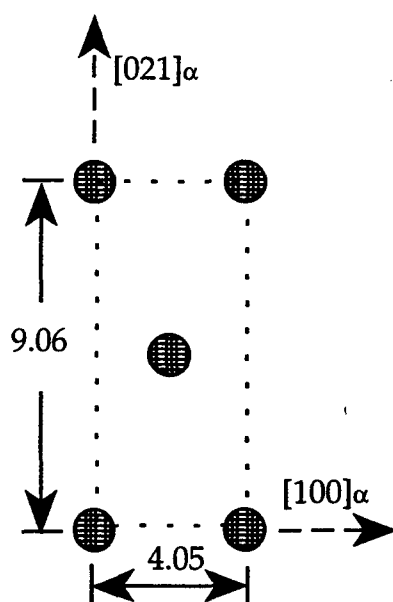
(b) atom locations on $(100)_{\alpha}$ plane

Figure 3.3 $(100)_{s'}/(100)_{\alpha}$ atom maps.

Atom type:  Al,  Cu,  Mg.



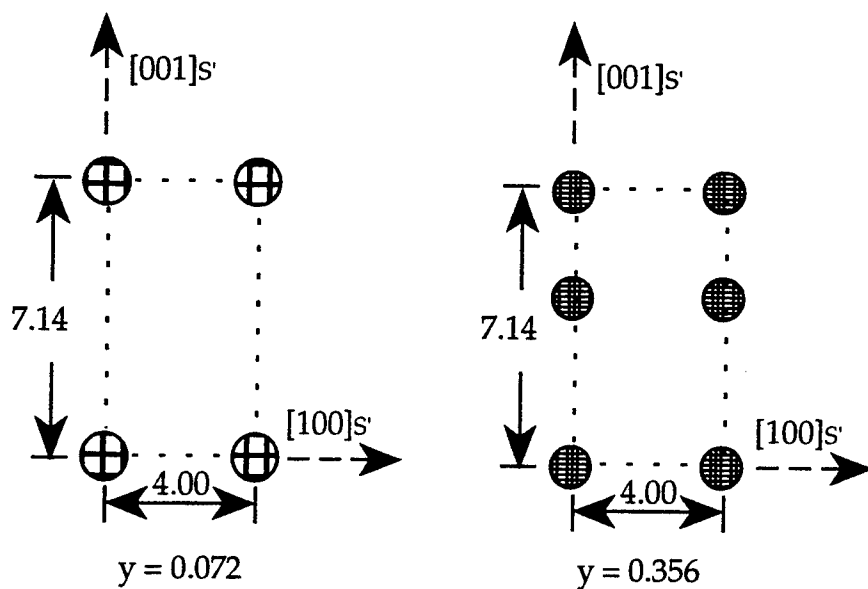
(a) atom locations patterns on two $(001)_{s'}$ planes



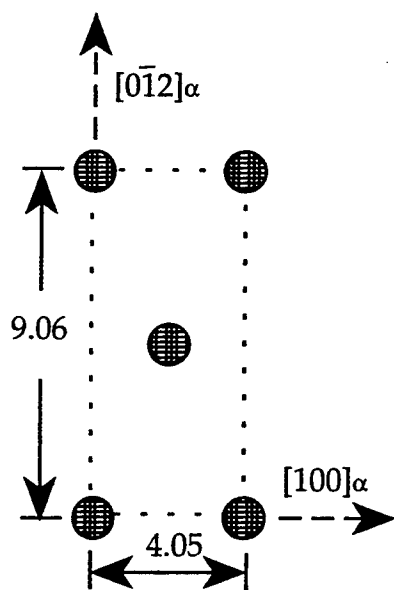
(b) atom locations on $(0\bar{1}2)_{\alpha}$ plane

Figure 3.4 $(001)_{s'}/(0\bar{1}2)_{\alpha}$ atom maps.

Atom type: \bullet Al, \odot Cu, \oplus Mg.




(a) two atom location patterns on $(010)_S$ planes



(b) atom locations on $(021)_\alpha$

Figure 3.5 $(010)_S / (021)_\alpha$ atom maps.

Atom type:  Al,  Cu,  Mg.

addition, the center atom on the $(021)_\alpha$ plane is left unmatched. The coherency level at this interface should be lower than that on $(001)_S \parallel (0\bar{1}2)_\alpha$ interface shown in figures 3.4. The interfacial energy on the $(010)_S \parallel (021)_\alpha$ should be higher than the $(001)_S \parallel (0\bar{1}2)_\alpha$ interface but much lower than on $(100)_S \parallel (100)_\alpha$ interface. In addition, the misfit values along the *a*, *b* and *c* axes of the *S'* phase are listed in table 3.3.

Table 3.3 Misfits between the *S'* Phase and the α Matrix along *a*, *b* and *c* Axes of the *S'* Phase

Axis of the <i>S'</i> phase	* Misfit % relative to Al: $\delta = \left(\frac{l_{Al} - l_S}{l_{Al}} \right) \times 100$
a	+1.2
b	-1.8
c	+21

* l_{Al} and l_S are the distances between two neighboring atoms in the specific directions.

From the above, it can be seen that the *S'*/ α interfaces consist of an $(001)_S$ with a considerably high coherency, an almost completely incoherent $(100)_S$ with high interfacial energy and an $(010)_S$ which is partially coherent and has an interfacial energy between $(001)_S$ and $(100)_S$ faces.

S'/ α interfaces were examined by both Radmilovic[10] and Yan [11] using high resolution electron microscopy (HREM). Both studies indicated that the lateral *S'*/ α interfaces consisted of broad faces parallel to $(010)_S / (021)_\alpha$ and $(001)_S / (0\bar{1}2)_\alpha$ planes. These interfaces were either smooth on the atomic scale or contained growth ledges. Radmilovic's HREM result [10] also indicated that there is a 1 to 1 lattice fringe match along the $[010]_S / [021]_\alpha$ direction, which means that the atoms from the both phases achieved a perfect match along this

direction. Although experiment evidence on the atom matching along the $[100]_{S'}/[100]_{\alpha}$ direction has not been reported, as the misfit along $[100]_{S'}/[100]_{\alpha}$ direction is even smaller, it is reasonable to believe that a similar perfect atom match also exists in this direction. Therefore, atoms across the $(001)_{S'}/(0\bar{1}2)_{\alpha}$ interface can achieve a perfect matching. This is in a good agreement with the results obtained from matching the planes in figures 3.4. Yan's HREM results [11] also indicated that the end interfaces, which are normal to $[100]_{S'}$ of the S' laths, are rough and irregular. This is usually the characteristic of incoherent interfaces.

Similar evidence has also been obtained in this thesis study using conventional transmission electron microscopy. Figure 3.6 is a TEM micrograph taken in a sample aged after 120 hours. The beam direction is $[100]_{\alpha}$. Lattice fringes can be resolved in both S' precipitates and the δ' precipitates in this photograph (arrowed). Using the fringes in the δ' phase as a calibration, both the angle between the lattice fringes from the S' precipitates and the α matrix and the fringe spacing in the S' precipitates shows that they are the $(001)_{S'}$ fringes. At the S'/α interfaces, numerous ledges parallel to the $(001)_{S'}$ fringes are visible which implies that these interfaces consist of $(001)_{S'}/(0\bar{1}2)_{\alpha}$ planes. Figure 3.7 shows some other S' precipitates which have a broader smooth interface with less ledges (arrowed). In common with figure 3.6, the fringes in these precipitates indicates that these broad interfaces are the $(001)_{S'}/(0\bar{1}2)_{\alpha}$ planes. Hence, both the experimental results in the present study (figures 3.6 and 3.7) and the HREM studies [10, 11] have achieved good agreement with the theoretical analysis in figures 3.3 to 3.5 in that the S' phase can form coherent or partially coherent interfaces on its (010) and (001) planes, respectively.

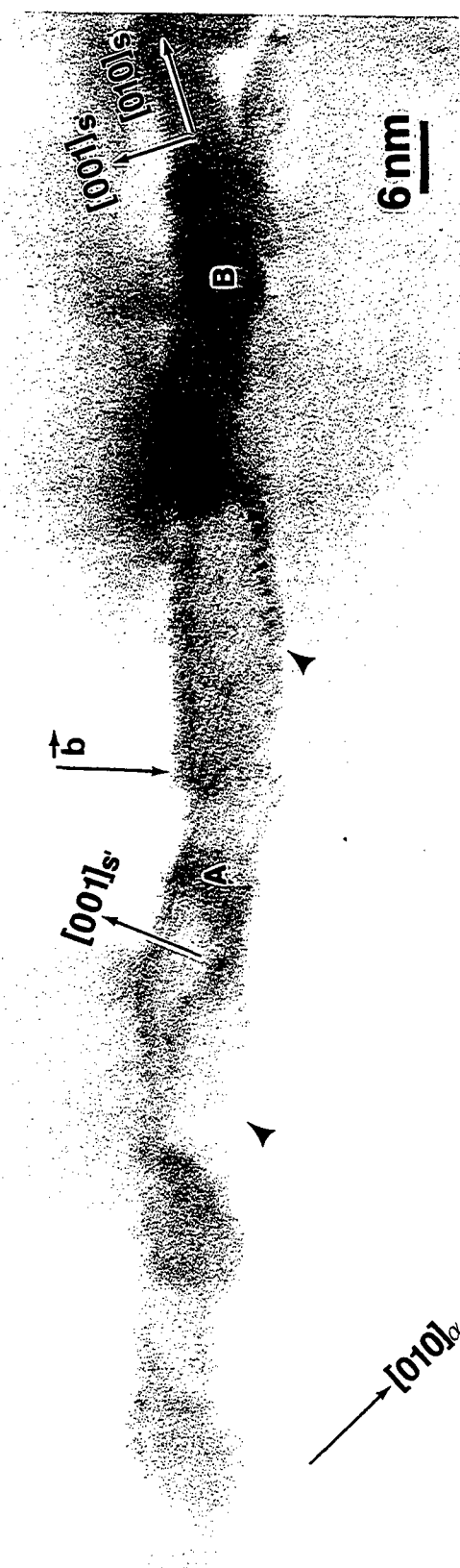


Figure 3.6 High magnification image of the S' precipitates at a dislocation. The $(010)_S$ and $(100)_S$ lattice fringes can be seen. Interfacial ledges are arrowed. $[B] = [100]_\alpha$.

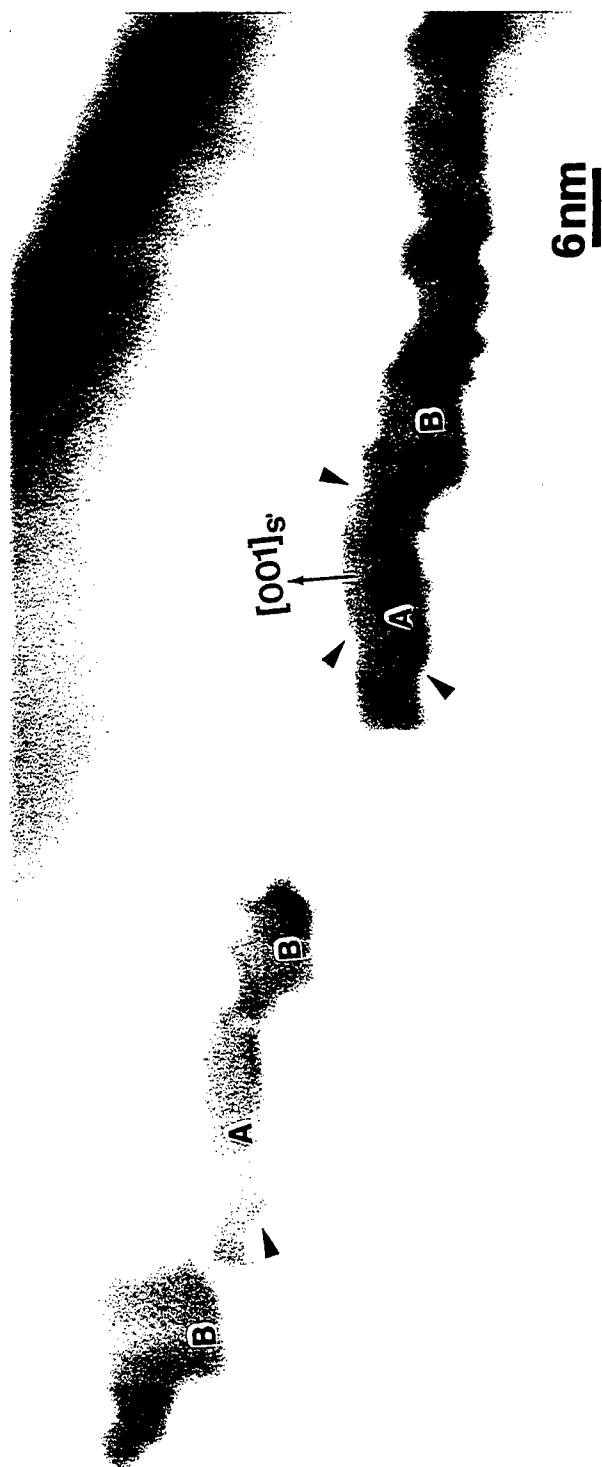


Figure 3.7 Broad faces and growth ledges in S' precipitates. Lath-like (A) and rod-like (B) precipitates can both be seen. $[B] = [100]_\alpha$.

3.2.2. Kinetic Shape of the S' Phase

As already seen from the above section, the coherent $(001)_S \parallel (0\bar{1}2)_\alpha$ and $(010)_S \parallel (021)_\alpha$ interfaces are rather smooth on the atomic scale. Hence, the growth perpendicular to these faces would depend on the lateral ledge growth mechanism, which is sometimes limited by the supply of ledges. On the other hand, the $(100)_S \parallel (100)_\alpha$ interfaces can be rough with easy atom accommodation. Therefore, the very likely incoherent $(100)_S$ interface may grow at a much faster rate than the low energy coherent $(001)_S$ and $(010)_S$ interfaces and the S' phase hence exhibits a lath/rod shape ($a \gg b$ and c). Because $(001)_S$ has a higher coherency than $(010)_S$, it is expected that the growth rate is even lower in the direction of $[001]_S$ than in $[010]_S$. Finally, the kinetic shape of the S' phase should be a lath ($a \gg b > c$), such as the precipitates (A) in figure 3.7. However, due to the impingement of different S' precipitates, rod-like S' precipitates ($a \gg b = c$) are also frequently observed in Al-Cu-Mg alloys, such as precipitates B in figure 3.7. In addition, it is noticed that these rod-like S' precipitates seems to have a better ledge supply so that their apparent lateral interfaces are tilted away from the $(010)_S / (021)_\alpha$ or $(001)_S / (0\bar{1}2)_\alpha$ planes.

3.3. S' NUCLEATION AT DISLOCATIONS

The dislocations in the α matrix provide preferential nucleation sites for the S' precipitation. The high density of S' at dislocations causes the so called "corrugated sheet" morphology, such as those shown in figures 3.8 and 3.9. It is noticed that in figure 3.9, in the vicinity of the dislocation loop, there is a zone free of the small dark imaging entities (S' type C and see section 2.3.2.3). The details of S' precipitation at dislocations are discussed in the following.

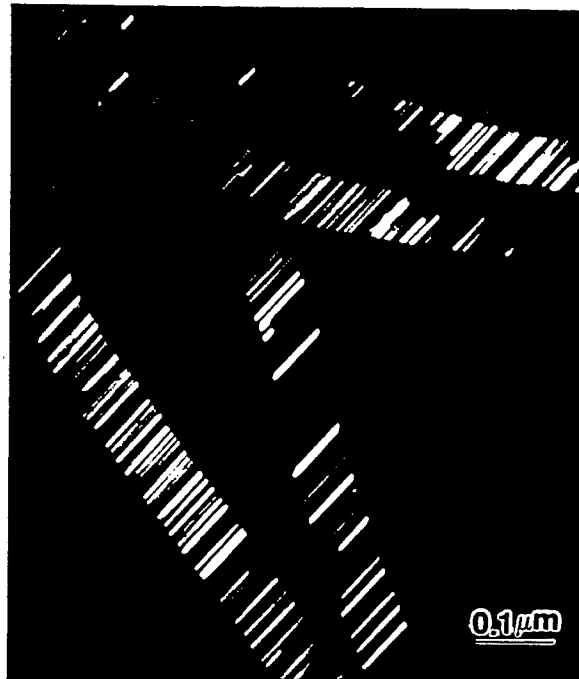


figure 3.8 S' sheet formed by S' nucleated at dislocations.

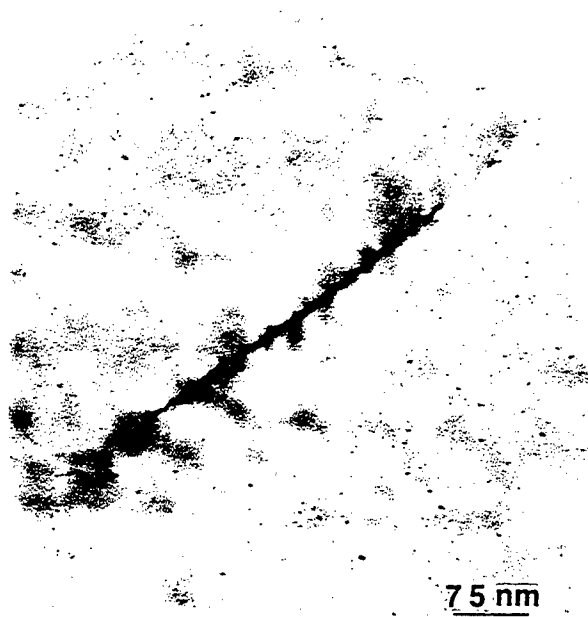


Figure 3.9 Upright view of S' precipitates nucleated at a dislocation loop.
The corrugated nature of the sheet can be seen clearly.
 $[B] = [100]_{\alpha}$.

3.3.1. S' Variants Nucleated at a Dislocation

The driving force for S' nucleation at edge dislocations is that the strain field around the dislocations can compensate for some of the strain at S'/ α interfaces. Because the misfit in different directions of the interfaces are different, the strain relief varies according to the orientation of the S' relative to the Burgers vector, \vec{b} , of the dislocations. As shown in table 3.2, although misfit is present along all a, b and c axes, the misfit along the c axis is the highest. The relief of misfit along c would decrease the strain energy at S'/ α interfaces more than along either the a or b axis.

From the point of view of misfit relief, as long as the c axis of the specific variant has a mutual angle $\neq 90^\circ$ with respect to the Burgers vector \vec{b} , this variant should be energywise favored to nucleate at the dislocation. In aluminum alloys, the dislocations usually have the Burgers vector $\vec{b} = \frac{1}{2} [110]_\alpha$ which has angles $\neq 90^\circ$ with all the 12 variants of S'. Therefore, at first, it might be expected that all 12 variants of S' precipitates would tend to nucleate at a given edge dislocation. However, TEM examination indicates that in most cases, the S' sheet that formed at a dislocation usually consists of only one or two variants of S' precipitates from the same group defined in table 2.1, as shown in figure 3.6. This result can be easily understood while considering the strain relief level of the differently oriented S' precipitates at the same dislocation. For example, if a dislocation has the Burger's vector $\vec{b} = \frac{1}{2} [110]_\alpha$, the misfit of the two variants of S' precipitates whose c axes are parallel to $[120]_\alpha$ and $[210]_\alpha$ have the lowest angle of 18.43° with the \vec{b} and hence the maximum misfit relief. This has also been proved in figure 3.6 by study the fringes in precipitates A and B. The fringes in these two precipitates are evidently from two set of planes with different index. Using the

fringes in the δ' precipitates as the calibration reference, the fringes are determined to be from the $(001)_S$ in precipitate A and from $(020)_S$ planes in precipitate B. Therefore, the c axes ($[001]_S$) of the two precipitates are marked on this micrograph. If the c axis in precipitates A is designated as $[0\bar{1}2]_\alpha$, from the angle between the two c axes, it is known that the c axis in precipitate B is along $[0\bar{2}1]_\alpha$, which is exactly what has been predicted in the analysis above. The other precipitates are believed to belong to one of these two variants. It is very interesting to notice that based on the c axis orientation of these precipitates, the Burgers vector of the dislocation can also be determined as indicated in figure 3.6. This dislocation is almost a pure edge dislocation.

3.3.2. S' Precipitation at Dislocation Loops

3.3.2.1 Dislocation Loop Orientation

Wilson and Partridge [7] observed S' precipitates nucleated at dislocation loops in their study on the precipitation behavior of the S' phase in Al-Cu-Mg alloys. In their study, the dislocation loops were on $\{110\}_\alpha$ planes and the S' precipitates which nucleated at those dislocation loops formed sheets parallel to the $\{110\}_\alpha$ plane, that is, the loop plane. The $\{110\}_\alpha$ oriented S' sheets formed at dislocation loops also form in the 8090 alloy used in the present study, as shown in figure 3.10. Because the beam direction of figure 3.10 is $[001]_\alpha$, the S' laths in this micrograph indicate the $[100]_\alpha$ and the $[010]_\alpha$ directions (marked). In addition, because the beam direction lies within the loop planes, the loop planes are projected on to the image plane as rods. The angle between these rods and the $[100]_\alpha$ direction is $\sim 45^\circ$, which indicates these rods are along the $[110]_\alpha$ direction. It should be pointed that although the angles measured from figure 3.10 only indicate that the projection of the loop planes on the projection plane is

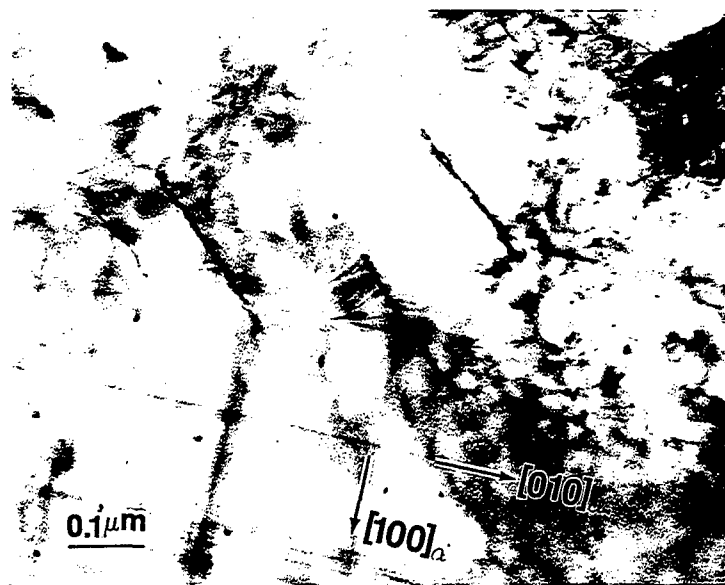


Figure 3.10 S' sheets parallel to dislocation loop plane, $(110)_\alpha$. The $[100]_\alpha$ and $[010]_\alpha$ directions were determined using the S' laths as references. $[B] = [001]_\alpha$.

along $\langle 110 \rangle_\alpha$ directions, with $[001]_\alpha$ as the beam direction, the projections of the $\{1\bar{1}0\}_\alpha$ planes are coincident with $\langle 110 \rangle_\alpha$ directions on the projection plane.

Hence, the $\langle 110 \rangle_\alpha$ directions in the projection plane (micrograph) correspond to the $\{1\bar{1}0\}_\alpha$ planes in the imaged volume of the sample. More generally, at this particular beam direction, $[001]_\alpha$, the $\langle h\bar{k}0 \rangle$ directions on the projection planes always correspond to the $\{hk0\}$ planes in the sample. This is discussed further in Appendix III.

In addition, dislocation loops on planes other than the $\{110\}_\alpha$ have been frequently observed in the present study. Figures 3.11a and b are two S' CDF images taken from the 8090 alloy. The angles between the projections of the loops and the $[100]_\alpha$ directions have been measured. The angles between the loop projections and the S' laths fall into the range of 22° to 28° , which generate a mean angle value of 25° . This is very close to the angle between the $[210]_\alpha$ and the $[100]_\alpha$, which is 26.57° . The deviation of the measured angles from the exact angle between the $[210]_\alpha$ and the $[100]_\alpha$ directions could be due to the measurement error, especially with precipitates lying on the loops. In addition, in figures 3.11a and b, there are several loops (arrowed) which are oriented differently from the other dislocation loops. The angle between these two sets of differently oriented loops is $\sim 53^\circ$, which is again very close to the angle between the $[210]_\alpha$ and $[2\bar{1}0]_\alpha$ directions. Therefore, the loops in figures 3.11a and b are confirmed to be on the $\{210\}_\alpha$ planes.

Although the dislocation loops on the $\{110\}_\alpha$ planes were documented and explained as the result of segment movement of the dislocation helices [12], the loops on $\{210\}_\alpha$ planes have never been reported before. The detailed formation mechanism of these $\{210\}_\alpha$ loops is not clear yet. However, the $\{210\}_\alpha$ loops



(a)



(b)

Figure 3.11 S' sheets parallel to $(210)_\alpha$ loop plane. $[B] = [001]_\alpha$.

shown in figure 3.12 indicate that these loops very likely originated from dislocation helices because they have similar diameters and spacing as the pitches in the dislocation helices. One possibility for the existence of the $\{210\}_\alpha$ loops is that these loops are originally formed on $\{110\}_\alpha$ planes and later rotated to the $\{210\}_\alpha$ planes by prismatic glide. The primary reason for this rotation is that the free energy of the system will be minimized because the habit planes of the S' phase are $\{210\}_\alpha$. When a S' nucleus first forms at a $\{110\}_\alpha$ loop, the nucleus may cause part of the dislocation loop to rotate to the $\{210\}$ plane which is parallel to the broad face of the S' nucleus, as shown in figure 3.13a. This way, the loop will be puckered and the total length of the dislocation loops will increase. To minimize the total length, the entire loop has to rotate to the $\{210\}$ plane. This yields the $\{210\}$ loop morphology (figure 3.13b). It then may be argued that some $\{110\}$ loops were indeed observed in the present study, such as those shown in figure 3.10. It is interesting to notice that the $\{110\}$ loops usually have a larger diameter than the $\{210\}$ loops. Therefore, the possibility of two different variants of S' nuclei forming at a $\{110\}$ loop in a short time period is much larger than at $\{210\}$ loops. As shown in figure 3.13c, if two variants of S' nuclei nucleate at the loop before it rotates, the loops will be pinned and any later rotation will be impossible. In addition, as is known, in Al-Li alloys, the vacancy mobility is lower than in other aluminum alloys, therefore, loops with small diameter are more likely to exist in these alloys. Hence, the $\{210\}$ loops may be a feature unique in Al-Li-Cu-Mg alloys.

Figure 3.14a shows dislocation helices and another type of dislocation loop. In common figure 3.11, the $[010]_\alpha$ and $[100]_\alpha$ directions were determined using S' laths in the same grain as calibration. The analysis of the orientation relationship between the loops and the helices (see Appendix III) indicates that these loops

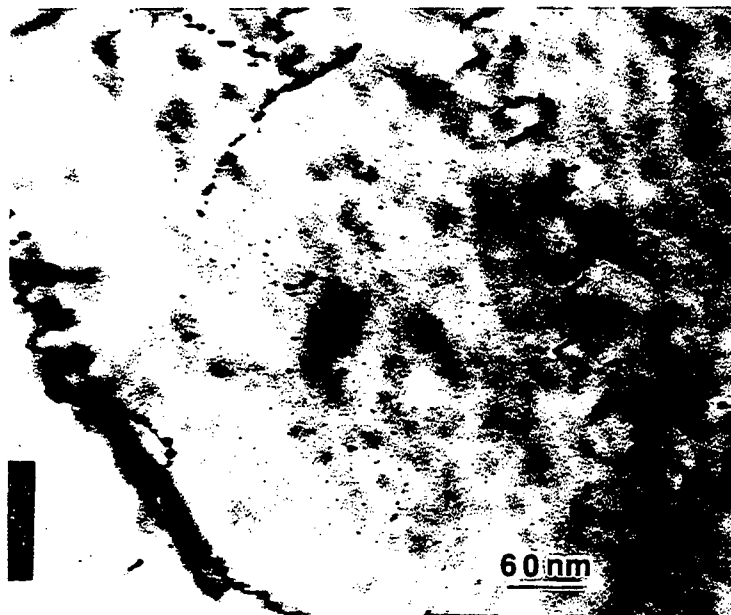
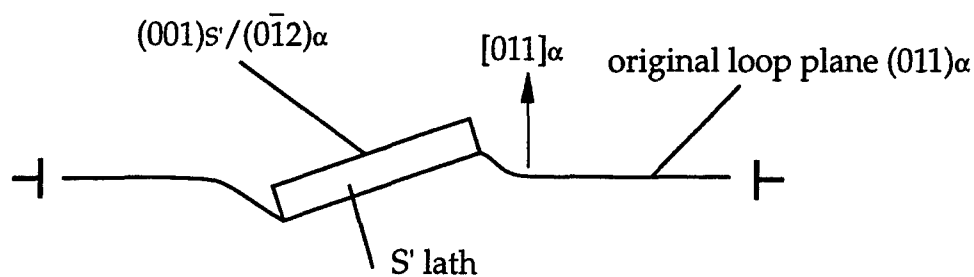
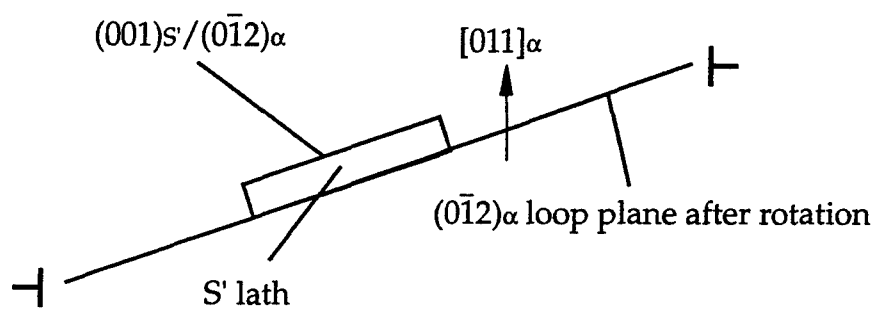


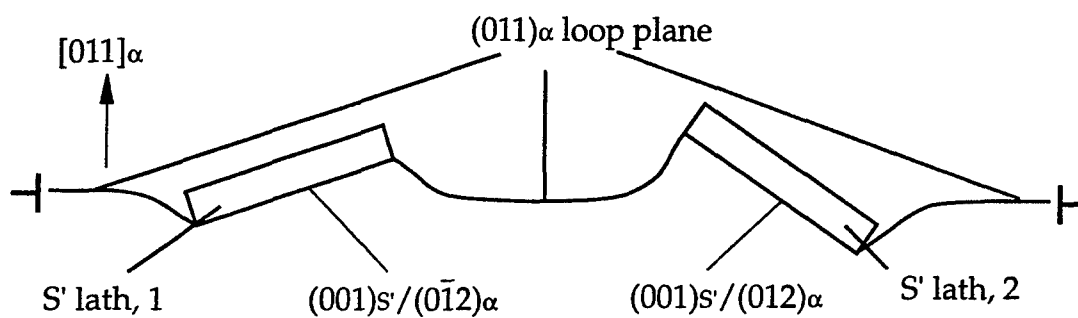
Figure 3.12 Relation of the dislocation loops on (210) planes and dislocation helices.



(a) puckered loop on $(011)_\alpha$ with the nucleation of S' lath

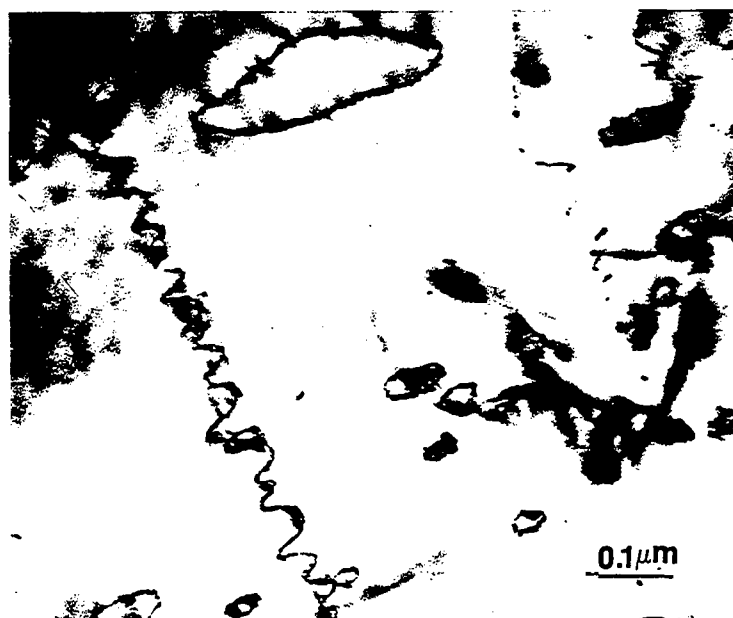


(b) $(012)_\alpha$ loop



(c) $(011)_\alpha$ loop pinned by more than one S' lath

Figure 3.13 Loops on $(011)_\alpha$ and $(012)_\alpha$ planes.



(a) upright view



(b) inclined view

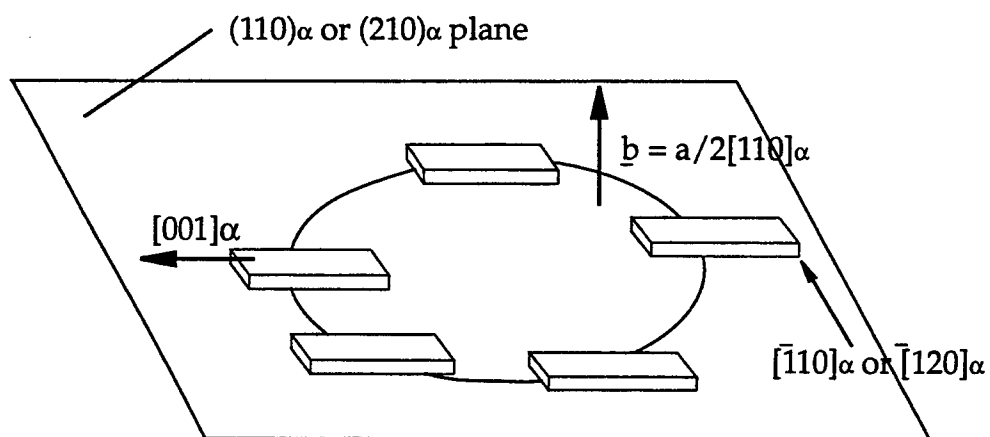
Figure 3.14 S' sheets inclined to dislocation loops.

are not on the $\{110\}_\alpha$ planes. In figure 3.11, because the S' precipitates lie within the loop planes, when these planes are oriented with their normal perpendicular to the beam direction, their orientation can be determined according to their projections. In figures 3.14, because the S' are inclined with respect to the loop planes (this can be seen clearly by comparing figure 3.14a with figure 3.14b, which is tilted away from $[001]_\alpha$), the loop planes in figures 3.14 do not project as rods. The loop planes were not able to be determined. As to the formation mechanism, the morphology of these loops are very similar to the faulted loops described by Kiritani and Weissmann's study [12] or the Lissajous-like figures addressed by Thomas and Whelan [13]. The latter are generated by the interaction of a pair of dislocation helices with opposite helical rotation. In either case, the loops are not on $\{110\}_\alpha$ or $\{210\}_\alpha$ planes.

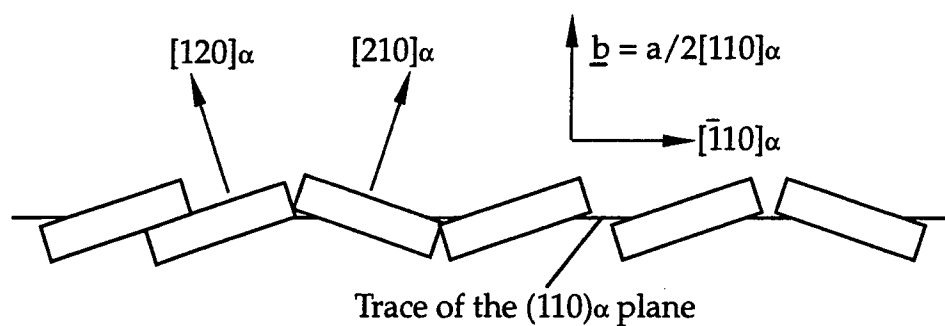
3.3.2.2. Relative Orientation of S' Precipitates with respect to Dislocation Loops

Kiritani and Weissmann's study [12] indicated that the dislocation loops on $\{110\}_\alpha$ planes in aluminum alloys usually had Burgers vector $\vec{b} = \frac{1}{2} [110]_\alpha$ and they were formed from the condensation of quenched-in vacancies. As shown earlier, for dislocation loops with $\vec{b} = \frac{1}{2} [110]_\alpha$, two variants of S' precipitates whose c axes are parallel to $[120]_\alpha$ and $[210]_\alpha$ directions will nucleate on any given $\{110\}_\alpha$ loops. These two S' variants have their a axis parallel to the $[001]_\alpha$ direction (see figures 3.15a and b). The alternate nucleation of these variants of S' precipitates would lead to the S' sheets "parallel" to the loop plane.

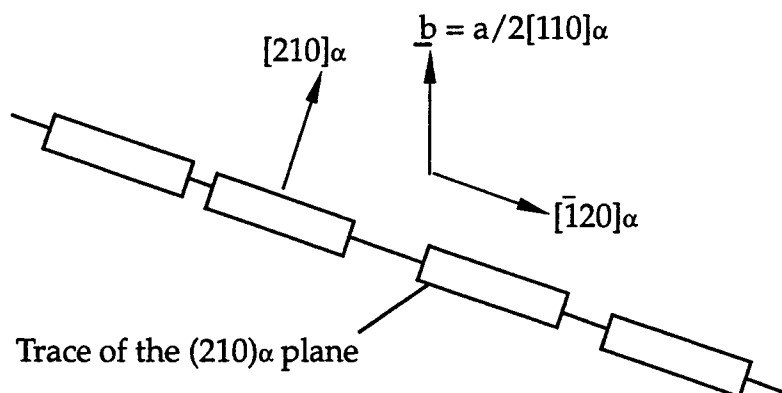
Similarly, as analyzed above, the $\{210\}_\alpha$ loops originated from dislocation helices also have Burgers vector $\vec{b} = \frac{1}{2} \langle 110 \rangle_\alpha$. However, as the habit planes of the S' laths are also $\{210\}_\alpha$ planes, of the two variants, the S' laths whose habit plane is parallel to the loop planes will be preferred, such as shown in figure



(a)



(b)



(c)

Figure 3.15 Model of S' nucleated at dislocation loops on (110) α or (210) α planes.

3.15c, because these laths will destroy a greater area of the loop. This has been proven by TEM examination. Figure 3.16 is a high magnification image of three $(210)_\alpha$ loops. The (001) lattice image of the S' precipitates nucleated at this loop can be resolved. From the orientation of the $(001)S'$ lattice image, it can be seen that all of the S' precipitates belong to the same variant, which has its (001) plane parallel to the $\{210\}$ loop plane. Again, in figure 3.16, the growth ledges of the S' precipitates can be clearly resolved (arrowed).

In the present study, another completely different orientation of S' precipitates with respect to dislocation loops have been found. Instead of forming S' sheets parallel to the dislocation loop planes, the S' precipitates nucleated at these loops orient their a axes at an angle with respect to the loop planes. As shown earlier in figure 3.14, by changing the beam direction, the S' nucleated at dislocations loops are shown to be inclined to the loop planes instead of lying within the planes. Figures 3.17a and b are another pair of micrographs showing a similar situation. Figure 3.17a was recorded with a beam direction closely parallel to $[100]_\alpha$ and the S' precipitates are shown upright. It can be seen that the S' precipitates penetrate the dislocation loop plane. The penetration can be seen more clearly by tilting the sample from the $[100]_\alpha$ beam direction, such as in figure 3.17b. Instead of forming an S' sheet on the loop plane, the S' precipitates form a ring along the loop.

3.4. MULTIPLE S' PRECIPITATION MODES

Three types of S' precipitates (type A, B and C) have been defined in section 2.3.2.3 according to their origin which will now be discussed.

Precipitates type A are the S' laths preferentially nucleated at dislocations and have been discussed thoroughly in the above. Type B precipitates are laths

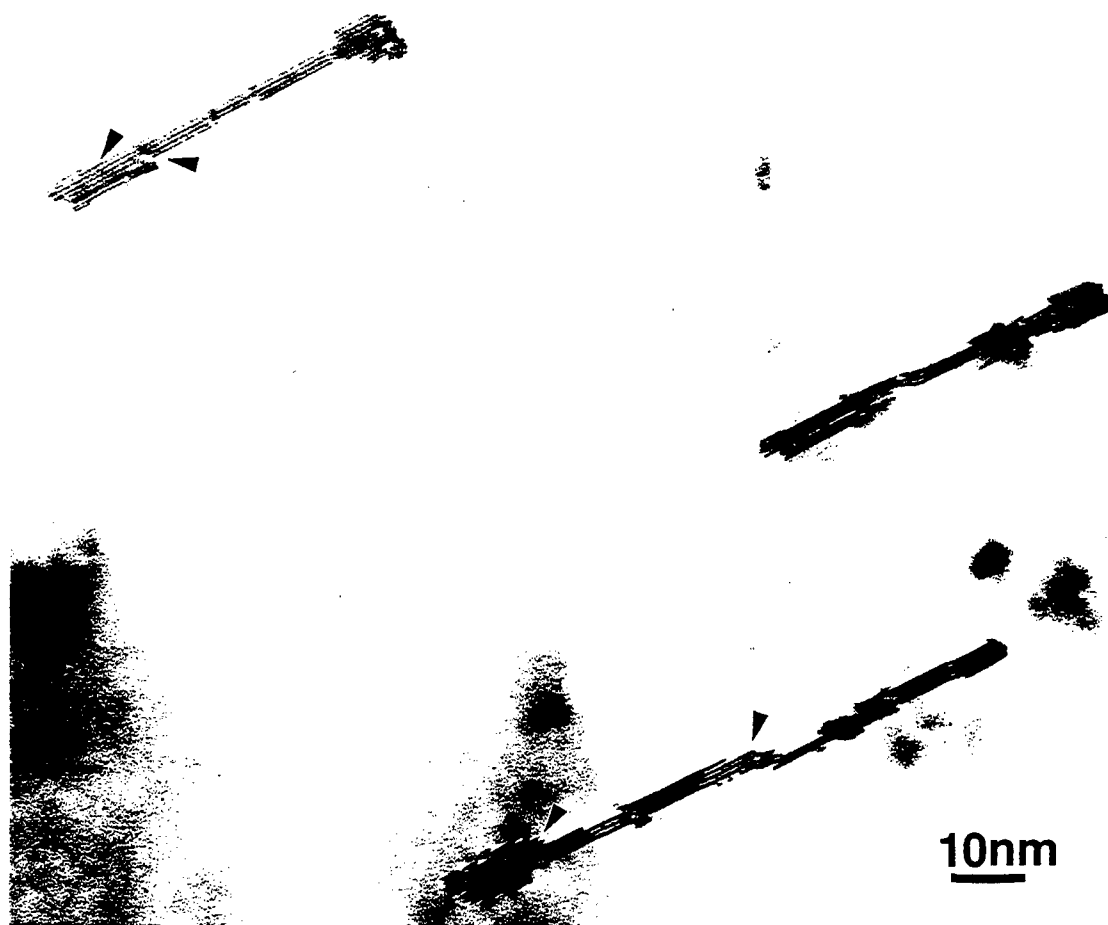
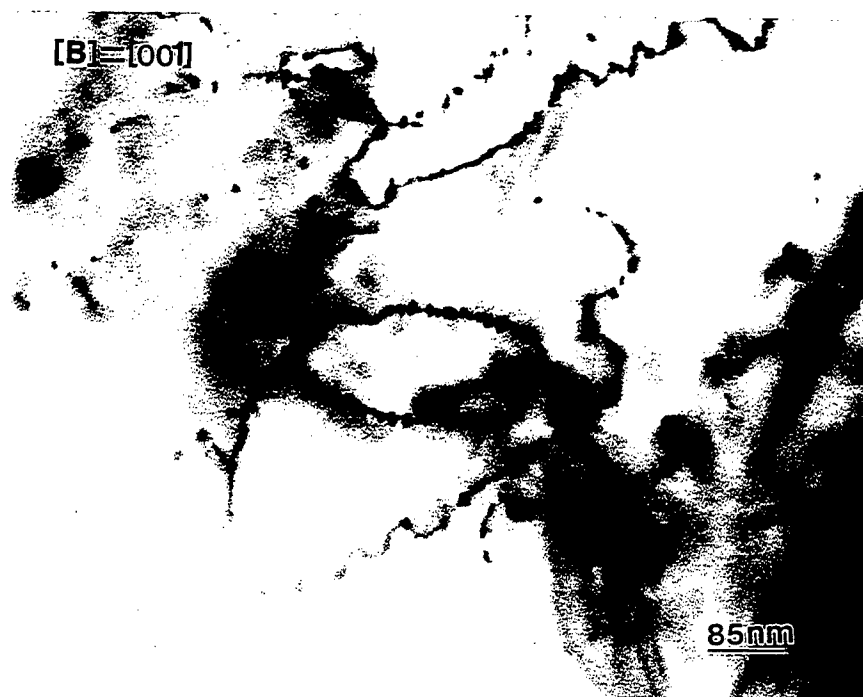
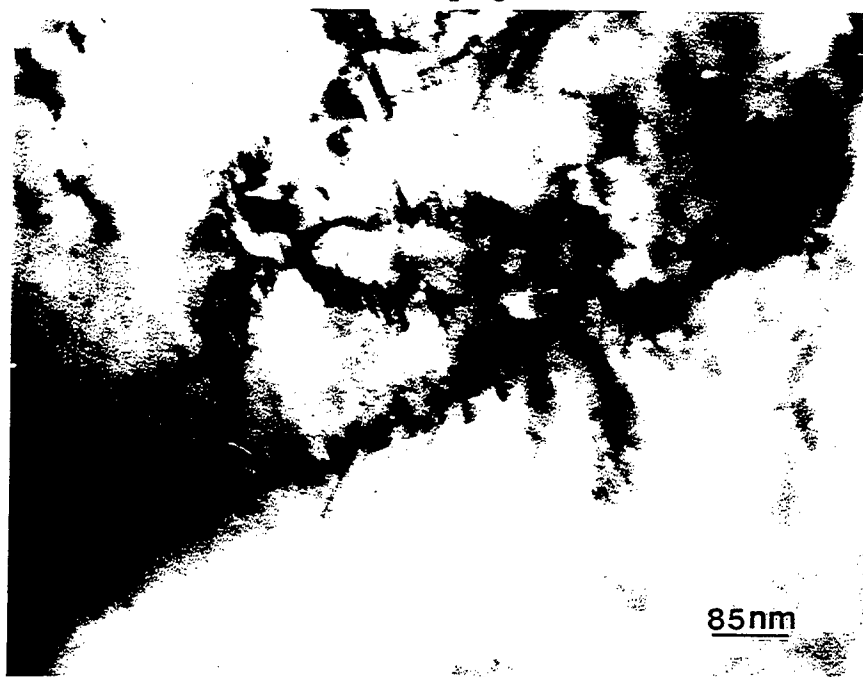


Figure 3.16 Single variant of S' precipitates formed at $\{210\}_{\alpha}$ loops. The broad interfaces of these precipitates are parallel to the loop plane



(a) upright



(b) inclined

Figure 3.17 S' precipitates at a dislocation loop viewed at different orientations by tilting the sample.

which appear to form independently of dislocations (arrowed in figure 3.18). Because these S' laths have the same size as those nucleated at dislocations, it is very likely that the type B laths are formed at the same aging stage as type A precipitates. From the discrete distribution of precipitates type B, the defects for their nucleation could be vacancy clutters.

It is well known that in as-quenched Al-Li alloys, the mobility of vacancies is very low due to the strong affiliation between Li atoms and vacancies. Therefore, it is generally very difficult for vacancies to migrate and form clusters. The lack of dislocation helices and loops in Al-Li alloys is considered as the proof of the immobility of vacancies. In the present study, TEM examination, figure 3.19, indicates that in the as-quenched 8090 alloy, except for dislocation loops around β' (Al_3Zr) particles, there is no evidence for vacancy migration and condensation. However, after natural aging for about 6 months, dislocation helices and loops can be seen within the α matrix, figure 3.20. The studies of Kiritani and Weissmann [12] and Thomas and Whelan [13] indicated that the dislocation helices in aluminum alloys were the results of vacancy condensation at screw dislocations. Hence, the vacancy migration in the 8090 alloy used for the present study is not negligible after natural aging. This vacancy migration led to the formation of dislocation loops, helices, and most probably vacancy clusters.

Because the samples used for the microstructural examination discussed were all naturally aged for 6 months prior to the artificial aging at 190°C , it is reasonable to assume that type B precipitates are nucleated at vacancy clusters. In addition, it has also been found that, in an 8090 sample aged for 16 hours immediately after the solution treatment, type B precipitates were hardly found. On the other hand, large amounts of type B precipitates can be seen in a sample

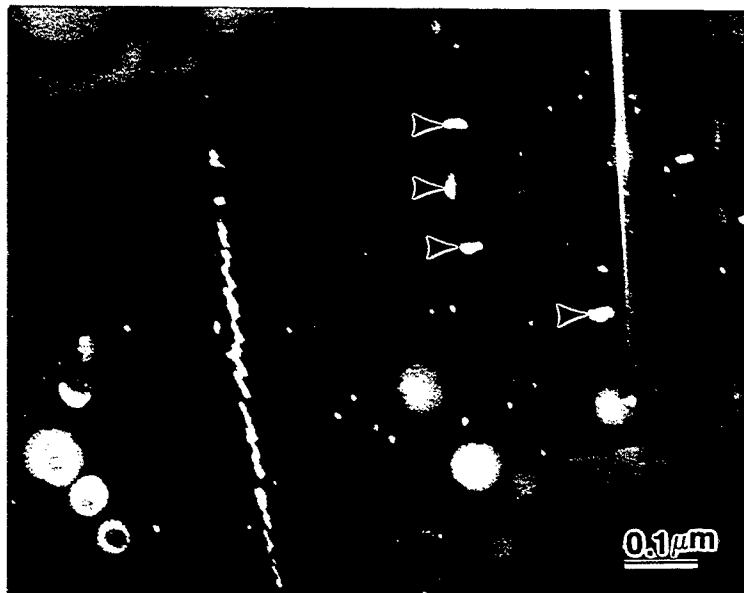


Figure 3.18 Upright view of S' precipitates of type B (arrowed).



Figure 3.19 Microstructure of a as-quenched 8090 sample. Except for the dislocation loops around the particles, there are no other dislocation loops and helices



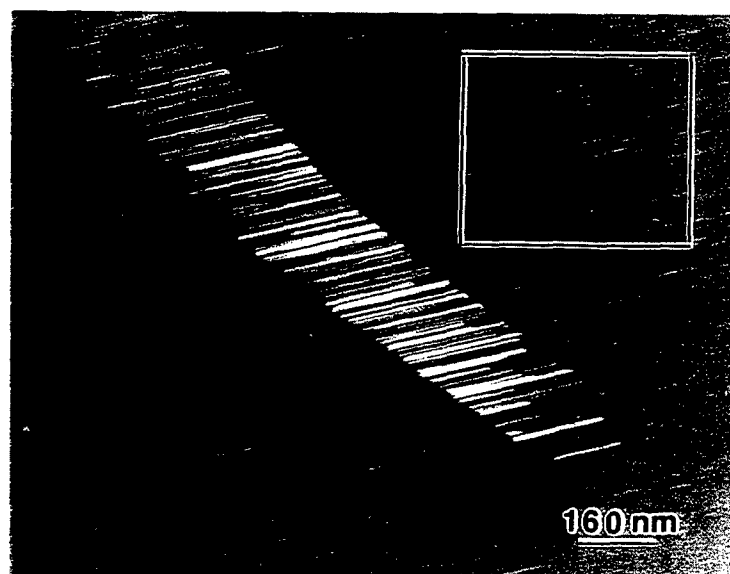
Figure 3.20 Dislocations in a 8090 sample naturally aged for 6 months. The dislocation helices (H) and loops (L) are from the vacancy condensation.

experienced 6 month room temperature aging and then artificially aged for 16 hours at 190°C, such as in those in figure 2.9 and 2.11.

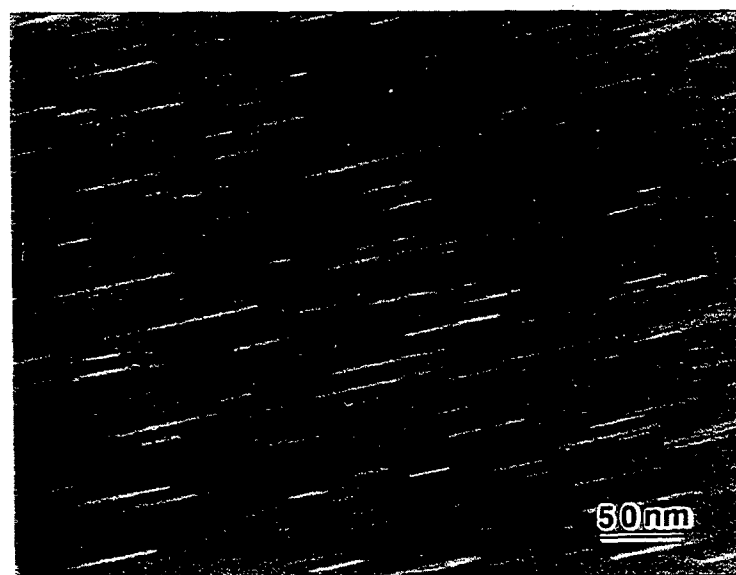
S' precipitate sheets and laths are well documented in Al-Cu-Mg alloys by many studies [4, 7-10, 14, 15], although they have never been designated differently. On the other hand, S' precipitate type C which was shown earlier in figure 2.11 and here in figure 3.21 were only reported in limited cases [4, 9]. In figure 3.21, a sample aged for 48 hours at 190°C, in addition to the S' precipitates nucleated at a dislocation, the background of this photograph is decorated with uniformly distributed S' precipitates. These uniformly distributed precipitates have their longitudinal axis parallel to the a axis of those type A S'.

Gregson et al [4, 9] observed the similar uniformly nucleated S' precipitates within the matrix in several Al-Li-Cu-Mg alloys. They suggested that as the δ' precipitation continues in these alloys, the vacancies which had been strongly bound to Li were rejected into the matrix. These vacancies tend to form clusters and condense into loops or helices. With sufficient Cu and Mg supersaturation, these aggregated vacancies would cause widespread S' precipitation. In their article, the source for a high Cu and Mg supersaturation was not clear.

Radmilovic et al's finding [10] explained the uniform distribution of the S' precipitates successfully. By using high resolution electron microscopy, Radmilovic et al. [10] observed S' nucleation at δ'/α interfaces. They suggested that although the δ'/α interfaces are not very favorable sites for S' nucleation because of the very low interfacial energy, the area next to δ'/α interfaces is expected to be highly supersaturated with Cu and Mg because these two elements are rejected into the matrix as δ' precipitates grow. Considering Gregson et al.'s theory mentioned above, a high concentration of vacancies should also be found near δ'/α interfaces. Hence, although the low energy δ'/α



(a)



(b)

Figure 3.21 S' precipitates of type A and type C after 48 hour aging at 190°C.
(b) is an enlarged image showing type C the framed area in (a)

interfaces do not provide efficient heterogeneous nucleation sites for S' precipitation, the high level of Cu, Mg and vacancies near these interfaces provide the preferential nucleation environment for the S' phase. By nature, these uniformly distributed S' precipitates are heterogeneously nucleated. However, because of the homogeneous nucleation of δ' precipitates, these preferential S' nucleation sites are distributed very uniformly in the α matrix and the S' nucleated in this mechanism are distributed uniformly in the matrix, as shown in figure 3.21b. As the nucleation of these S' relies on the high concentration of vacancies in the matrix and the high concentration of vacancies near δ'/α interfaces is the result of δ' precipitate coarsening, type C S' precipitates are usually formed at a later stage as compared with the type A and type B precipitation. Therefore, the type C precipitates in figure 3.21 have a smaller size and weaker intensity.

Figure 3.22 documents an interesting phenomenon of the S' precipitation. In the center of this photograph, there is a dislocation helix where many type A S' precipitates have nucleated. In the background, numerous finely dispersed S' precipitates (type C) can also be seen. Because the beam direction of this TEM CDF image is near $[100]\alpha$, the S' precipitates are viewed upright as small rods. (This orientation is preferred for S' precipitate distribution evaluation because the interference from the S' precipitates at different depth of the sample is significantly reduced). In the vicinity of the dislocation helices, there is a type C S' precipitate free region. Because the dislocations are an annihilation sink for the vacancies, it is very likely that the vacancies in the vicinity of the dislocation have migrated to the dislocation and have annihilated. Therefore, the heterogeneous nucleation sites near the dislocation are destroyed and type C precipitation is



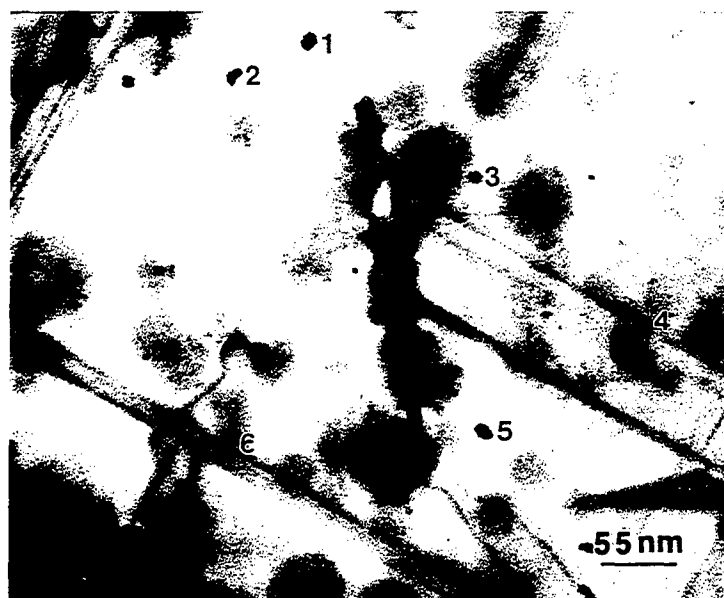
Figure 3.22 S' precipitates of type A nucleated at a dislocation helix and type C in the background. For precipitates of type C, there is a precipitate free zone in the vicinity of the helix.

suppressed. This is also very likely the reason for the S' PFZ shown earlier in figures 2.25 and 3.9. In addition, the high density of S' precipitates on the dislocation will also have caused the depletion of Cu and Mg in this region, hence, no more other S' precipitates can be formed in this region.

In both the experimental results reported in Gregson et al's article [4] and in this thesis study, with a $[100]_{\alpha}$ beam direction, some small dark regions have been observed, such as those shown in figure 3.23a (numbered). Since the size of these regions is very small, usually in the range of a few nm, Gregson et al suggested that they were vacancy clusters. When the field imaged in figure 3.23a was examined after the sample is tilted, the discrete regions are now imaged as rods as shown in figure 3.23b. Hence, it can be concluded that the small dark regions in figure 3.23a are not vacancy clusters. They are S' rods viewed upright, which could be either type B or type C.

3.5. CONCLUSIONS

1. The S'/ α interfaces can achieve a high coherency at $(001)_S \parallel (0\bar{1}2)_{\alpha}$ planes and a lower coherency at $(010)_S \parallel (021)_{\alpha}$ planes. On the other hand, $(100)_S \parallel (100)_{\alpha}$ planes are probably incoherent.
2. The geometric shape of the S' phase is lath-like although rod-like S' precipitates could be observed due to the impingement between precipitates or due to differences in ledge supply.
3. The S' precipitates in Al-Li-Cu-Mg alloys can be classified into three types according to their heterogeneous nucleation sites: dislocations, vacancy clusters and δ'/α interfaces, respectively.
4. Of the 12 variants of S' precipitates, usually only one or two can nucleate at the same dislocation.



(a) $[B] = [100]_{\alpha}$



(b) tilted from $[B] = [100]_{\alpha}$

Figure 3.23 Small dark regions in (a) are shown to be precipitate laths/rods in (b).

5. Vacancy rearrangement can occur in Al-Li alloys after long time natural aging. This leads to the existence of dislocation helices and loops as well vacancy clusters in these alloys.
6. In Al-Li-Cu-Mg alloys, {210} loops could be a preferred configuration for dislocation loops which originated from dislocation helices.
7. When nucleated at dislocation loops, the S' can form not only sheets parallel to the loop planes, but also rings with S' laths inclined to the loops.

3.6. REFERENCES

1. P. J. Gregson and H. M. Flower: *Acta metall.*, 33, (1985), p527.
2. W. S. Miller, M. P. Thomas, D. J. Lloyd and D. Creber: *Mater. Sci. Tech.*, 2, (1986), p1210.
3. C. P. Blankenship Jr.: *PhD dissertation*, University of Virginia, (1992).
4. P. J. Gregson, K. Sinsdale, S. J. Harris, and B. Noble: *Mater. Sci. Tech.*, (1987), p7.
5. Yu. A. Bagaryatskii: *Zhm. Tekhn. Eiziki Fulmer Res. Inst. Trans.* Nos. 11, 12, 55, 66, (1948).
6. J. M. Silcock: *J. Inst. Metals*, 89, (1961), p203.
7. R. N. Wilson and P. G. Partridge: *Acta metall.*, 13, (1965), p1321
8. G. C. Weatherly and R. B. Nicholson: *Phi. Mag.*, 17, (1968), p801.
9. P. J. Gregson, H. M. Flower, C. N. Tite, and A. K. Mukhopadhyay: *Mater. Sci. Tech.*, 2, (1986), p349.
10. V. Radmilovic, G. Thomas, G. J. Shiflet, and E. A. Stark, Jr.: *Scripta Metall.*, 23, (1989), p1141.
11. J. Yan: *J. Mater. Sci. Letters*, 10, (1991), p591.
12. M. Kiritani and S. Weissmann: *J. Appl. Phys.*, 42, (1971), p2603.

13. G. Thomas and M. J. Whelan: *Phil. Mag.*, 4, (1959), p511.
14. X. Xia and J. W. Martin: *Mater. Sci. Eng.*, A128, (1990), p113.
15. X. Xia: *Scripta Metall.*, 26, (1992), p1587.

CHAPTER 4

AGING RESPONSE OF A PARTICULATE REINFORCED METAL MATRIX COMPOSITE

4.1. BACKGROUND

Metal matrix composites (MMCs) represent a relatively new and important class of materials. Aluminum alloys, because of their high strength, low density and reasonable cost, are good matrix candidates for MMCs used in a wide range of engineering applications where high performance and weight saving are desired, such as, aerospace (module doors of aircraft [1]) and automobile (cylinder liners in Honda Prelude and diesel-engine pistons in Toyota [2]) industries.

Unlike continuous filament reinforced composites, the properties of whisker or particulate reinforced composites are largely dependent on the matrix. So far, the matrix choices for aluminum matrix composites have been age hardenable alloys, such as 2024, 6061, 8090 etc. For these materials, matrix strengthening by an aging process plays an important role in developing high strength. For example, Arsenault found that adding 20% SiC to annealed 6061 increase the yield strength by 100MPa [3]. However, heat treating unreinforced 6061 from the annealed condition to T6 increases the yield strength by 220 MPa [4]. Hence, most aluminum matrix composites are expected to be age hardened to develop maximum strength.

Although at normal aging temperatures, the microstructure and properties of the reinforcement usually do not experience any changes, the

aging behavior of a MMC can not be simply determined by the aging behavior of the unreinforced matrix alloy. In metal matrix composites, a high density of dislocations in the matrix is a common feature. Due to the usually very different coefficients of thermal expansion (CTEs) between matrix and reinforcement, differential contraction is expected in these materials during the cooling cycles. In metal matrix composites, this differential contraction is predominantly accommodated by the plastic deformation of the matrix because the reinforcement usually has a much higher modulus than the matrix. An *in situ* high voltage electron microscopy (HVEM) study conducted by Vogelsang et al [5] revealed the generation of these dislocations during cooling cycles. During aging, these dislocations can provide preferential nucleation sites and solute diffusion short circuits and hence promote the formation of strengthening phases. This is the principal reason for accelerated aging kinetics in many metal matrix composites [6-10]. These dislocations can also work harden the matrix and further increase the strength of the matrix [11]. On the other hand, these dislocations can also provide annihilation sites for vacancies, cause vacancy depletion and exaggerate solute segregation to grain boundaries and reinforcement/matrix interfaces. Hence, precipitation processes during aging could be retarded or suppressed [12, 13]. Consequently, the hardening potential of the composites would decrease [8, 13] or the aging kinetics would be decelerated [12] as compared to the corresponding unreinforced alloys. In addition, Chawla et al [6] reported that since the strengthening phases formed at different temperature ranges could be different in the same material, the aging response could also be different. In their study on a 2014/SiC composite, the aging response of the material did not exhibit any acceleration when aged at

150°C. However, at 195°C, the peak aging time decreased from 8 hours in the unreinforced alloy to 2 hours in the composite. Chawla et al [6] indicated that at 150°C, the strengthening of the material depended on the formation of GP zones which were not affected significantly by the dislocation density in the matrix. When aged at higher temperature, S' precipitates became the predominant strengthening phase. Since S' is known to preferentially nucleate at dislocations, its formation would be accelerated by a high density of dislocations.

Interfaces between the matrix and the reinforcement in a composite represent another important factor in determining the properties of the composite. A clean interface and good interfacial bond are necessary requirements for effective load transfer and prevention of premature fracture. Special surface treatments along with proper processing techniques are usually applied to the reinforcement in order to minimize the reaction zone at interfaces and to improve the bonding between reinforcement and the matrix alloy. For most practical aluminum/SiC composites and for processing methods used in industry today, the reaction between aluminum and SiC is virtually suppressed. The reaction zone at aluminum/SiC interfaces is actually not a problem for the properties of these composites. Instead, the precipitation which could occur at the interfaces during aging is more important in affecting the mechanical properties of the composite.

As shown by both previous research [14-16] and in the present study, T_2 (Al_6CuLi_3) precipitates form at high angle grain boundaries and cause δ' PFZs. In aluminum-lithium composites, matrix/reinforcement interfaces may also act as preferential nucleation sites for T_2 . Because of the brittleness of the T_2 phase and the poor strength in the δ' PFZs, not only would the load

transferring efficiency from the matrix to the reinforcement decrease, but also premature failure at the interfaces could occur. As the result, the properties of the composites would be degraded. So far, although the precipitation of the T_2 phase and the associated δ' PFZs at high angle grain boundaries in aluminum-lithium alloys are well documented, the precipitation at and near matrix/reinforcement interfaces in aluminum-lithium composites is not yet well understood.

Hence, the aging response of metal matrix composites is a multi-parameter determined process. The objective of this chapter is provide a fundamental understanding of the effects of these parameters, such as microstructural inhomogeneity and different strengthening phases, on the aging response of a metal matrix composite.

4.2. AGING KINETICS OF THE COMPOSITE

4.2.1. Experimental

The composite used in the present study is an 8090/SiC spray formed material. The composite contains about 17 %vol. SiC particles. The length of these SiC particles ranges from 3 to 10 μm with geometric aspect ratio of 1 ~ 3. Figure 4.1 is a SEM micrograph showing SiC particles and their distribution in the composite. Spray forming is a newly developed technology which has the potential advantage of reducing both the reinforcement/matrix reaction and the inhomogeneity of reinforcement distribution.

The heat treatment of the composite is identical to that used for the unreinforced 8090 alloy (henceforth called the control alloy) in Chapter 2, which includes solution treating at 536°C for 45 minute, naturally aged for ~ 6 months and then artificially aging at 190°C for up to 30 hours.



Figure 4.1 SEM image of the 8090/SiC composite.

In order to monitor the property changes during aging, the hardness of the composite was tested. Both microhardness and macrohardness values have been measured. Microhardness tests were used to assure that any property changes came solely from the matrix. To avoid the interference from SiC particles, microhardness readings were taken from the matrix regions which appeared to be SiC free under the light microscope. For the same reason, a load of 10 gram was employed to obtain hardness indentations as small as possible. Macrohardness tests were also conducted as a complementary method.

To study the effects of a high density of dislocations on the aging response of the 8090 alloy, the microhardness values of a series pre-deformed samples were also measured. These samples were deformed by ~3% before the age hardening process. A set of non-deformed 8090 alloy samples were heat treated together with the pre-deformed samples to make a comparative study. In contrast to the treatment employed for the control alloy and the composite, neither the pre-deformed nor the non-deformed samples were naturally aged.

4.2.2. Results

The micro and macro hardness test results from the composite after different aging times are presented in figures 4.2 and figure 4.3, respectively. To compare the aging kinetics of the composite with the control alloy, the hardness results from the control alloy are also presented in these two figures. Somewhat unexpectedly, the aging kinetics of the matrix in the composite were not significantly affected by the presence of SiC particles. In figure 4.2, the same two stage strengthening observed earlier in the control alloy is also exhibited in the composite. The positions of the two strengthening peaks are

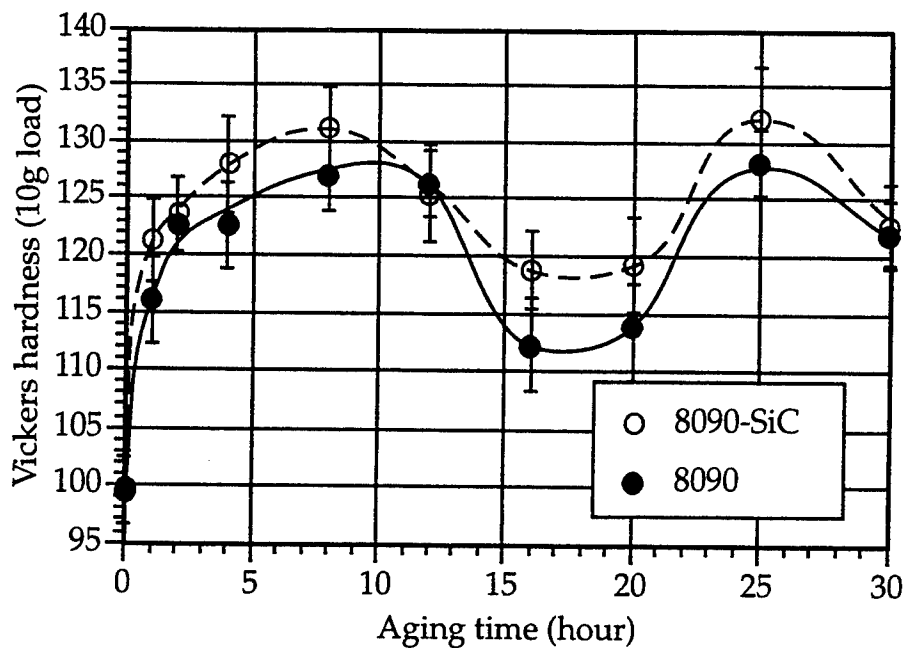


Figure 4.2 Aging kinetics (represented by microhardness changes) of the matrix for both the composite and the control alloy.

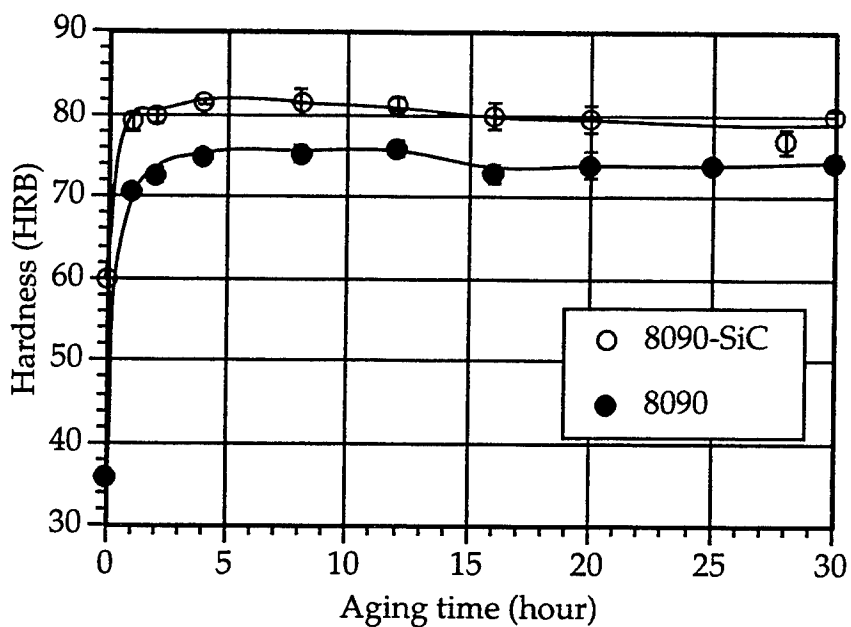


Figure 4.3 Macrohardness changes upon aging at 190°C for the composite and the control alloy.

at almost the same aging times as in the control alloy. Moreover, the strengthening levels achieved in the two materials are very close.

Figure 4.3 indicates that in common with the control alloy, the composite exhibits good aging stability up to 30 hours when it is characterized by macrohardness changes. In addition, due to the existence of SiC particles, the HRB values are higher in the composite.

Although the non-deformed 8090 samples still exhibits two stage hardening, figure 4.4, the second aging peak has disappeared in the pre-deformed samples. In addition, the first aging peak in the pre-deformed 8090 alloy is higher than in the non-deformed alloy. The second aging peak in the non-deformed 8090 alloy is not as pronounced as the first peak, which is in contrast to the situation in figure 4.2. The as-quenched sample also has a much lower hardness than the sample which has been naturally aged prior to the artificial aging (figure 4.2).

4.3. DISLOCATION CHARACTERISTICS OF THE COMPOSITE

The aging kinetics of metal matrix composites are closely related to the microstructure in the matrices of these materials, such as, dislocations and interfaces. To understand the aging kinetics shown in figures 4.2 and 4.3 in this particulate reinforced composite, the dislocations in the matrix of the composite have been examined and compared with those in the control alloy.

4.3.1. Experimental

As in the control alloy, TEM was the principal method for microstructural examination in the composite. The electropolishing method used to prepare TEM samples of the control alloy proved to be unsuitable for

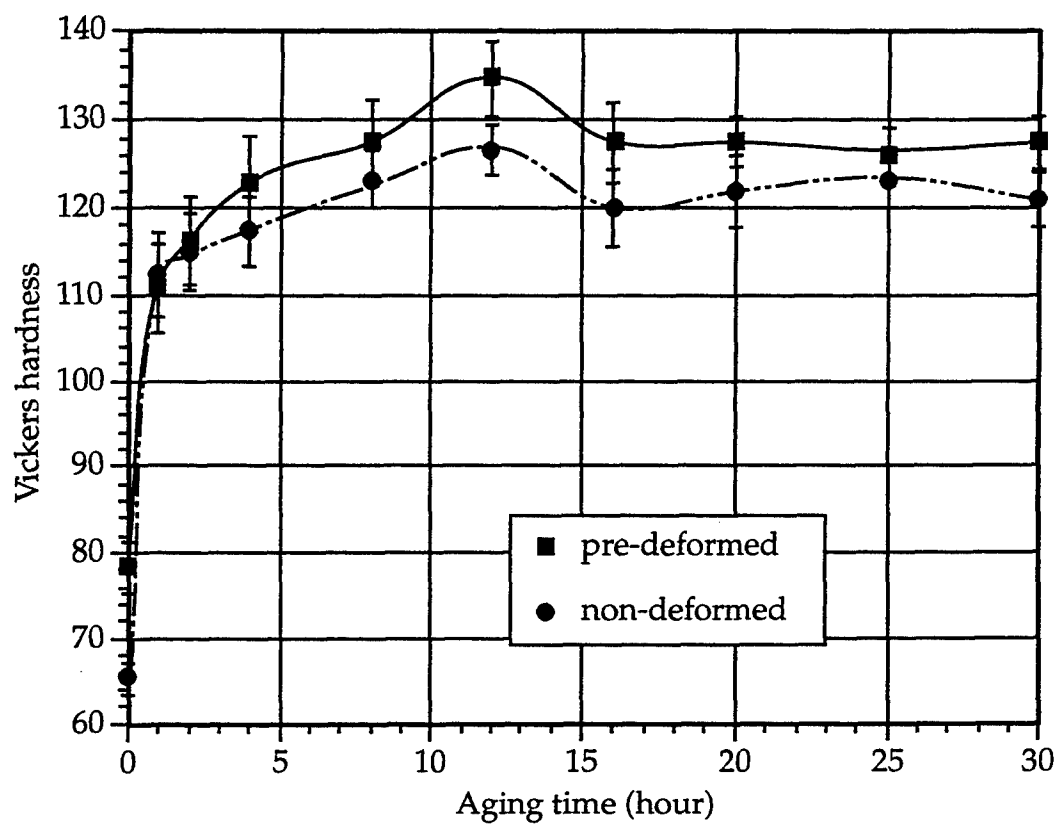


Figure 4.4 Comparison of hardness change of the pre-deformed 8090 material with the non-deformed material.

the composite sample preparation, because of the very different electrochemical properties of SiC and the aluminum matrix. Hence, after the thickness of the composite specimen was reduced to $\sim 100 \mu\text{m}$ by mechanical grinding, 3 mm diameter sample discs were further dimpled to a thickness of $\sim 20 \mu\text{m}$. Subsequently, the samples were transferred to a Gatan 600 ion mill machine for the final thinning process until perforation was obtained. The ion milling was conducted under a working voltage of 3.5 kV and a current of 0.5 mA for each gun. To reduce the differential thinning rate between SiC particles and the matrix, in the final thinning stage, the milling angle was reduced to $\sim 10^\circ$. In addition, a cold stage cooled with liquid nitrogen was used to prevent possible heating effects during ion milling. The sample materials used for dislocation examination were aged at 190°C for 1 hour to prevent further natural aging during sample preparation and examination.

Dislocation density measurements were conducted on weak beam (WB) dark field images in both the control alloy and the composite with bright field (BF) imaging technique as the complementary method for the general dislocation distribution observation. An intersection method [17] was employed to measure the dislocation density in both materials. By counting the number (N) of the intersections of dislocations with randomly drawn lines in a sample with a thickness (t), the dislocation density (Λ ($1/\text{m}^2$)) can be obtained from the following equation [17]:

$$\Lambda = \frac{2N}{Lt} \quad (4.1)$$

where L is the total length of those randomly drawn lines. In this study, the lines were a series of concentric circles which were designed to reduce the possible errors caused by the anisotropic distribution of dislocations. The

thickness, t , of each sample was determined from the thickness fringes at grain boundaries under strict two beam conditions.

4.3.2. Results

4.3.2.1 Dislocation Distribution

Figure 4.5 is a BF TEM micrograph which illustrates the dislocation distribution in a matrix area between two SiC particles. The most noticeable feature of this micrograph is the non-uniform dislocation distribution in the matrix. In the vicinities of the two SiC particles, the dislocation density is so high that the individual dislocations are hardly distinguishable. In the area which is further away from the two SiC particles, the dislocation density is much lower and individual dislocations are clearly imaged.

Details of the dislocations in the vicinity of a SiC particle are illustrated clearly in figure 4.6, a high magnification WB image. This micrograph shows that the matrix adjacent to the SiC particle is most highly dislocated so that the dislocations are tangled and it is very difficult to distinguish individual dislocations. As the distance from the matrix/SiC increases, the dislocation density decreases gradually and individual dislocations eventually become resolvable. In addition to the dislocation density, the configurations of dislocations in different regions are also different. In the highly dislocated region, most of the dislocation lines are bowed. In contrast, the dislocations in low dislocation density regions are mostly helices and loops. This feature can be seen both in figure 4.5 and in figure 4.7 which is a high magnification WB image from a SiC free region in the composite.

The dislocations in the control alloy were also examined using WB and are shown in figures 4.8a and b. In addition to the relatively low dislocation



Figure 4.5 Dislocation distribution in the matrix of the composite between two SiC Particles.

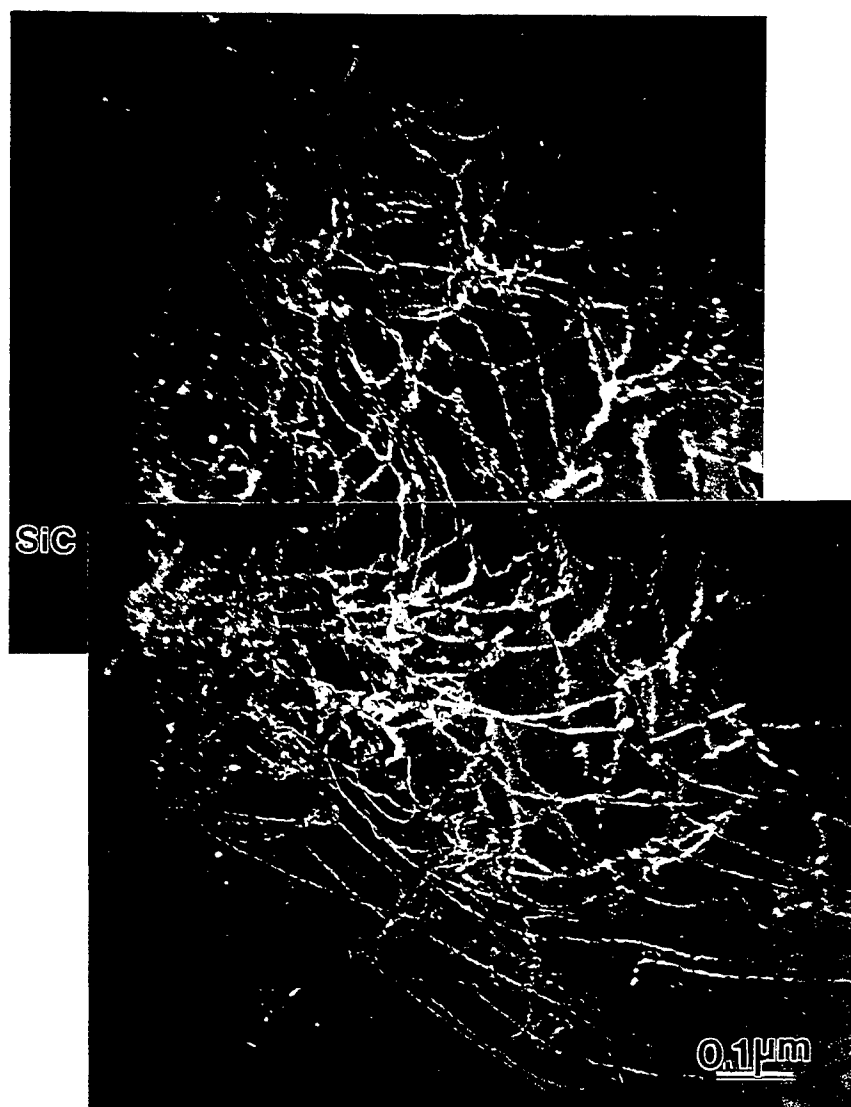


Figure 4.6 High magnification WB image of dislocations in the vicinity of a SiC particle.

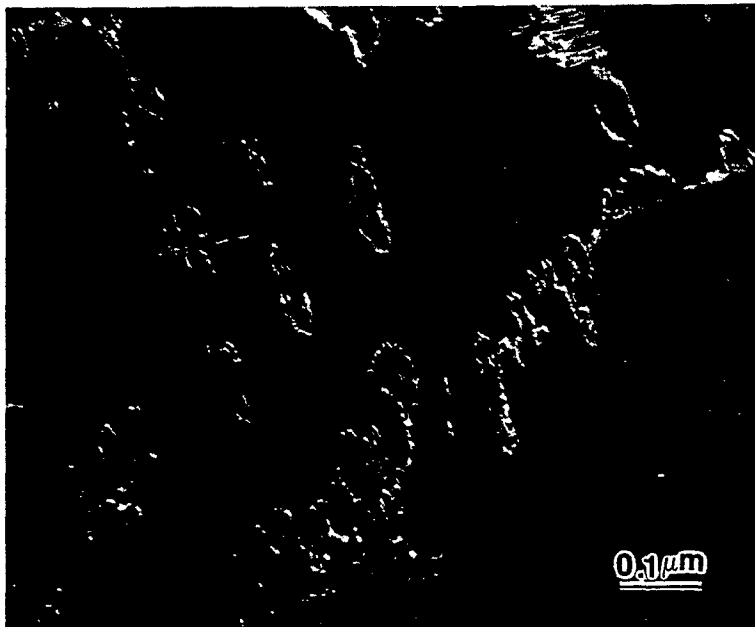
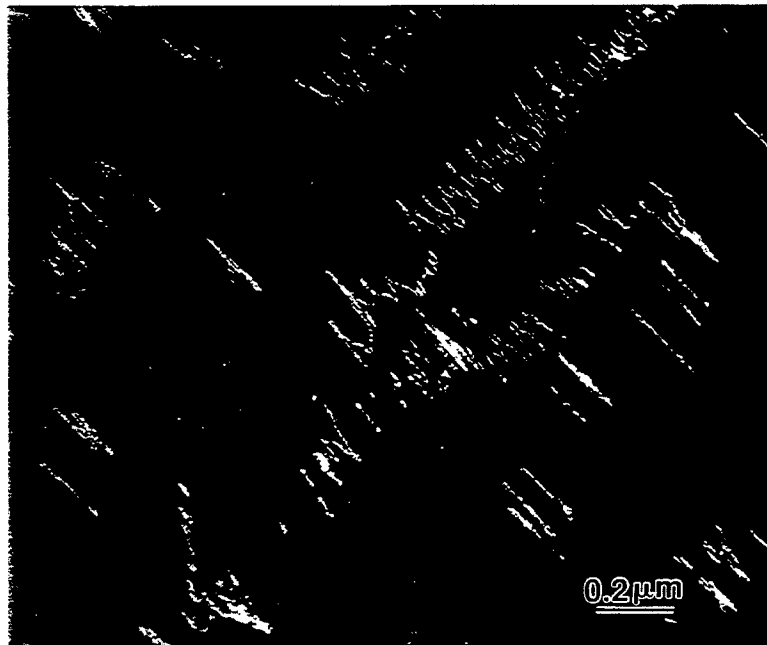
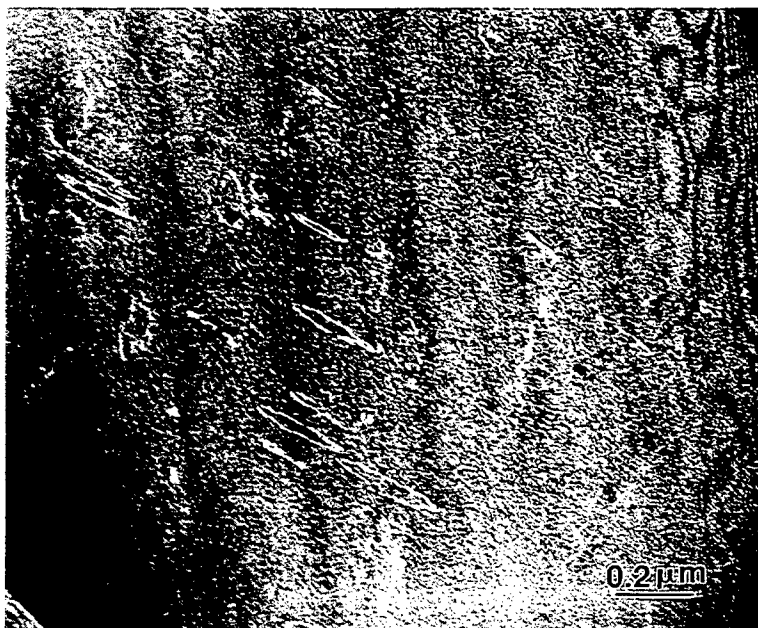


Figure 4.7 Dislocations in a SiC free region of the composite.



(a)



(b)

Figure 4.8 Dislocations in the control alloy:
(a) dislocation helices,
(b) dislocation loops.

density, most of the dislocations in the control alloy are helices and loops, which are very similar to those in the SiC free regions of the composite.

4.3.2.2. Dislocation Density Measurement

Dislocation densities in both the control alloy and the composite have been quantitatively measured using the intersection method [17] and calculated using equation 4.1. The average dislocation density of each set of samples came from measurements on at least 6 micrographs. The results are presented in table 4.1.

Table 4.1 Dislocation Densities

Composite		Control Alloy
Vicinities of SiC	SiC free regions	
$1.65 \times 10^{14} \text{ (m}^{-2}\text{)}$	$3.68 \times 10^{13} \text{ (m}^{-2}\text{)}$	$4.22 \times 10^{13} \text{ (m}^{-2}\text{)}$

Special attention was paid to avoid very thin areas during the measurements because of the potential for dislocation loss. Most of the dislocation density data came from areas with foil thicknesses of 2500~3500 Å. It should also be pointed out that these results in table 4.1 have already been corrected for the invisibility factor, $\vec{g} \cdot \vec{b} = 0$, which indicates that when the imaging vector \vec{g} is perpendicular to the Burgers vector of a dislocation, \vec{b} , the dislocation will be invisible.

The quantitative results in table 4.1 indicate that the dislocation density in the SiC free regions of the composite is dramatically lower than that in the vicinities of SiC particles. In contrast, the dislocation density in the control alloy is very close to that in the SiC free regions of the composite. These results, together with the dislocation configuration shown in figures 4.5 - 4.8,

demonstrate that the effect of SiC particles on the microstructure of the matrix of the composite is limited in spatial extent.

4.4. PRECIPITATION CHARACTERISTICS OF THE COMPOSITE

After the dislocations in the different regions of the composite and in the control alloy had been compared, the precipitation of the two strengthening phases, δ' and S' , was examined to study the effects of dislocations on these phases. In addition, samples which had been pre-deformed immediately after the solution treatment and before aging were used to verify if the changes in precipitation behavior are indeed associated with the dislocation distribution.

4.4.1. Precipitation of the δ' Phase

Previous studies [7] suggested that in composites, due to the vacancy annihilation at reinforcement/matrix interfaces and dislocations, the coarsening of the δ' phase could be retarded as compared to the unreinforced materials.

Because vacancies in the vicinities of SiC particles may annihilate both at SiC/matrix interfaces and at dislocations, if vacancy annihilation has any effect on the coarsening of the δ' phase, this effect will be more significant in the vicinities of SiC particles. Hence, the sizes of the δ' precipitates in these two regions were measured separately after several aging times. Because no significant size difference between the two regions were found in samples aged for 1, 2, 8 and 25 hours (table 4.2), measurements at other times were no longer carried out separately. The results are present in table 4.2.

The δ' size vs. aging time relationship is presented together with the δ' size in the control alloy in figure 4.9. The data of 1, 4, 8 and 25 hours in this

Table 4.2 δ' Precipitate Size Development

Aging Time & Examined Area	Size \bar{d} (nm)	Standard Deviation (nm)
1 hour, SiC free	15.2	1.58
1 hour, near SiC	16.4	1.60
2 hours, SiC free	18.5	2.06
2 hours, near SiC	18.3	2.10
4 hours	20.6	2.50
8 hours, SiC free	23.2	3.22
8 hours, near SiC	23.7	3.55
12 hours	27.2	2.75
16 hours	30.6	5.80
20 hours	31.8	4.12
25 hours, SiC free	32.6	3.80
25 hours, near SiC	32.3	4.35
30 hours	30.7	3.55

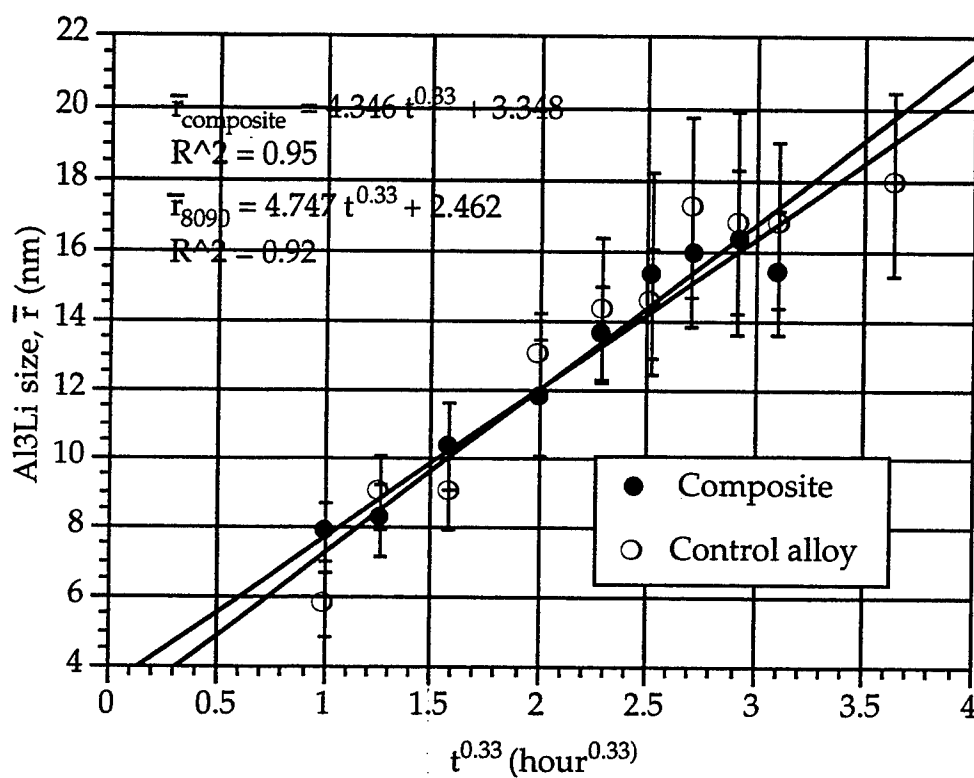


Figure 4.9 δ' radius, \bar{r} , as a function of $\sqrt[3]{t}$, where t is the aging time.

graph are the average values from both the vicinities of SiC particles and the SiC free regions. In common with the δ' coarsening in the control alloy, the δ' size development in the composite follows the LSW $\bar{r}-\sqrt[3]{t}$ rule.

4.4.2. S' Precipitation

The morphology of S' precipitates and its precipitation behavior have been discussed in detail in Chapters 2 and 3. The precipitation of the S' phase has been reported to be accelerated by a high density of dislocations in either pre-deformed materials [18] or composites [7, 10, 19, 20].

Figure 4.10 is a BF image micrograph taken from the region adjacent to a SiC particle. The sample was aged for 4 hours. Many S' laths can already be clearly identified in this micrograph. At the same time, it has been found that in the regions with low dislocation density in the composite, S' precipitates are rarely observed.

The precipitates of the S' phase were best examined after 25 hours of aging when the S' precipitates were found in all regions as shown in figure 4.11. In the matrix next to the SiC/matrix interface, there is a very high number density of S' precipitates. As the distance from the interface increases, the S' number density decreases continuously.

It is also interesting to notice that the size of the S' precipitates changes with distance from the interface. Finer S' precipitates are associated with a higher number density in the highly dislocated area immediately next to the SiC particles and the coarser S' precipitates are observed with a lower number density in the areas which are further away from the SiC particle.

By correlating the S' precipitation behavior with the already known dislocation distribution in the composite, it was assumed that the change in



Figure 4.10 S' precipitates in an area next to a SiC particle after 4 hours of aging.



Figure 4.11 S' precipitation behavior changes as the distance from the SiC/matrix interface increases. Finer S' laths are seen in the vicinity of the SiC particle (top) and coarser S' precipitates are away from the SiC particles.

the S' precipitation behavior is caused by the dislocation distribution in the composite. To confirm the above, the S' precipitation in an unreinforced 8090 sample, which had been deformed by ~3% before the aging treatment (the pre-deformed samples), has been examined. The S' precipitates in this sample after 25 hours of aging are shown in figure 4.12 in a CDF image. To make a comparison, the S' precipitates from the vicinities of SiC particles, SiC free regions in the composite and from the control alloy after the same aging time are also presented in figure 4.13 to figure 4.15. The comparison indicates that the S' precipitates in the pre-deformed 8090 alloy are very similar to those in the vicinities of SiC particles in the composite, in both size and distribution. On the other hand, the S' precipitates in the SiC free regions are similar to those in the control alloy. Therefore, it can be concluded that the dislocations in the composite do have an effect on the precipitation of S' precipitates. However, due to the localized dislocation distribution in the composite, the spatial extent of this effect is limited.

4.5. DIFFERENTIAL SCANNING CALORIMETRY (DSC) ANALYSIS

To further study the effect of dislocations on the S' precipitation kinetics in the bulk materials, differential scanning calorimetry (DSC) has been used. The reason for using DSC instead of quantitative microstructural measurements is that the DSC can monitor the precipitation kinetics in a very short time period. Although quantitative microstructural study using TEM is feasible, it is a time consuming and tedious process. The only disadvantage of the DSC method is that microstructural details which are associated with the precipitation kinetics are not available.



Figure 4.12 S' precipitates in the pre-deformed (~3%) 8090 sample after 25 hours of aging.

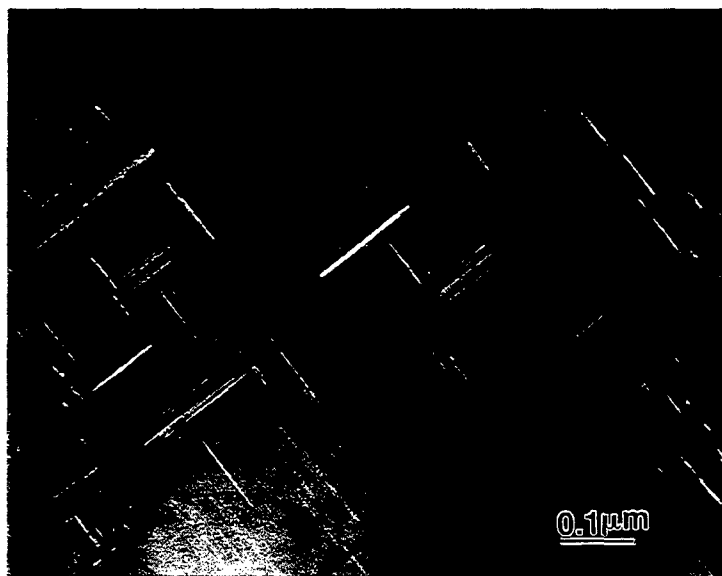


Figure 4.13 S' precipitates in the vicinity of a SiC particle in the composite after 25 hours of aging.

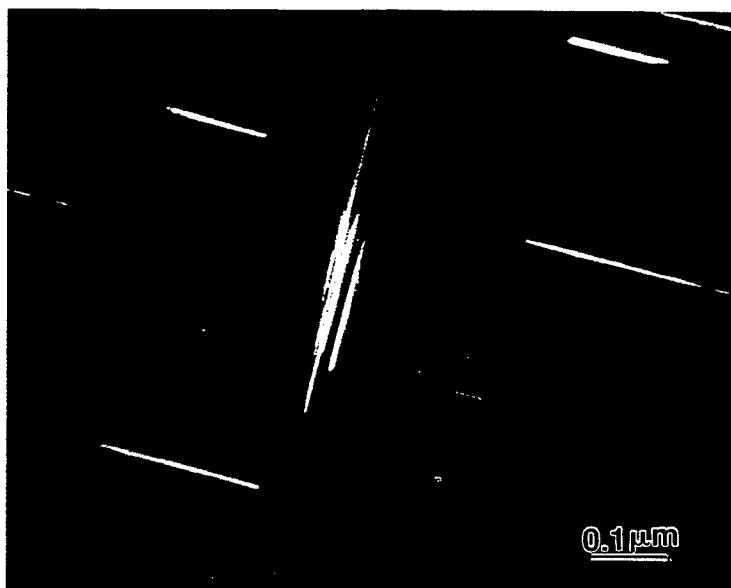


Figure 4.14 S' precipitates in a SiC free region of the composite after 25 hours of aging.



Figure 4.15 S' precipitates in the control alloy after 25 hours of aging.

4.5.1. Experimental

The specimens used for DSC analysis were: (1) as-quenched 8090 alloy, (2) as-quenched composite, (3) the pre-deformed 8090 alloy and (4) naturally aged 8090 alloy. The DSC samples were discs of 5 mm in diameter and 1 mm in thickness. They were solution treated at 536°C for 45 minutes in sealed glass tubes filled with helium gas and ice-water quenched. The as-quenched samples were stored in liquid nitrogen until the DSC experiment was conducted. The pre-deformed samples were stored in liquid nitrogen and deformed by ~3% immediately before the DSC experiment. The naturally aged samples were kept at room temperature for 26 hours before the DSC test.

The experiment was conducted on a PERKIN-ELMER 7 series thermal analysis system. Precipitation sequences in the temperature range of 0 - 480°C were examined at a heating rate of 10°C/min. Before the samples were tested, the instrument was calibrated using an indium sample. A pure aluminum pan was also heated through the experiment temperature range at the same heating rate to set a baseline. For each group, two samples were tested to check for consistency and reliability.

4.4.2. Results

The thermogram of the as-quenched control alloy, figure 4.16, shows three primary exothermic processes at 105°C, 175°C and 330°C, which have been designated as P1, P2 and P3, respectively. These exothermic processes have been determined by previous studies as, P1: GPB zone formation [7, 21, 22], P2: δ' precipitation and P3: S' formation [22-24]. The endothermic processes Q1 (~140°C) was reported to be associated with the dissolution of the Al-Li rich GP zones [22,25]. However, according to the high resolution

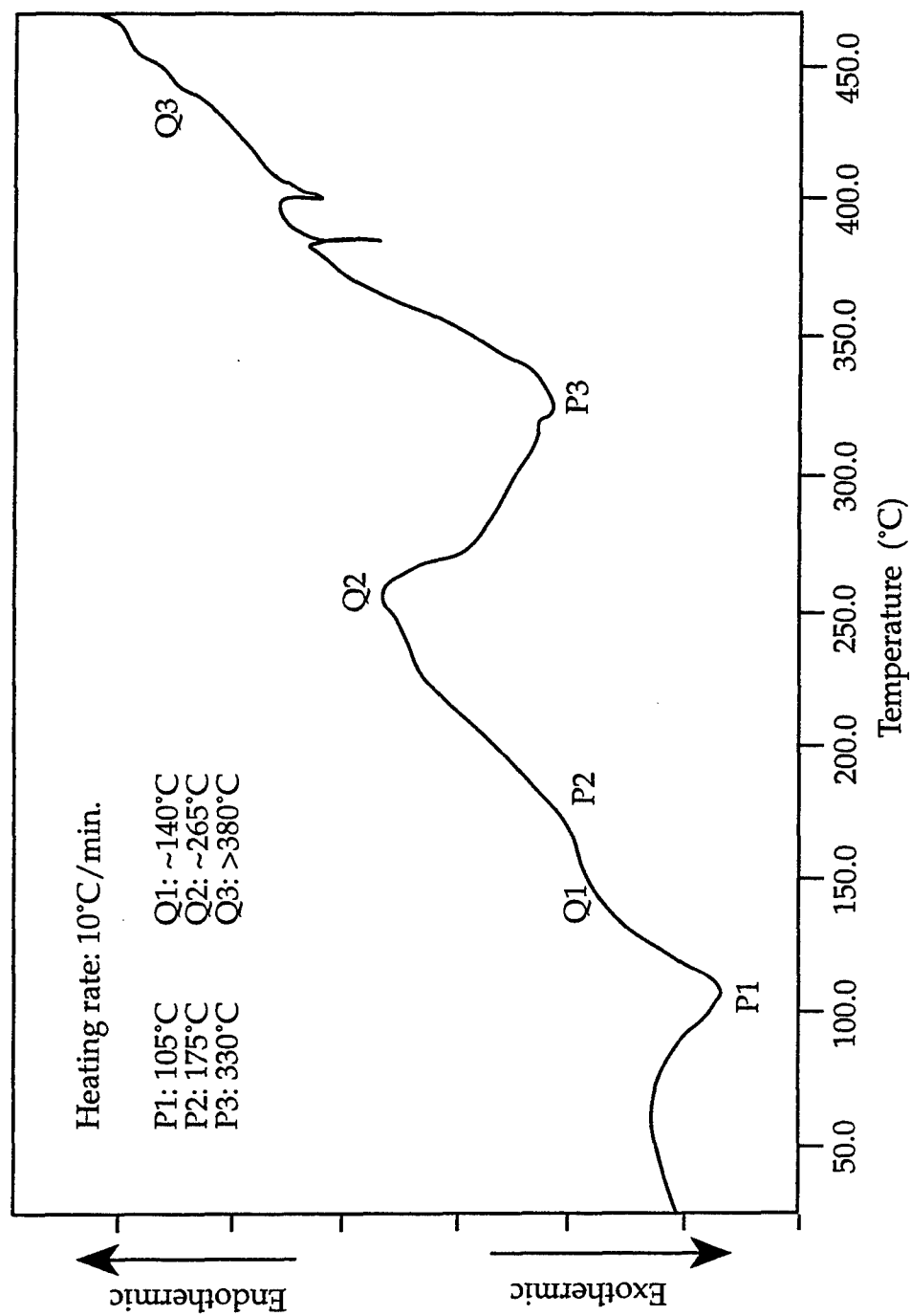


Figure 4.16 DSC thermogram of the as-quenched 8090 alloy.

electron microscopy examination conducted by Radmilovic et al [26], these so-called GP zones which formed during quenching are more likely the short range ordered domains in Al-Li alloys. Q2 ($\sim 265^{\circ}\text{C}$) composed of the dissolution of GPB zone [21] and the δ' phase [22-25], and Q3 ($> 380^{\circ}\text{C}$) is due to the dissolution of the S' phase ($380 - 400^{\circ}\text{C}$) plus δ phase [7,21].

In the composite, figure 4.17, although the precipitation sequences are the same as in the control alloy, some changes can be seen from the thermogram. P1 has been somewhat depressed while P2 has increased. However, the positions of P1 and P2 are still at the same temperatures as in the control alloy. An important phenomenon is that P3 has been shifted to a temperature around 310°C which is about 20°C lower than in the control alloy. This means that the precipitation of the S' phase in the composite is accelerated by the existence of SiC particles.

In the pre-deformed 8090 alloy, figure 4.18, the P1 process has almost disappeared from the thermogram. On the other hand, the P2 process has further increased as compared to the composite. In common with the composite, P3, has been shifted to around 310°C and the precipitation of the S' phase has been accelerated.

After 26 hour natural aging at room temperature, the thermogram of the control alloy (figure 4.19) does not show any significant difference as compared to the as-quenched control alloy. Although a previous study [23] reported the disappearance of the GPB zone formation peak (P1) after natural aging, this change has not been observed in the present study. Jena [21] examined an Al-Cu-Mg sample aged at room temperature for 48 hours and indicated that the GPB formation and dissolution were not changed as compared to the as-quenched samples. The present study is in agreement

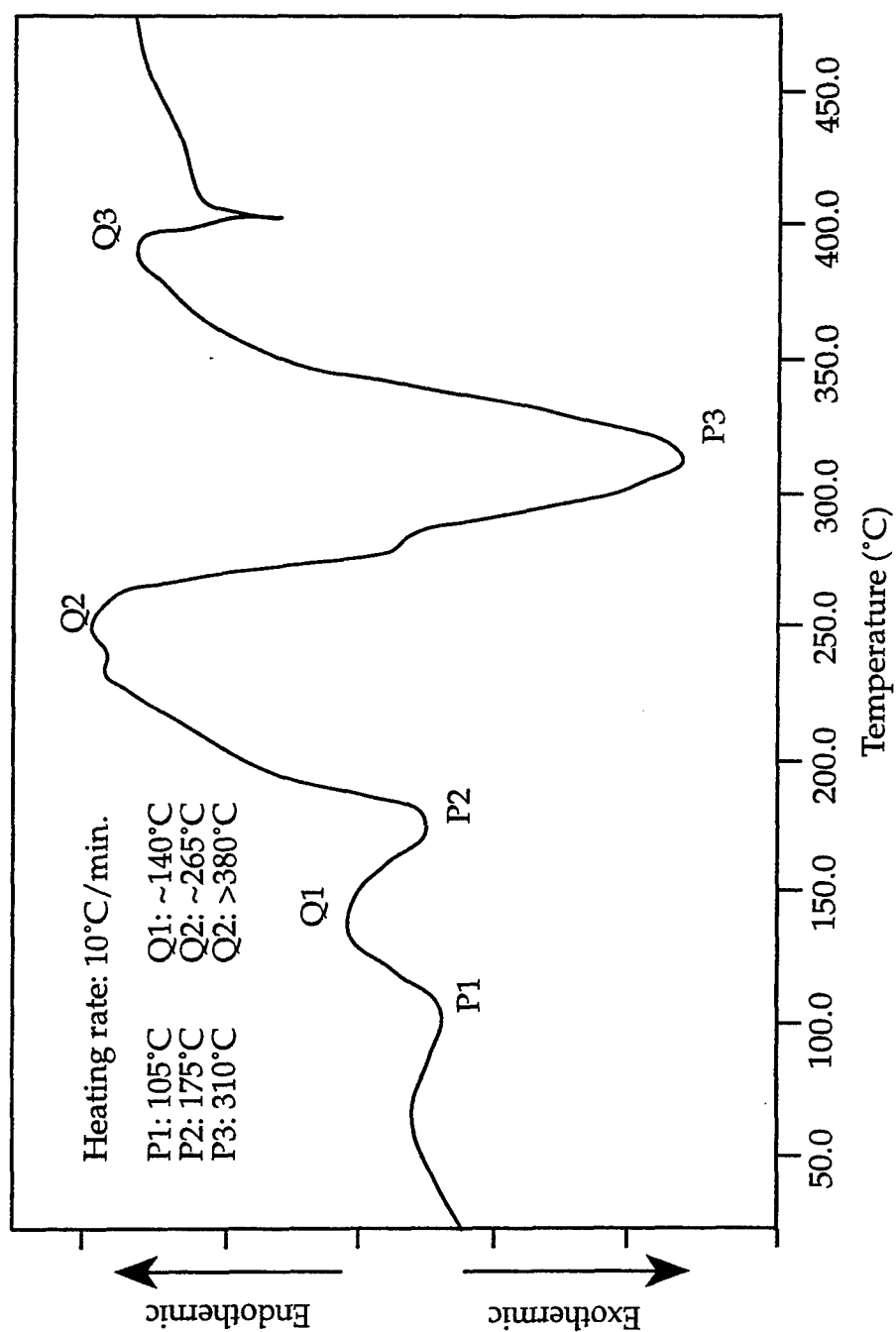


Figure 4.17 DSC thermogram of the as-quenched composite.

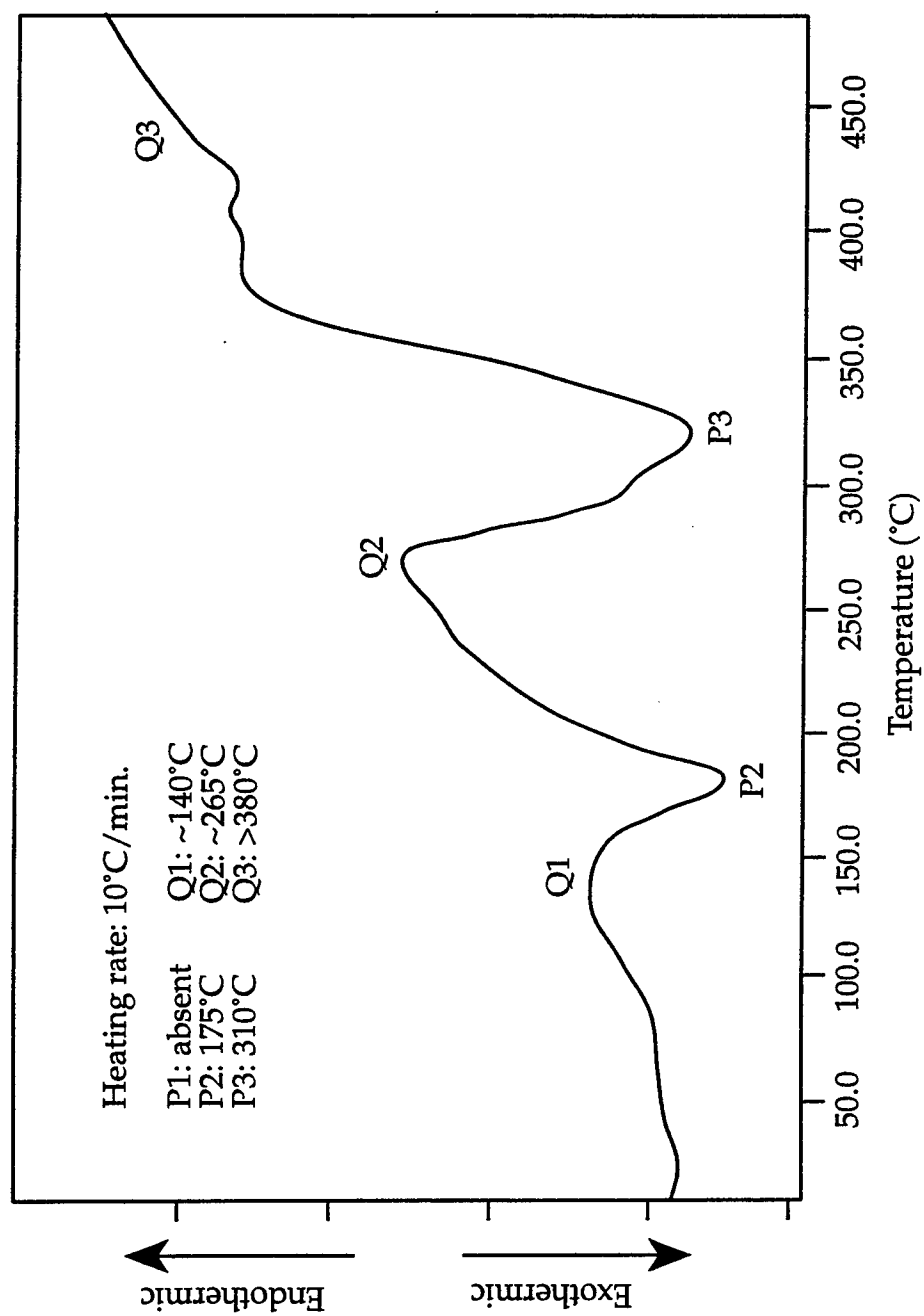


Figure 4.18 DSC thermogram of the pre-deformed 8090 alloy.

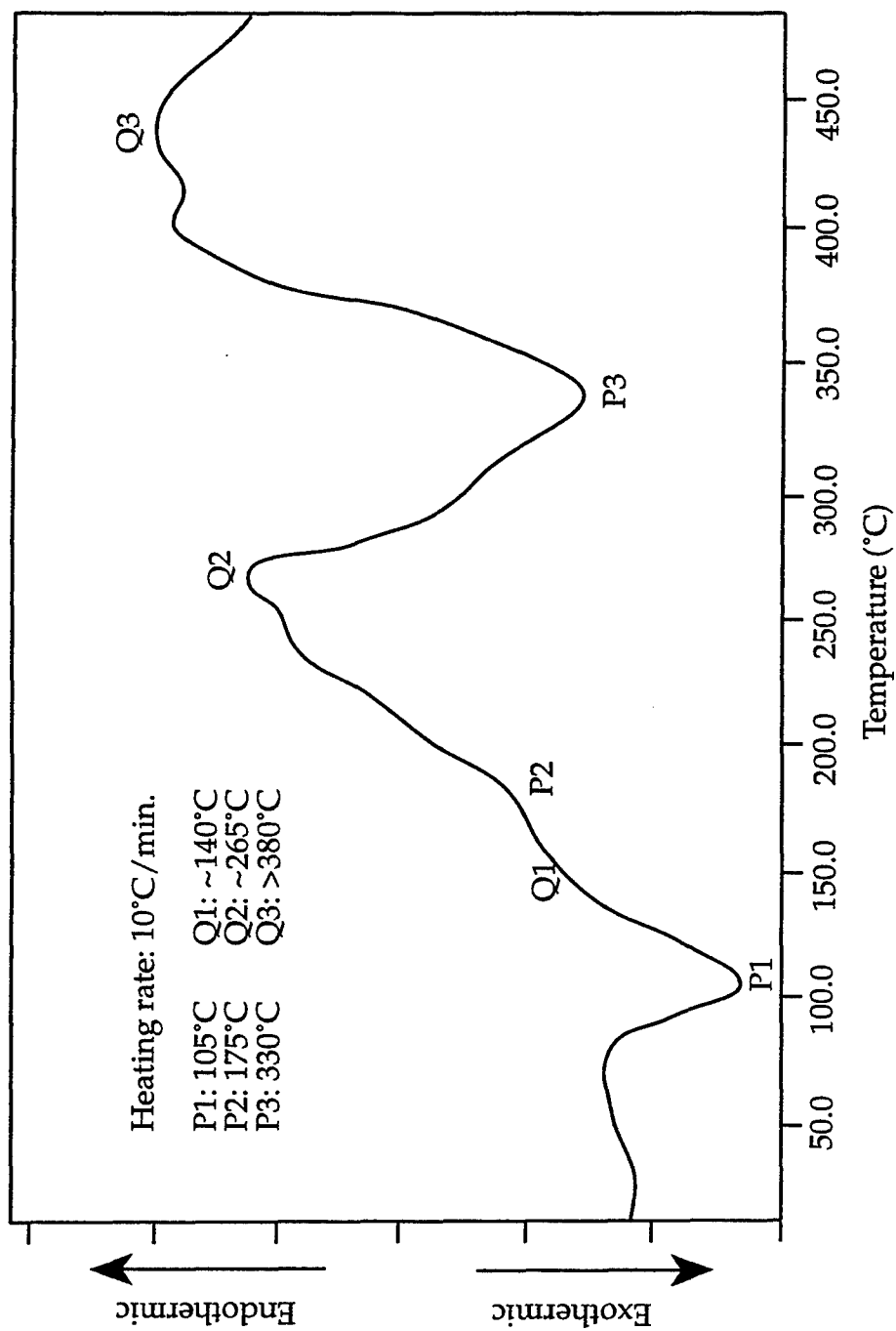


Figure 4.19 DSC thermogram of the 8090 alloy naturally aged for 26 hours at room temperature.

with both studies [22, 23] in that natural aging has no effect on the precipitation of the S' phase.

4.6. GRAIN BOUNDARY AND SiC/ α INTERFACIAL MICROSTRUCTURAL CHANGES

4.6.1. Experimental

The microstructural examination methods and samples used for the SiC/ α interfacial microstructural examination are identical to those described in section 4.3.1. TEM was still the principal technique to study the microstructural changes at SiC/ α interfaces. In addition, the specific areas of both grain boundaries and SiC/ α interfaces have been measured using the intercept method. Grain boundaries were revealed when etched with Keller's agent (HF:HCl:HNO₃:H₂O=1:1.5:2.5:95). Samples were then examined using scanning electron microscopy (SEM). By drawing lines in perpendicular directions on SEM micrographs and counting the number of intercepts of these lines with matrix grains and SiC particles, the specific area (S_v) of the grain boundaries and the SiC/matrix interfaces can be obtained through equation (4.2) [27]:

$$S_v = k \cdot N_L \quad (4.2)$$

where N_L is the number of the intercepts per unit test line length. The constant, k , in equations (4.2) are 2 and 4 for grain boundary and SiC/matrix interfaces, respectively, because the matrix is a continuous phase and SiC particles are discrete.

4.6.2. Results

The specific area is $0.34 \mu\text{m}^{-1}$ for the grain boundaries and $0.3 \mu\text{m}^{-1}$ for the SiC/ α interfaces in the composite. As the composite contains a large amount

of interfaces, the interfacial microstructural changes (if any) during aging would play an important role in determining the properties of the composite.

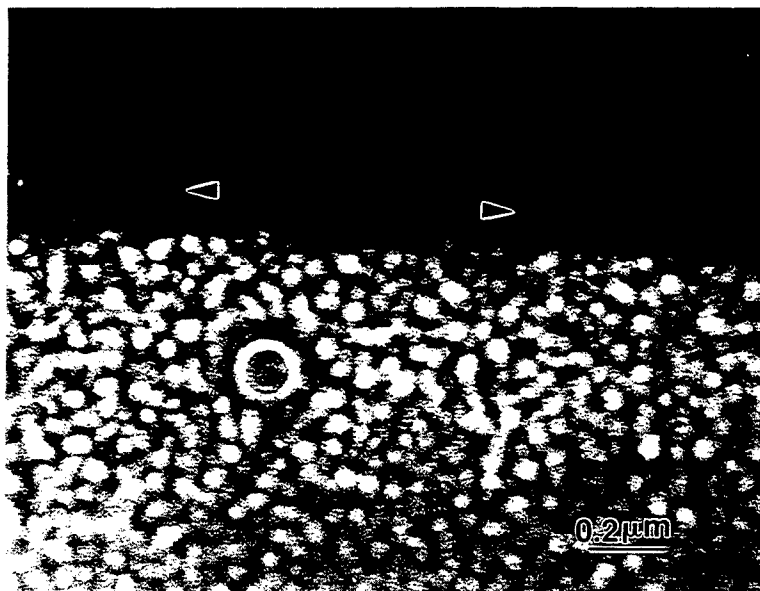
4.6.2.1. Interfacial precipitation and δ' PFZs

In common with the control alloy, δ' PFZs have been observed as early as after 1 hour aging at both grain boundaries and SiC/ α interfaces, as shown in figures 4.20a and b. These δ' PFZs further developed with prolonged aging times. The width of δ' PFZs at both grain boundaries and SiC/ α interfaces has been characterized quantitatively. Because the PFZs with abnormal low width in each sample were not included for the PFZ width measurement, the measurement results should be considered as the upper limits of PFZs in these samples. Due to time limitation, only the composite samples artificially aged for up to 12 hours were measured. The results are presented in table 4.3 together with the PFZ width obtained in the control alloy.

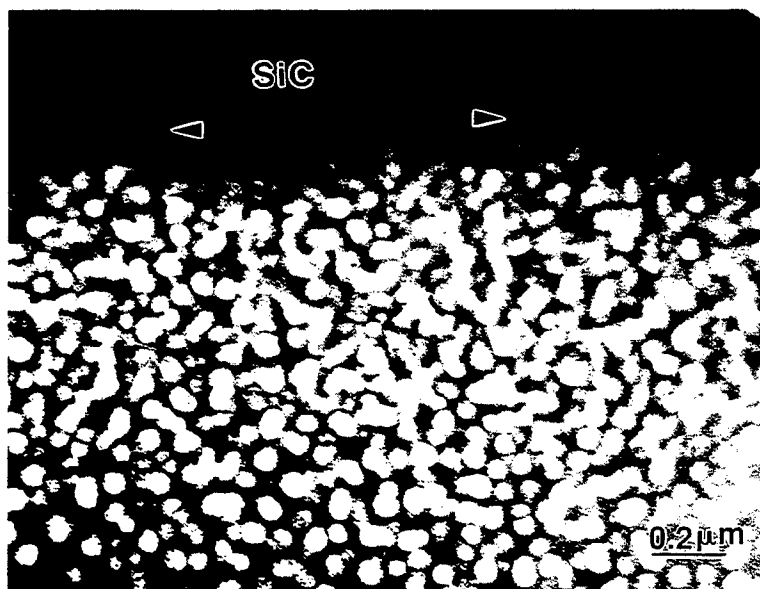
Table 4.3 δ' PFZ Development with Aging Times

aging time (hour)	Interfacial PFZ (nm) (composite)	Grain boundary PFZ (nm) (composite)	Grain boundary PFZ (nm) (control alloy)
1	33.1	34.8	20.8
4	66.9	61.2	31.4
8	57.0	56.4	57.8
12	78.7	78.3	62.9

From the results listed in table 4.3, it has been found that the development of δ' PFZs at SiC/ α interfaces is identical to that at high angle grain boundaries in the composite although both exhibit faster kinetics than the high angle grain boundaries in the control alloy.



(a) grain boundary (arrowed)



(b) SiC/ α interface (arrowed)

Figure 4.20 δ' PFZs in the composite after 1 hour aging.

With 1 hour aging, some grain boundary precipitates have been occasionally observed, as shown in figure 4.21. According to the results presented earlier in Chapter 2, these precipitates are either T_2 or δ phase. At this stage (1 hour aging) SiC/ α interfaces are usually very clean, such as the one presented in figure 4.22, which indicates that the interaction between the reinforcement and the aluminum matrix is suppressed during fabrication. Qualitative TEM examination also revealed that the population of precipitates at SiC/ α interfaces was less than at grain boundaries.

After 25 hour aging, precipitates can be seen at SiC/matrix interfaces, an example of such precipitates is given in figure 4.23a. From the microcrystalline nature, these precipitates are believed to be T_2 . The PFZs along the SiC/ α interfaces can also be seen in figure 4.23b.

4.6.2.2. S' Distribution along SiC/ α Interfaces

In common with the S' distribution along grain boundaries in the control alloy, S' were observed in the vicinities of SiC/ α interfaces. As compared to the δ' distribution shown in figure 4.24a, S' does not exhibit a well defined precipitate free zones along SiC/ α interfaces. However, a careful examination of figure 4.24b indicates that S' precipitates never extend to contact the SiC particle. There is a very narrow S' free zone.

4.7. DISCUSSION

4.7.1. Aging Kinetics of the Composite

In the 8090 matrix SiC reinforced composite used in present study, it has been observed that the aging response is not significantly affected by the existence of the reinforcement. Several previous studies on metal matrix



Figure 4.21 Precipitates at a high angle grain boundary in the composite after 1 hour aging.

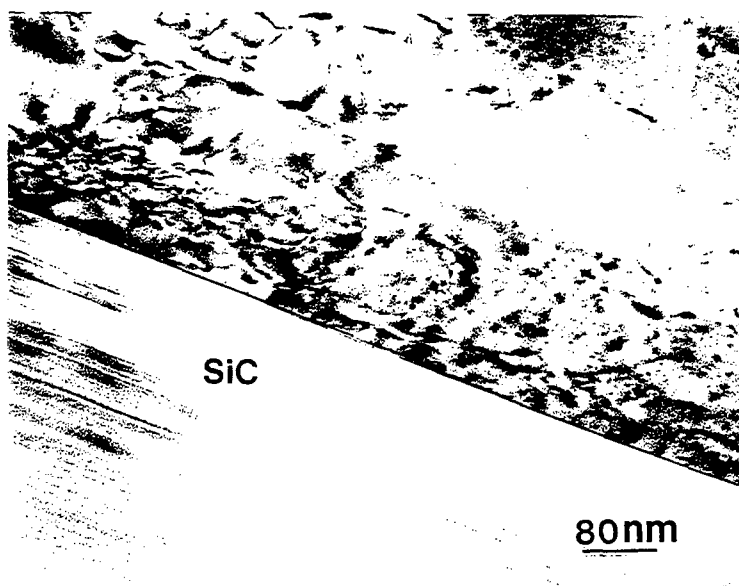
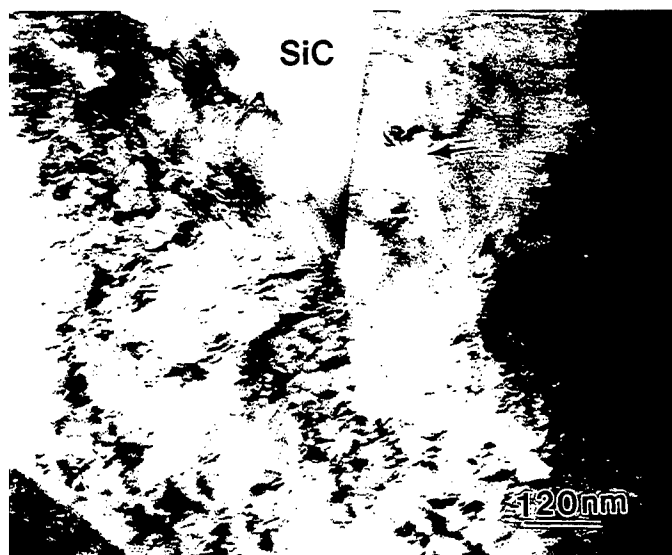
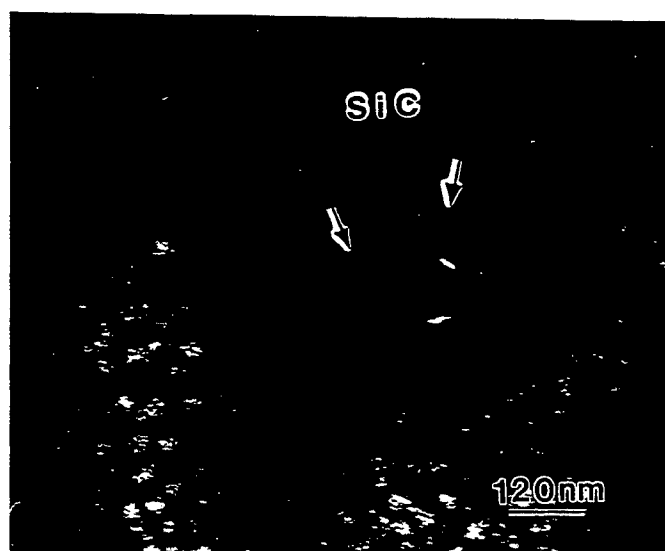


Figure 4.22 SiC/ α interface after 1 hour aging. No precipitates are present at the interfaces

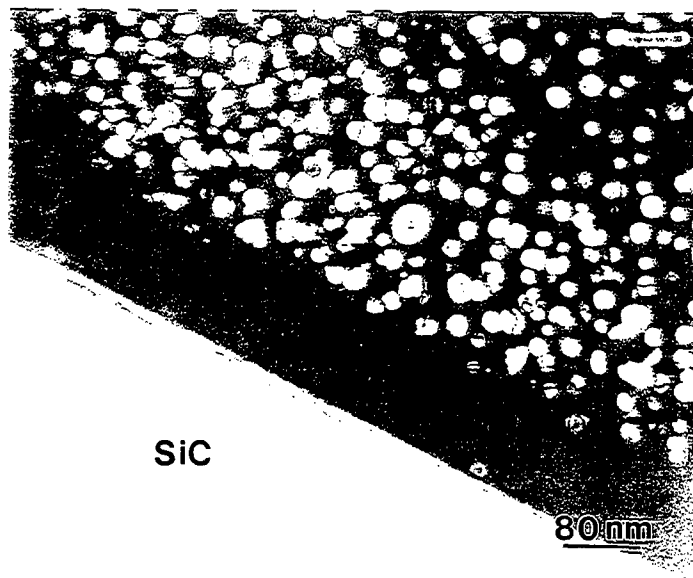
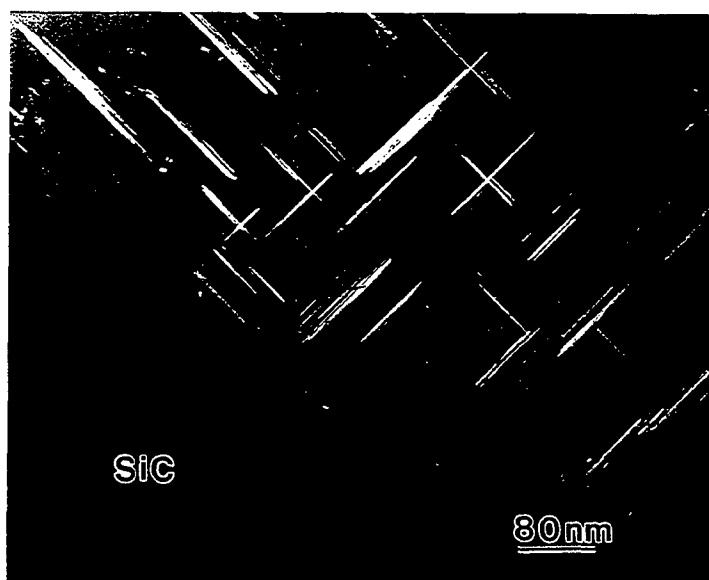


(a) precipitate at SiC/ α interface (arrowed)



(b) δ' PFZs at the same interface, interfaces are arrowed

Figure 4.23 SiC/ α interfacial precipitates and the associated δ' PFZ after 25 hour aging

(a) δ' CDF

(b) S' CDF

Figure 4.24 Comparison of the distribution of the δ' phase and the S' phase near a SiC/ α interface.

composites have claimed relatively uniform dislocation distribution in the matrix of these materials [9, 10, 20]. These dislocations accelerated heterogeneous nucleation of certain strengthening phases, such as the β'' and β' phases in 6061 matrix composites [9] and the S' phase in Al-Cu-Mg matrix composites[10]. Although a high density of dislocations caused by the differential contraction of the matrix alloy and SiC particles has been found in the matrix of the composite in the present study, the dislocation distribution is highly non-uniform. The DSC thermograms (figures 4.16 - 4.19) have shown that these dislocations accelerate the precipitation of the S' phase in the matrix of the composite. However, the microstructural examination results presented in figures 4.10 to 4.15 indicate that this acceleration can only occur in very limited regions, that is, in the vicinities of SiC particles. As stated earlier in this chapter, to avoid the interference of SiC, the microhardness data in the present study came from SiC free regions. In these regions, as shown in figures 4.5, 4.7 and 4.14, both the dislocation distribution and the S' precipitation are very similar to those in the control alloy. Therefore, it is reasonable that accelerated aging kinetics is not observed from the microhardness data.

The microhardness test results from the pre-deformed samples support the above conclusion. In the as-quenched condition (aging time 0 hour in figure 4.4), the hardness of the pre-deformed sample is much higher than that of the non-deformed material because of the high density of dislocations in the former material. In the early stage of the aging treatment, with the precipitation of the δ' particles, the hardness of both materials increases significantly. The effect of a high density of dislocations on the hardness seems to become less important so that after 1 and 2 hours aging, the hardness

values of the two materials are actually very close. However, with further aging, such as after 4 hours of aging, the pre-deformed material starts to strengthen at a higher rate than the control alloy. Although the microstructure after 4 hour aging has not been examined in the pre-deformed sample, the microstructural examination of the vicinity of SiC in a composite sample aged for 4 hours was presented in figure 4.10. Because the microstructure of pre-deformed samples are similar to the vicinities of SiC in the composite (figures 4.12 and 4.13), the microstructural development in the vicinities of SiC in the composite can be considered as indicative of the precipitation in the pre-deformed material. In figure 4.10, many S' laths can be clearly seen. On the other hand, only very few S' precipitates can be seen in the control alloy after the same aging time, such as those shown in figure 4.25. Therefore, with 4 hours of aging, the δ' phase is the sole strengthening phase in the control alloy. On the other hand, the strengthening in the pre-deformed material comes from the δ' plus S' phases. With the additional strengthening contribution from these S' precipitates, the hardness of the pre-deformed samples would be higher than the control alloy samples with 4 hour or even longer aging time. The high strengthening rate in the pre-deformed samples is the result of the accelerated strengthening or aging kinetics in this material as compared to the control alloy. The disappearance of the second aging peak in figure 4.4 can also be attributed to the result of S' strengthening being shifted to the shorter time.

As indicated earlier, with the second aging peak, the hardness of the control alloy and the composite recovered to the same level as with the first aging peak (figure 4.2). In the non-deformed 8090 alloy, which was not naturally aged between the solution treatment and the artificial aging at



Figure 4.25 S' precipitation in the control alloy after 4 hours of aging. S' laths are arrowed.

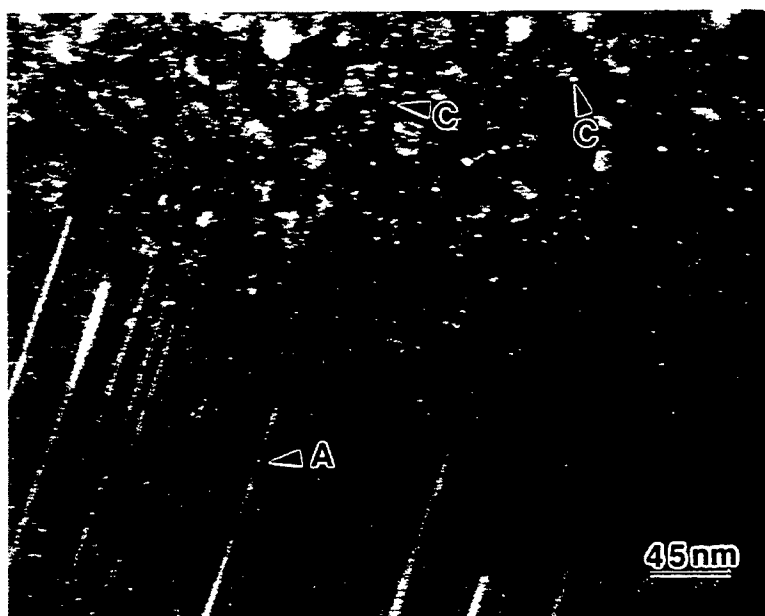
190°C, the recovery of the second aging peak was more moderate (figure 4.4). The material could not achieve the same hardness as with first aging peak. In Chapter 3, it has been shown that after natural aging, many dislocation loops and helices and probably vacancy clusters were generated in the material. These same defects were not observed in the as quenched 8090 sample. Because these defects are preferential nucleation sites for the S' phase in the non-deformed 8090 alloy, the S' precipitation is less well developed as compared to the control alloy. TEM examination indicates that although a considerable amount of S' types A, B and C have been observed in the sample experienced natural aging plus artificial aging (figure 2.9), type A was much less numerous and can only be seen at some dislocation lines in the sample artificially aged for 16 hours immediately after solution treatment (figure 4.26a). In this sample, type B was hardly observed although S' type C was still observed in a considerable quantity as shown in figure 4.26b. It is very likely that the S' type A and type B have been suppressed due to the shortage of dislocation loops and vacancy clusters. Therefore, the second aging peak is not as strong as in the material without previous natural aging.

4.7.2. Dislocation Distribution in the Composite

In composites, the ratio of $\frac{w}{r}$ is used to describe the size of the highly dislocated regions, where w is the distance from the center of the reinforcement to the edge of the highly dislocated region and r is the radius of the reinforcement, as schematically shown in figure 4.27. For most of the observations in the present study, the $\frac{w}{r}$ ratio is ≤ 2 . Dutta et al [28] calculated the size of the plastically deformed zone near reinforcements in composites using a finite element method (FEM). Their results indicate that in the



(a) S' type A nucleated at dislocation lines



(b) S' type A at dislocations and type C dispersed within the matrix

Figure 4.26 S' precipitates in a 8090 sample aged for 16 hours at 190°C immediately after solution treatment.

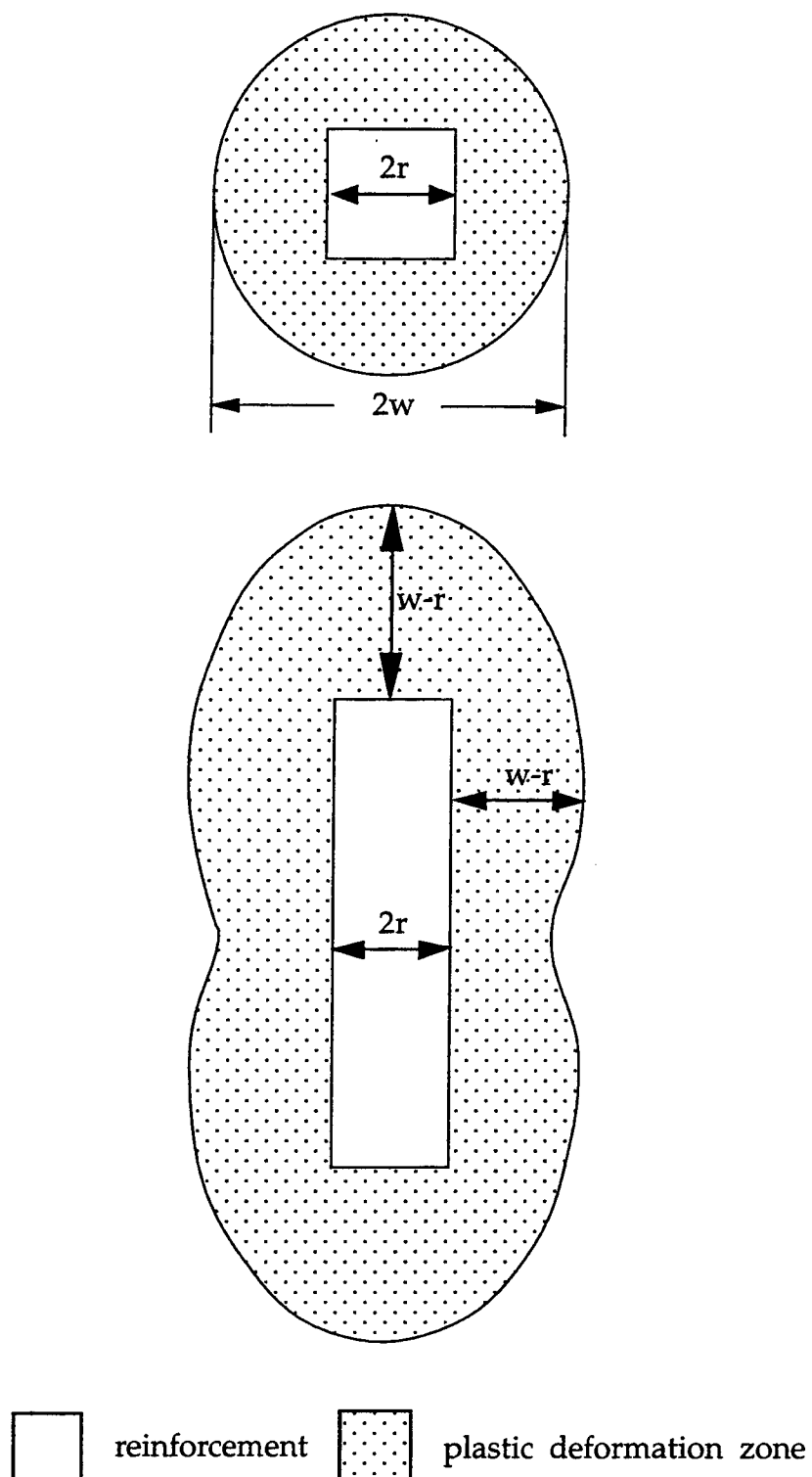


Figure 2.27 Plastic deformation zones in the matrix around reinforcement.
(top: aspect ratio ≈ 1 ; bottom: aspect ratio >1)

Al/SiC composite system, for a matrix yield strength of 200 MPa and SiC particles with an geometric aspect ratio of 1 to 3, the $\frac{w}{r}$ value is 1.8 to 2, which is very close to the assessment made in this thesis study. Because the volume fraction of the SiC particles in the composite used in this thesis study is around 17%, with a $\frac{w}{r}$ value of 2, the volume fraction of the highly dislocated area plus the SiC particles is about 34%. This also means that less than a quarter of the matrix in this composite is highly dislocated.

Plastic deformation in the vicinities of SiC particles increased the dislocation density, and also influenced the dislocation configurations. The dislocations are helices and loops in SiC free regions (figure 4.7) but are curved and tangled in the vicinities of SiC particles (figure 4.6). Similarly, dislocations in the control alloy, as shown in figure 4.8, are mostly helices and loops. The tangled dislocation lines in the vicinities of SiC particles are the products of plastic deformation. On the other hand, as discussed earlier in Chapter 3, dislocation loops and helices were the result of vacancy condensation [29-31] during the 6 month natural aging. It is very likely this condensation continued during artificial aging at 190°C. Therefore, the dislocation loops and helices are not related to the plastic deformation associated with the differential contraction between the SiC and the α matrix.

4.7.3. Precipitation in the Composite

4.7.3.1. δ' Precipitation

Although previous study [7] suggested that the coarsening of the δ' phase may be retarded in composites, the quantitative measurement in the present study (table 4.2) does not show any difference between the sizes of the δ'

precipitates in the vicinities of SiC particles and in SiC free regions. Moreover, as shown in figure 4.9, the coarsening of the δ' phase in the composite is actually the same as in the control alloy. The thermograms of DSC analyses from both the control alloy and the composite also indicate that the P2 exothermic peaks associated with the formation of the δ' phase in the two materials are at almost the same position. In previous study [7], the reason for the retarded growth of the δ' phase has been explained as the result of a decreased solute volume diffusion rate due to the depletion of vacancies in the composite. However, it should be noticed that these vacancy depleted regions are also highly dislocated. The volume diffusion rate could be both retarded by the vacancy depletion and promoted by the short circuit diffusion paths through the dislocations. Eventually, the effects from the depletion of vacancies and the dislocation short circuits may have been offset so that the growth of the δ' phase is actually unchanged.

4.7.3.2. S' Refinement

In Christman and Suresh's study on the aging behavior of a 2124/SiC composite [10], in addition to the accelerated nucleation of S' in the composite, the length of S' precipitates in the composite was also found to have increased when compared with the unreinforced 2124 alloy. However, the microstructural examination results in the present study indicated that although a significantly higher number density of S' precipitates formed in highly dislocated regions, the size of these precipitates could be smaller than those in the control alloy. This refinement of the S' precipitates occurs after relatively long aging times. After 25 hours, S' precipitates in highly dislocated regions in figures 4.12 and 4.13 are significantly finer than in the low

dislocation density areas (figures 4.14 and 4.15). A similar refinement of the S' precipitates in highly dislocated regions was also observed in pre-stretched samples by Wilson and Forsyth [32]. However, the S' precipitates after 4 hour aging are larger in the vicinity of a SiC particle (figure 4.10) than in the control alloy (figure 4.25). Although the high density of dislocations may promote the nucleation of the S' phase and provide short circuits for Cu and Mg diffusion in the early stages of aging, the growth of these laths may also be hindered by the shortage of solute supply caused by the high density of S' precipitates in the later stages of aging. In the earlier stages of aging, such as after 4 hours, because the dislocations accelerated the nucleation of S' phase, the S' precipitates in highly dislocated regions can grow to a larger size as compared to the low dislocation density regions. After a long time of aging, such as 25 hours, with the higher number density of the S' phase, the solute flux in the composite and the pre-deformed material would be lower than in the control alloy. The growth of the S' laths is consequently retarded.

4.7.4. Precipitation Sequence

In addition to the acceleration of the S' precipitation, another change shown in the thermogram of the composite is the formation of GPB zones, that is, the P1 exothermic peak. As compared to the control alloy, the P1 peak in the composite was diminished. Moreover, in the pre-deformed sample (figure 4.18), the P1 peak has almost disappeared. It appears that the GPB zone formation during heating decreases as the dislocation density increases.

A similar decrease trend in GPB zone formation has been reported by previous studies in several different aluminum matrix composites [7-9, 13, 19]. The interpretations of this phenomenon can be divided into two

completely different categories. The first type of interpretation suggests that the high density of dislocations in composites promotes the formation of GPB zones so that these GPB zones may have mostly formed during the quench with the help of those dislocations which formed during the same process [8, 9]. Therefore, the GPB zone formation during the heating process is suppressed. The second type of interpretation considers the numerous reinforcement/matrix interfaces and dislocations in the composites as sinks for vacancy annihilation [13, 19]. As a high density of vacancies will favor GPB zone formation by facilitating solute diffusion and providing nucleation sites at vacancy clusters, the depletion of vacancies due to the annihilation would suppress GPB zone formation.

The first interpretation is based on the fact that a high density of dislocations was formed during quenching. Hence, GPB zone formation could be promoted significantly during quenching. However, this explanation can not explain the results observed in the pre-deformed samples in the current study. The pre-deformed samples were deformed after quenching. Hence, the GPB zone formation during quenching is equivalent to that in the control alloy. The deformation was conducted at room temperature. After deformation, the samples were stored at subzero temperature for 1-2 hours until the DSC experiment was conducted. It is virtually impossible for GPB zone formation to occur after deformation and before the DSC experiment. Hence, the second interpretation, that is GPB zone suppression, might be more likely. Comparing figures 4.16 -4.18, it can be seen that when the GPB formation peak, P1 is strong, the δ' precipitation, P2 is weak (such as in the control alloy, figure 4.16). With the decrease of P1, P2 becomes more and more strong (figures 4.17 and 4.18). It was mentioned

earlier that the dissolution of the GPB zones occurs at 140 - 240°C, which is overlapped with the precipitation of the δ' phase. The heat absorbed by the GPB zone dissolution will partially offset the heat released by the δ' precipitation. Hence, with significant GPB formation, the dissolution of the GPB would decrease the P2 peak as in figure 4.16. As the GPB formation is depressed, the dissolution of the GPB also decreases and the P2 peak becomes more and more significant as shown in figures 4.17 and 4.18. Hence, as already proved by microstructural examination, the precipitation of the δ' phase does not change in the composite as compared to the control alloy. The P2 peak change in the thermograms of figures 4.16-4.18 is due to the suppression of GPB zone formation in highly dislocated materials, such as the composite and the pre-deformed 8090 alloy.

As mentioned above, the mechanism of the GPB suppression has been suggested by Friend and Lexton [13] and Papazian [19] to be due to the annihilation of vacancy clusters and mobile vacancies at either dislocations or the large quantity of interfaces in composites. Again, it could be argued that in Al-Li alloys there are very few mobile vacancies because of the strong binding energy between Li atoms and vacancies. As shown in Chapter 3, although dislocation loops and helices have been observed in the 6 months naturally aged control alloy (figure 3.16), they were rarely seen in the as-quenched 8090 alloy (figure 3.15). The thermograms for the pre-deformed material were obtained from samples which had not been naturally aged. Hence, a lack of vacancies is unlikely to cause the observed suppression.

Graf and Guinier's study [33], quoted by Kim et al [34], proposed another possibility concerning the formation of θ'' in Al-Cu alloys. The nucleation of θ'' was suppressed by deformation in their Al-Cu alloys. They proposed that

the formation of the θ'' phase was facilitated by the segregation of atoms on {100} plane. Plastic deformation distorted the atom planes and made the segregation more difficult and consequently retarded the formation of the θ'' phase. A similar mechanism might also lead to the suppression of GPB zones observed in the present study. In addition, GPB zone suppression in the composite and the pre-deformed 8090 alloy could be the result of solute segregation to dislocations in these two materials. As GPB zones are Cu and Mg rich clusters, with the segregation of these atoms to dislocations, the depletion of these solutes is expected in the matrix. Therefore, the GPB zone formation would consequently be depressed.

4.7.5. Interfaces

TEM examination indicated that the microstructural development at SiC/ α interfaces is similar to that at high angle grain boundaries. Equilibrium phases, T_2 and probably δ tend to nucleate at these locations. Consequently, δ' PFZs are formed along these interfaces and boundaries. Although the precipitates at SiC/ α interfaces may affect the properties of composites adversely, it is worthwhile noting that the precipitation and PFZ formation are no worse at these locations than at grain boundaries. From TEM observation, the frequency of finding precipitates at grain boundaries is higher than at SiC/ α interfaces. In addition, although the PFZ width vs. time relationship suggested a diffusion control mechanism for the δ' PFZ development, the development of these PFZs along SiC/ α interfaces has not been accelerated by the expected faster solute diffusion caused by the high density of dislocations in the vicinities of SiC particles as compared with the PFZ development at grain boundaries in the same material.

The excellent strengthening potency of S' phase in aluminum alloys has been confirmed by many previous studies [35-37]. The present study has revealed another advantage of S' as a strengthening phase in aluminum matrix composites, that is, the good interfacial microstructural characteristics. S' phase does not form any wide precipitate free zones along either grain boundaries or SiC/matrix interfaces. Although the precipitation of S phase (which is suggested to be the equilibrium version of S' phase in some studies ([38, 39] quoted by Silcock [40])) has been documented at high angle grain boundaries [41], this precipitation has never been related to S' precipitate free zones in the vicinity. The difference between S' and S phases is still in dispute. The present study has not provided any evidence of S' or S phase formed at either high angle grain boundaries or at SiC/matrix interfaces. Hence, in Al-Cu-Li-Mg alloys and the composites having these alloys as matrices, the S' phase plays a very important role in compensating some disadvantages caused by the δ' phase strengthening, such as, co-planar slip and PFZs along grain boundaries and reinforcement/matrix interfaces. Currently, the obstacle to fully develop the strengthening potential of the S' phase is that the S' phase is usually formed after a relatively long time during aging when the boundary precipitation becomes a concern. However, as indicated earlier, a pre-stretch or naturally aging for long time period can significantly enhance the kinetics of S' precipitation.

4.8. CONCLUSIONS

1. The aging kinetics of the Al-Li matrix SiC particulate reinforced composite did not exhibit any significant change as compared to the control alloy.

2. In the composite studied in the present work, both the dislocation distribution and the precipitation distribution were highly non-uniform.
3. Of the two predominant strengthening phases in the 8090 alloy, the δ' phase was not affected significantly by the existence of the reinforcement. The heterogeneous nucleation of S' was promoted by the high density of dislocations in the vicinities of the SiC particulates in the composite.
4. Natural aging prior to artificial aging can promote the formation of the S' precipitates and enhance the strengthening result in materials.
5. In Al-Li-Cu-Mg materials, GPB zone formation could be suppressed by a high density of dislocations.
6. SiC/aluminum interfaces in composites act similarly to the high angle grain boundaries in the development of interfacial precipitation and the associated δ' PFZs.

4.9. REFERENCES

1. M. Hunt, *Mater. Eng.*, 6, (1991), p27.
2. A. Mortensen & M. J. Kocauk, *JOM*, 45, (1993), p9.
3. R. J. Arsenault: *Proc. the 3rd Japan-U.S. Conference on Composite Materials*, , K. Katawa, S. Umekawa, and A. K. Kobayashi, eds., Tokyo, 1986, p521.
4. *Aluminum Standards and Data 1978 Metric SI*, The Aluminum Association, Washington, DC 20006, p32.
5. M. Vogelsang, R. J. Arsenault, and R. M. Fisher: *Metall. Trans.*, 17A, (1986), p379.

6. K. K. Chawla, A. H. Esmaili, A. K. Datye, and A. K. Vasudevan: *Scripta Metall.*, 25, (1991), p1315.
7. E. Hunt, P. D. Pitcher, and P. J. Gregson: *Scripta Metall.*, 24, (1990), p937.
8. I. Dutta, C. P. Harper, and G. Dutta: *Metall. Trans.*, 25A, (1994), p1591.
9. I. Dutta, S. M. Allen, and J. L. Hafley: *Metall. Trans.*, 22A, (1991), p2553.
10. T. Christman and S. Suresh: *Acta metall.*, 36, (1988), p1691.
11. R. J. Arsenault and R. M. Fisher: *Scripta Metall.*, 17, (1983), p67.
12. S. I. Hong and G. T. Gray III: *Acta metall.*, 40, (1992), p3299.
13. C. M. Friend and S. D. Lexton: *J. Mater. Sci.*, 23, (1988), 3173.
14. F. S. Lin, S. B. Chakraborty & E. A. Starke, *Metall. Trans.*, 13A, (1982) p401.
15. M. H. Tosten, A. K. Vasudevan & P. R. Howell, *Aluminum-Lithium Alloys III*, Institute of Metals, London, (1986), p490
16. S. Suresh, A. K. Vasudevan, M. Tosten & P. R. Howell, *Acta. Metall.*, 35, (1987), p25.
17. P. Hirsch, A. Howie, R. Nicholson, D. W. Pashley, and M. J. Whelan: *Electron Microscopy of Thin Crystals*, Krieger Publishing Co. Malabar, Florida, (1967), p422.
18. M. Ahmad and T. Ericsson: *Aluminum-Lithium Alloys III, Proc. 3rd International Aluminum-Lithium Conference*, C. Baker, P. J. Gregson. S. J. Harris and C. J. Peel eds., University of Oxford, England, July 8-11, 1985, p509.
19. J. M. Papazian: *Metall. Trans.*, 19A, (1988), p2945.
20. J. Lin, P. Li, and R. Wu: *Scripta Metall.*, 28, (1993), p281.
21. A. K. Jena. A. K. Gupta, and M. C. Chaturvedi: *Acta metall.*, 37, (1989), p885.

22. A. K. Mukhopadhyay, C. N. J. Tite, H. M. Flower, P. J. Gregson, and F. Sale: *J. de Physique*, Supplement, C3, (1987), p439.
23. A. Luo, J. Lloyd, and W. V. Youdelis: *Acta metall.*, 41, (1993), p769,
24. P. J. Gregson, K. Dinsadale, S. J. Harris, and B. Noble: *Mater. Sci. Tech.*, 3, (1987), p7.
25. J. M. Papazian, C. Sigli, and J. M. Sanchez: *Scripta. Metall.*, 20, (1986), p201.
26. V. Radmilovic, A. G. Fox, and G. Thomas: *Acta metall.*, 37, (1989), p2385.
27. A. G. Guy and J. J. Hren: Elements of Physical Metallurgy, 3rd Edition, Addison-Wesley Publishing Company, Inc., (1974), p233.
28. I. Dutta, D. L. Bourell, and D. Latimer: *J. Comp. Mater.*, 22, (1988), p829.
29. G. Thomas and M. J. Whelan: *Phil. Mag.*, 4, (1959), p511
30. G. Thomas: *Phil. Mag.*, 4, (1959), p1213
31. M. Kiritani and S. Weissmann: *J Applied Phys.*, 42, (1971), p2603
32. R. N. Wilson and p. J. E. Forsyth: *J. Inst. Metals*, (1966), p8
33. R. Graf and A. Guinier: *Compt. Rend.* 238, (1954), p2175
34. T. S. Kim, T. H. Kim, H. H. Oh, and H. I. Lee: *J. Mater Sci.*, 27, (1992), p2599.
35. P. J. Gregson and H. M. Flower: *Acta metall.*, 33, (1985), p527.
36. W. S. Miller, M. P. Thomas, D. J. Lloyd and D. Creber: *Mater. Sci. Tech.*, 2, (1986), p1210.
37. C. P. Blankenship Jr.: *PhD dissertation*, University of Virginia, (1992).
38. H. Lambot: *Mem. Acad. Roy. Belg., Classe Sci.*, 26, (1950), p1609.
39. Yu. A. Bagaryatsky: *Zhur. Tekhn. Fiziki*, 18, (1948), p827 (Fulmer Research Inst. Translation N0.12).
40. J. M. Silcock: *J. Inst. Metals*, 89, (1960), p203

41. S. R. Nutt and R. M. Carpenter: *Mater.Sci.*, 76, (1985), p169.

CHAPTER 5

CONCLUSIONS AND SUGGESTIONS FOR FUTURE WORK

5.1. SUMMARY OF THIS THESIS

The aging behavior and the associated microstructural development of the 8090 alloy as well as an 8090/SiC composite has been studied in depth. In addition to the excellent strengthening when aged at 190°C, the 8090 alloy has been found to exhibit good stability up to 30 hours. The primary reason for this stability is the precipitation of two strengthening phases, δ' and S' , formed at the different aging stages. The present study indicates that the majority of the strengthening in the 8090 alloy comes from the δ' phase. Although the formation of S' precipitates at a later aging stage helped the alloy to sustain a high hardness, the formation of grain boundary precipitates of the T_2 and δ phases may lead to degradation of mechanical properties.

Despite the low vacancy mobility in Al-Li alloys, 6 months natural aging resulted in significant vacancy rearrangement. This rearrangement led to the existence of many dislocation helices and loops as well as vacancy clusters all of which generated preferential nucleation sites for S' precipitation. In contrast to the loops observed in other aluminum alloys, most of these loops lay on $\{210\}_\alpha$ planes which is the habit plane of the S' phase. Natural aging prior to artificial aging promoted the precipitation of the S' phase as compared to the non natural aged material and therefore provided another path for the acceleration of the S' precipitation.

S'/α interfacial coherency has been re-evaluated. Detailed study on the atomic matching across the interfaces indicates that although the $(010)_{S'}$ and the $(001)_{S'}$ interfaces are coherent or semi-coherent, the atomic matching at the $(100)_{S'}$ interfaces is very poor. Therefore, the S' will grow as a lath.

Based on the morphology and nucleation mechanism, S' precipitates in Al-Li-Cu-Mg alloys are classified into three types, A, B, and C. Type A precipitates nucleate at dislocations and exhibit a sheet-like morphology; type B likely nucleate at vacancy clusters and exhibit the lath morphology; type C nucleate at $\delta'/$ matrix interfaces at the later aging stage and are distributed uniformly within the matrix as fine laths.

The aging response of the SiC particulate reinforced 8090 matrix composite did not exhibit any acceleration as compared to the unreinforced 8090 alloy (the control alloy). The essential reason for the almost identical aging kinetics in both materials is the non-uniform dislocation distribution in the composite, which is characterized by highly dislocated regions limited to the vicinities of SiC particles. The experimental results achieved good agreement with the theoretical modeling from a previous study in that, with the amount of reinforcement employed, a non-uniform dislocation distribution would be expected.

The development of the δ' phase in the composite did not exhibit any difference as compared to the control alloy. This indicates that the dislocations in the composite have no effect on the precipitation of homogeneously nucleated precipitates. However, the precipitation of heterogeneously nucleated precipitates, such as the S' phase was accelerated by the high density dislocations in composites. However, the acceleration was restricted to the regions adjacent to the SiC particles. In addition, acceleration

does not necessary lead to coarser precipitates in the composites. The high density of dislocations refines the S' distribution, especially after long aging times.

SiC/ α interfaces were preferential nucleation sites for equilibrium precipitates, such as the T2 and δ phases. However, these interfaces were not as efficient as grain boundaries. At the early aging stage, such as 1 hour, the interfaces were usually free of precipitates.

5.2. FUTURE WORK

Based on the results obtained in this thesis study, the following work is suggested for the future work:

1. S' precipitation acceleration and the property improvements in Al-Li-Cu-Mg alloys.

The present study shows that Al-Li-Cu-Mg alloys and composites can be strengthened by the co-precipitation of δ' and S' phase. However, because S' precipitation is usually accompanied by grain boundary or reinforcement/matrix interface precipitation in these materials, the strengthening potential may be limited. To fully develop the strengthening potential, it is necessary to find a effective method to accelerate the precipitation of the S' phase and avoid the adverse effect of grain boundary precipitation on the properties of these materials.

To accelerate the S' precipitation, plastic deformation prior to artificial aging is usually employed. The present study indicates that a high density of vacancy clusters in Al-Li-Cu-Mg alloys after long time natural aging can also promote the S' precipitation. In addition, the S' precipitates formed at vacancy clusters are distributed more uniformly.

Hence, a study aimed on the improvement of mechanical properties of Al-Li-Cu-Mg alloys and composites by accelerating S' precipitation and avoiding grain boundary precipitation is suggested. In this future study, the effect of both pre-deformation and the introduction of high density of vacancies should be studied.

As the effect of grain boundary precipitation on mechanical properties can not be monitored by hardness changes, in this future work, tensile tests and fracture toughness tests are suggested.

2. {210} dislocation loop morphology

In the present study, an unusual {210} loop morphology was observed. Although it was suggested in the present study that this morphology was caused by loop rotation associated with the precipitation of the S' phase at these loops, experimental proof of this rotation is not available. A study aimed at the experimental proof of the loop rotation is suggested. Since the {210} loops were observed after 16 hour aging when the S' precipitation is already considerable, in the future study, dislocation loop orientation at earlier aging stages should be investigated. This way, the loop orientation before the S' precipitation can be observed. In addition, if the {210} loops are indeed caused by the rotation associated with the S' precipitation, it should be possible to observe the loops in the middle of the rotation process which could occur in the earlier stage of S' precipitation.

3. Relationship between GPB zone formation and plastic deformation

The relationship between the GPB zone formation and plastic deformation prior to aging is very controversial. In common with all the DSC results reported previously, the GPB zone formation peak diminished in materials containing a high dislocation density (both the composite and the

pre-deformed material) in the present study. Although the results in the present study suggested that the GPB zones are suppressed by deformation, a completely different mechanism, GPB acceleration by plastic deformation has been proposed in some previous studies. The conclusion on this issue depends on more detailed microstructural examination, including using electron diffraction and high resolution electron microscopy.

APPENDIX I

QUANTITATIVE ANALYSIS OF THE δ' PHASE IN THE 8090 ALLOY

The volume fraction of the δ' phase in the 8090 alloy was determined from measuring the number density and size of this phase at different aging times. The thickness of the imaged fields were determined by their thickness fringes under strict two beam condition. The procedure is described in the following:

First, the sizes of the δ' phase at different aging times were measured according to their diameter in CDF images. To decrease measuring error, those particles with very low intensity in CDFs were ignored because of the possibility of these precipitates being sectioned by sample surfaces. The average size, \bar{r} , of the δ' precipitates were determined according to equation (I-i):

$$\bar{r} = \frac{\sum r_i}{N} \quad (\text{I-i})$$

where r_i is the radius of each precipitate and N is the total number of the measured precipitates. A typical histogram of particle sizes is given in figure I-1.

Then, random lines (e.g., AB in figure I-2a) with certain length (l), were placed on CDF micrographs. Considering the characteristics of TEM, these random lines correspond to random planes in the samples examined (plane ABCD in figure I-2a). The area of these planes, $A = l \cdot h$ where h is the thickness of the samples. By counting the total number of intersections (N_t)

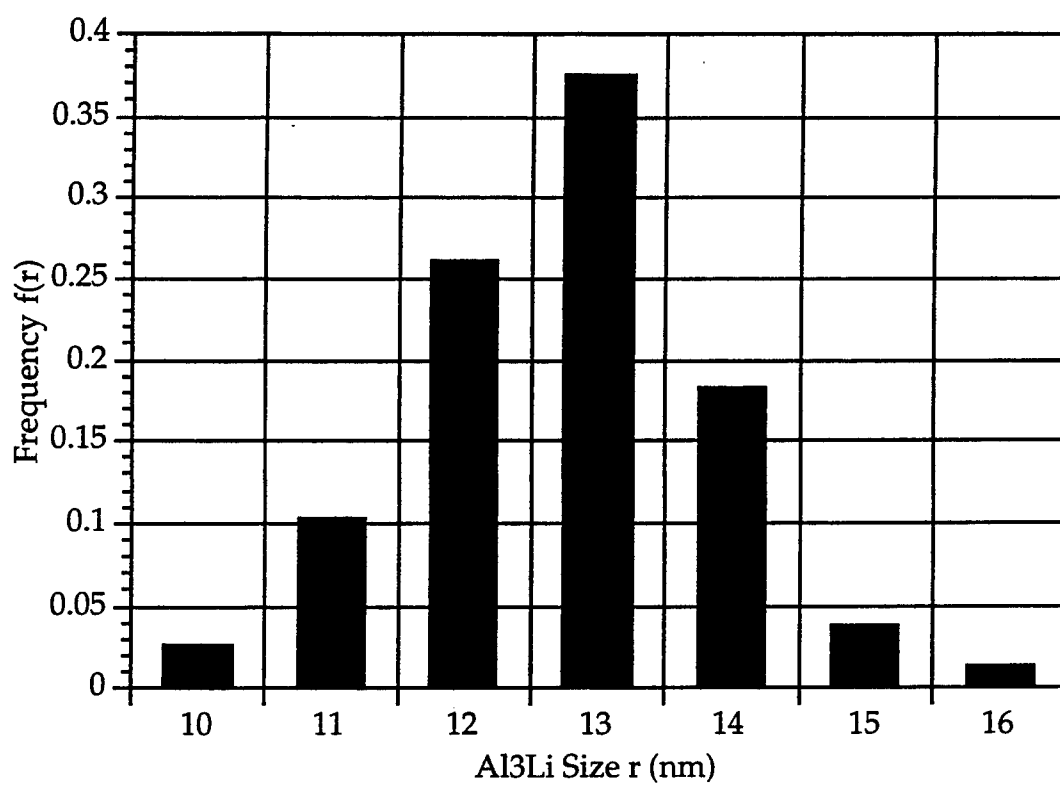
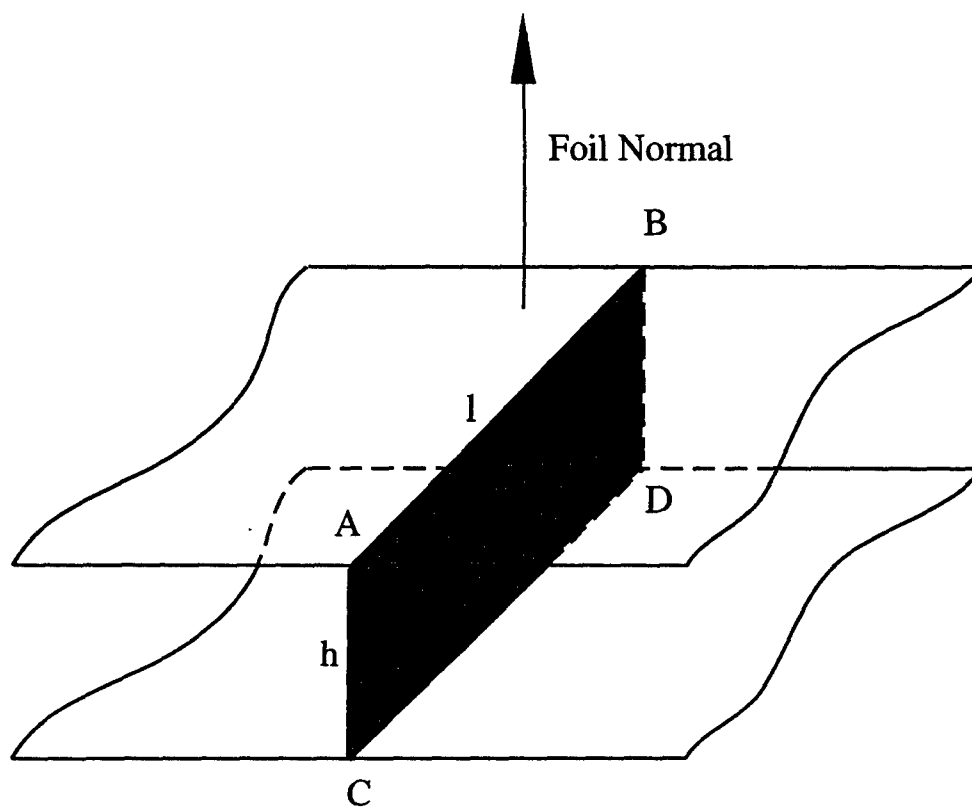
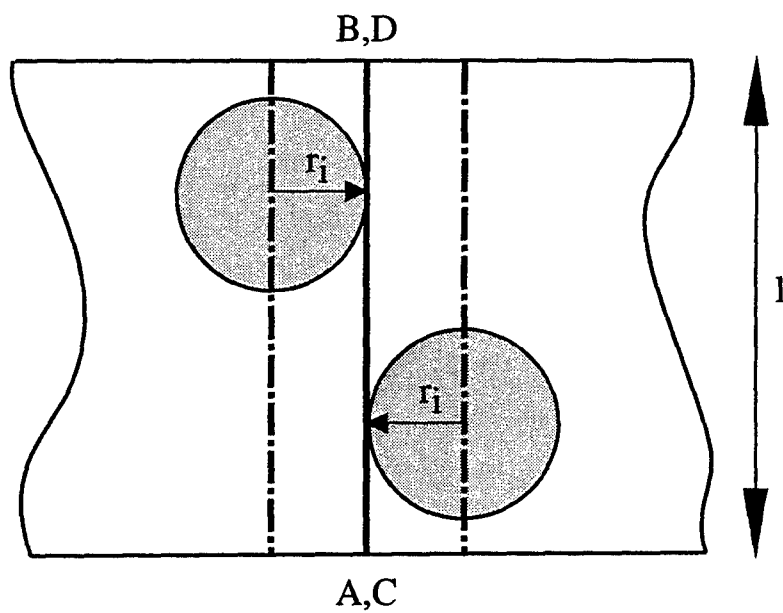


Figure I-1 δ' size distribution after 8 hour aging ($\bar{r} = 13$ nm)



(a)



(b)

Figure I-2 Illustration of the quantitative measurement of the δ' phase.

of the δ' precipitates with these random lines, the apparent area number density (N_A) can be obtained through equation (I-ii):

$$N_A = \frac{N_t}{l \cdot h} \quad (\text{I-ii})$$

Consider a particle size distribution in the form of a histogram (figure I-1), and a given bin which is centered on a radius r_i . Reference to figure I-2b shows that the precipitates in this size interval will intersect the analysis plane, if their centers are located within a distance of r_i of plane ABCD.

Consider now the bin for the smallest size interval which is centered on $r = r_1$. The number of precipitates, in this size interval, which intersect the analysis plane, per unit area, N_{A1} is:

$$N_{A1} = 2N_1 \cdot r_1 \quad (\text{I-iii})$$

where N_1 is the number of particles/unit volume for this size interval in bin 1. The factor of 2 is included because precipitates within a distance of r_1 will intersect the analysis plane (figure I-2b). If the bin width is Δ , then the number of precipitates in the section size interval, which intersect the analysis plane, is

$$N_{A2} = 2N_2 \cdot (r_1 + \Delta) = 2N \cdot r_2 \quad (\text{I-iv})$$

Hence, the total number of the precipitates which intersect the analysis plane per unit area (N_A) is

$$N_A = 2 N_1 \cdot r_1 + 2N_2 \cdot r_2 + 2 N_3 \cdot r_3 \dots\dots 2N_n \cdot r_n \quad (\text{I-v})$$

Equation (I-v) can be rewritten as

$$N_A = 2 \sum_{i=1}^{i=n} N_i \cdot r_i \quad (\text{I-vi})$$

Now, since we are considering unit volume:

$$\sum_{i=1}^{i=n} N_i = N_V \quad (\text{I-vii})$$

and

$$\frac{\sum_{i=1}^{i=n} N_i \cdot r_i}{\sum_{i=1}^{i=n} N_i} = \frac{\sum_{i=1}^{i=n} N_i \cdot r_i}{N_V} = \bar{\bar{r}} \quad (\text{I-viii})$$

Rearranging equation (I-viii) yields $\sum_{i=1}^{i=n} N_i \cdot r_i = \bar{\bar{r}} \cdot N_V$.

Equation (I-viii) now becomes

$$N_A = 2 \bar{\bar{r}} \cdot N_V \quad (\text{I-ix})$$

and the volume number density (N_V) of the δ' particles is

$$N_V = \frac{N_A}{2 \bar{\bar{r}}} \quad (\text{I-x})$$

The volume fraction of the δ' phase is

$$V_V = N_V \frac{4}{3} \pi \cdot r^3 \quad (\text{I-xi})$$

It is interesting to note that, as would be expected intuitively, the number of intersections per unit area (N_A) is given by the volume number density (N_V) times the average diameter of the δ' phase ($2\bar{\bar{r}}$), i.e., equation (I-ix).

APPENDIX II

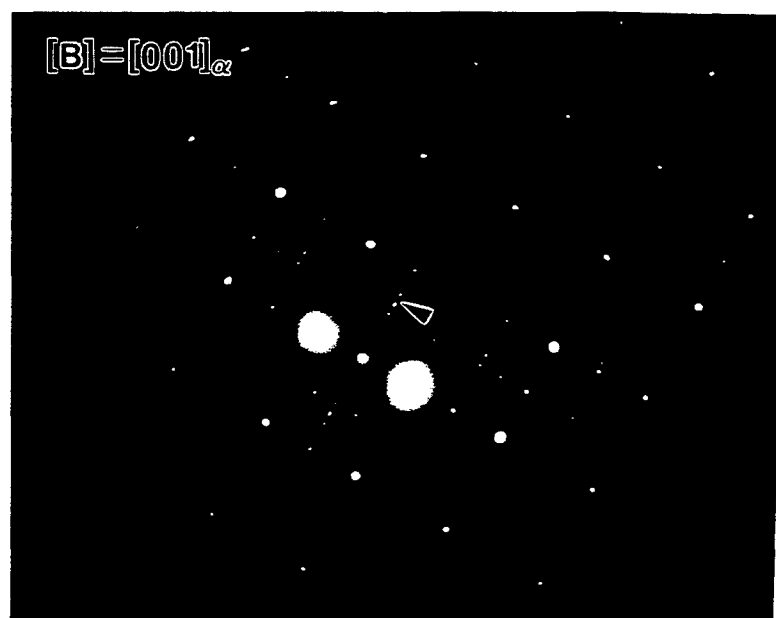
ELECTRON DIFFRACTION PATTERNS AND INDEXING OF THE S' PHASE

When employing the TEM, the crystal structure of a specific phase, such as the S' phase, is determined by indexing electron diffraction patterns. Because of the complex crystal structure and the multiple variants (12) of the S' phase, manual indexing of electron diffraction patterns is very difficult. In the present study, the indexing of S' diffraction patterns and the confirmation of the existence of the phase were assisted by a computer software Diffract 1.12v.

Figure II-1a shows a CDF image of the S' phase after 120 hour aging. The selected area diffraction pattern from figure II-1a is shown in figure II-1b. The beam direction for figures II-1a and b is very close to $[B]=[100]_{\alpha}$. As shown in figure II-1a, at least two groups (which may contain as many as 8 variants) of S' precipitates exist in the area imaged, lying with their a axes normal to each other. As a consequence, the periodicity of the precipitate diffraction pattern (figure II-1b) is very complicated. By using computer simulation software Diffract 1.12v, after inputting crystal structural information of the S' phase (refer to table 3.2 in Chapter 3) and the 12 orientation of the S' phase with respect to the α matrix listed in table 2.2, SAD patterns with known beam directions were easily simulated. Figure II-2 is a simulated SAD pattern with beam direction parallel to $[100]_{\alpha}$. Since in figure II-1a, only two groups of S' laths, whose a axes are normal to the beam direction, can be seen, the pattern

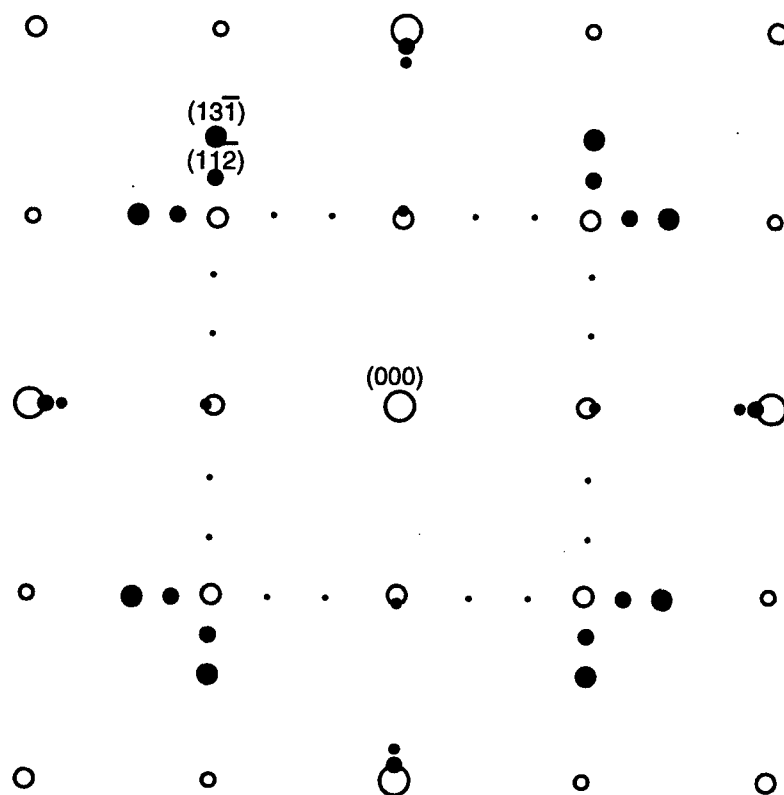


(a) S' CDF



(b) SAD pattern, $R_d = 24.5 \text{ mm}\text{\AA}$. The arrowed reflections are indexed as $(13\bar{1})$ and $(11\bar{2})$ in figure II-2

Figure II-1 S' laths from groups I and II, which lie perpendicular to the beam direction, and the corresponding SAD pattern.



○ Matrix and Al_3Li reflections

● S' reflections

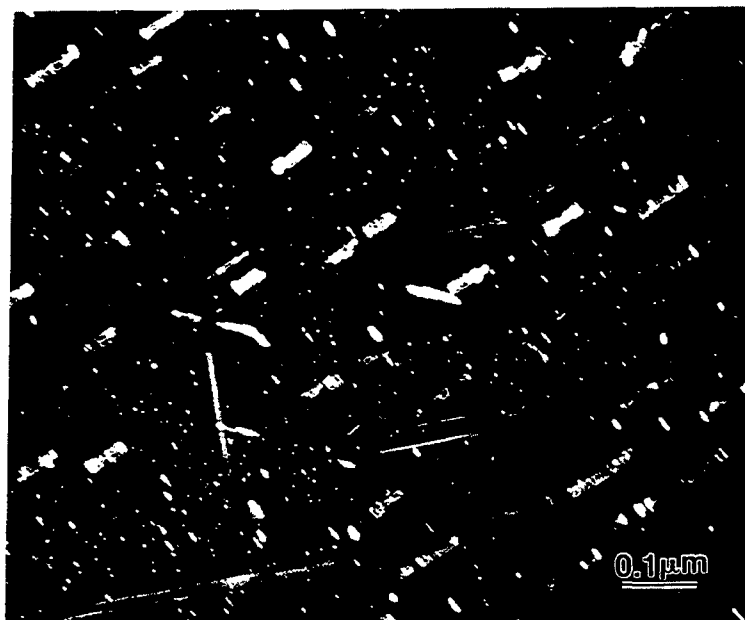
$R_d = 100 \text{ mm}\text{\AA}$, $[\text{B}] = [001]_\alpha$.

Figure II-2 Simulated SAD pattern of S' laths including 8 variants lying normal to beam direction.

in figure II-2 was simulated only considering the existence of the 8 variants of S' belonging to these two groups. Also included in this simulated SAD pattern is the δ' phase. Comparing figure II-1b with figure II-2, it can be seen that figure II-1b contains the reflections from both the δ' and S' phases. The arrowed reflections in figure II-1b were used to form the CDF image in figure II-1a and are the $(13\bar{1})$ and $(11\bar{2})$ reflections from the S' phase.

In the S' CDF image, figure II-3a, in addition to the S' laths which are similar to those in figure II-1a, the S' precipitates from the third group, which have their a axes parallel to the beam direction, can also be seen as dots or short rods. The designation A, B, and C are used to indicate that they belong to types A, B and C S' precipitates, respectively. Figure II-3b is the SAD pattern from the area shown in figure II-3a and the arrowed reflection was used to form the CDF image in figure II-3a. Because the precipitates in figure II-3a include all the 3 groups, 12 variants of S' in the material, an SAD pattern containing all the 12 variants of S' precipitates was simulated, as shown in figure II-4. By comparing this simulated pattern with figure II-2, those reflections from the group whose a axis is parallel to the beam direction can be easily identified. This comparison of figure II-3b with figure II-4 indicates that the reflection arrowed in figure II-3b is $(0\bar{4}0)_{S'}$ and it is from the group which has the a axis parallel to the beam direction.

All the S' diffraction patterns presented earlier in the text were indexed in a similar way described here.



(a) CDF image

(b) SAD pattern from the area shown above, $R_d = 24.5 \text{ mm}\text{\AA}$

Figure II-3 S' precipitates from all the 3 orientation groups.

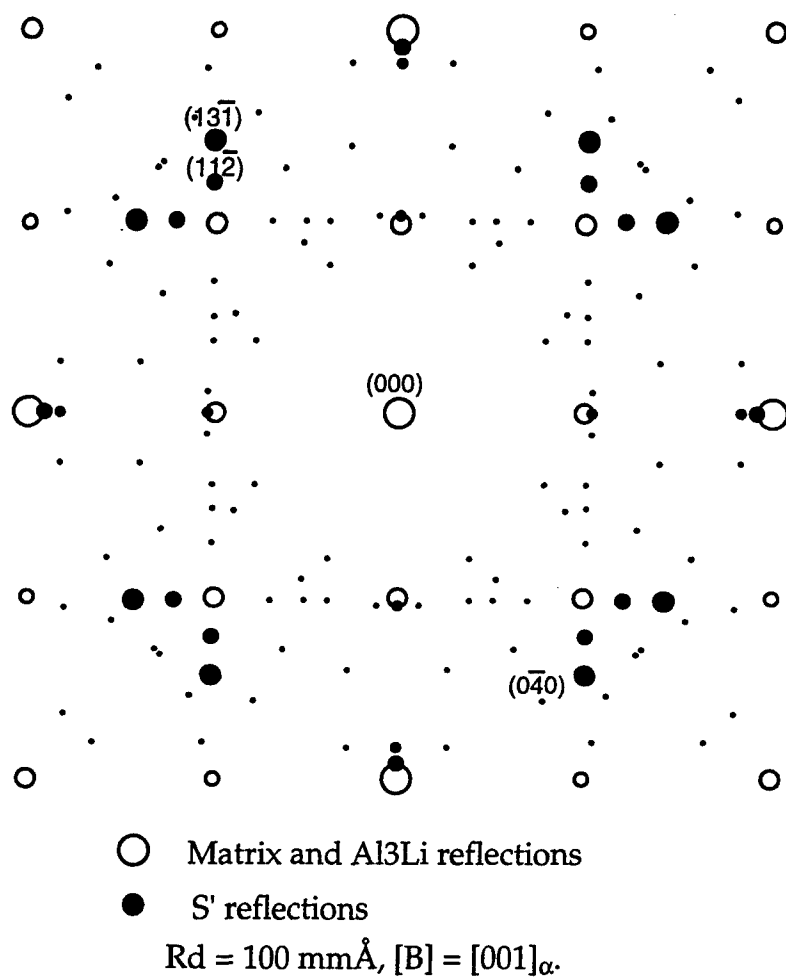


Figure II-4 Simulated SAD pattern of S' laths including all the 12 variants.
 (131) and (112) are from group I and II. (040) is from group III.

APPENDIX III

TRACE ANALYSIS

For the determination of e.g., loop planes, trace analysis was employed. In all cases, the beam direction $[B]$ was close to $[001]_{\alpha}$. This frequently required the beam to be tilted such that the foil normal $[N]$ was not parallel to $[B]$. However, this did not present projection problems as shown below.

Figure III-1 is a schematic drawing of the relationships between the sample, the three $\langle 100 \rangle$ directions and the plane of projection (the image plane). The foil normal $[N]$ is shown at some arbitrary angle to the beam direction $[001]$. The (001) plane is indicated by the bold lines and the $[100]$ and $[010]$ directions are also indicated. Because the (001) plane in the foil is parallel to the projection plane, then two of the three $\langle 001 \rangle$ directions will be contained in the image plane whereas the third is perpendicular to the image plane. This means that in an $[001]$ orientation, 2 of the 3 S' groups (table 2.2) will have their growth directions (the a axis) contained within the plane of projection whereas the third group will have their growth direction perpendicular to the image plane. Hence, the S' laths can be used to orient the image.

Consider a plane of the form $\{hk0\}$ in figure III-2. The projection of the direction $\langle hk0 \rangle$ is $\langle hk0 \rangle$, and the "upright" $\{hk0\}$ plane will project as a line (the trace of the $\{hk0\}$ plane) which is perpendicular to $\langle hk0 \rangle$. Hence, any loop which lies on an $\{hk0\}$ plane will project as a line which preserves its orientation relative to the $\{001\}$ planes in the sample. Hence, measurement

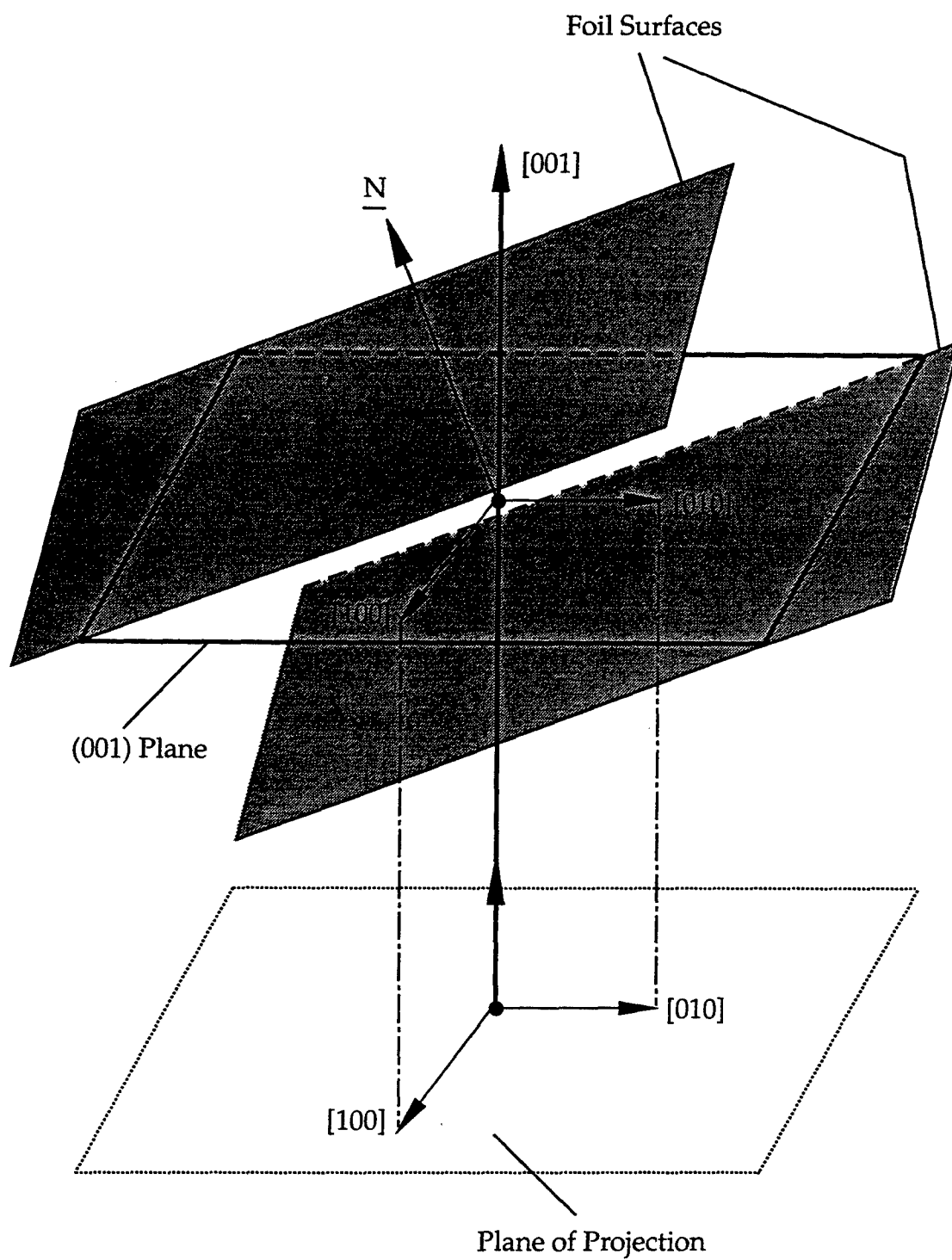


Figure III-1 Relationship between $\langle 100 \rangle$ projections and the plane of projection with $[B] = [001]$.

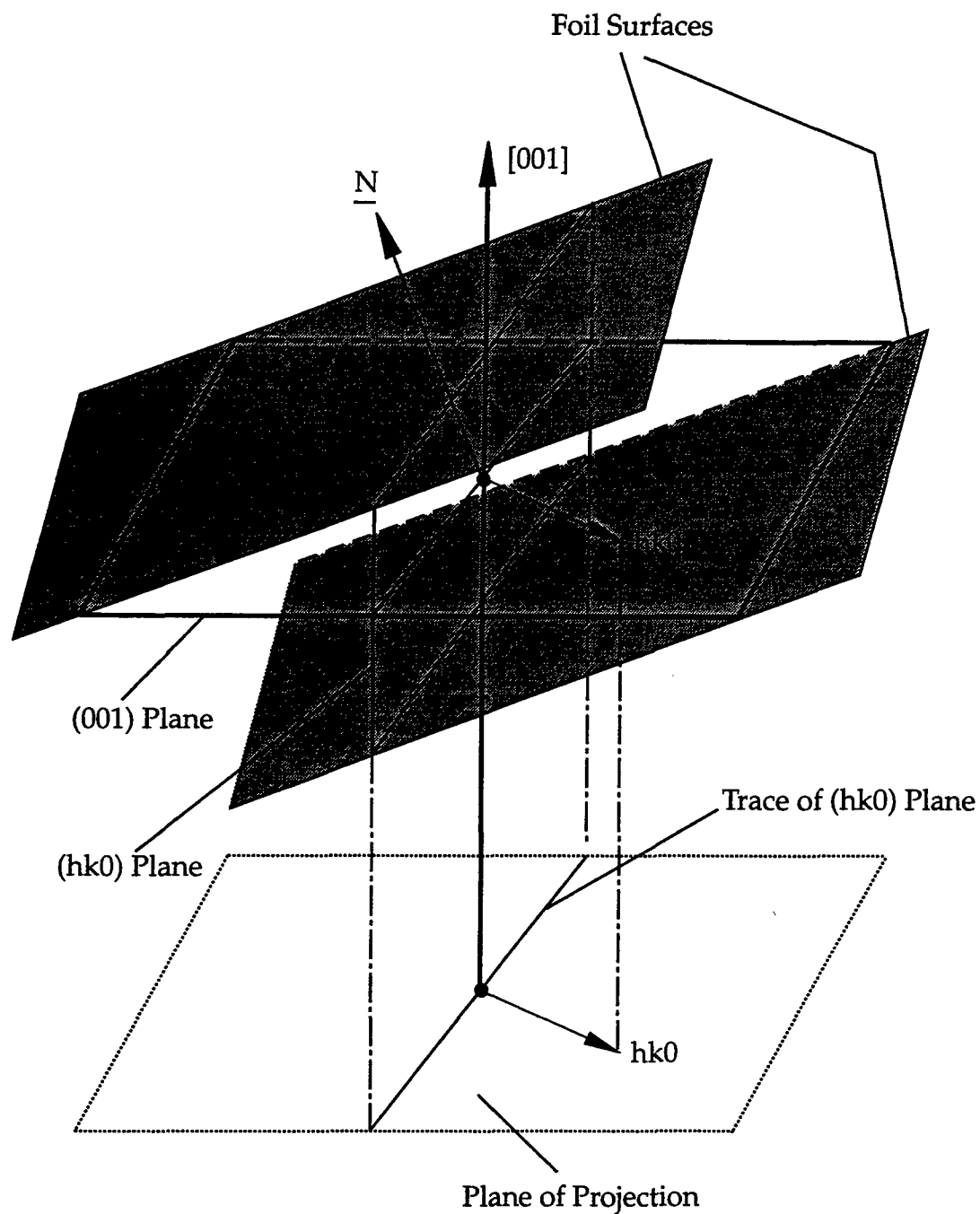
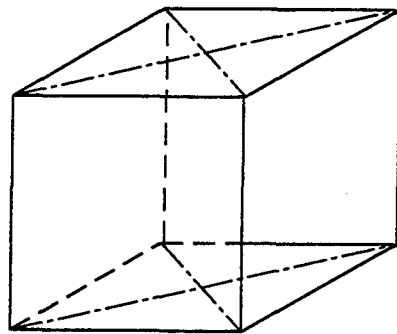


Figure III-2 Relationship between $\{hk0\}$ and $\langle hk0 \rangle$ projections and the plane of projection with $[B] = [001]$.

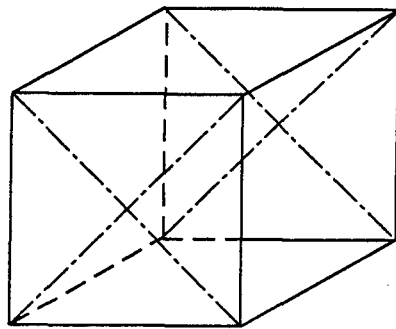
of the angle between $(hk0)$ and e.g., $[100]$ will uniquely describe the orientation of e.g., a loop plane.

It has been pointed out earlier that the dislocation loops in figure 3.14 do not appear to lie on $\{110\}$ planes. Detailed analysis is presented in the following:

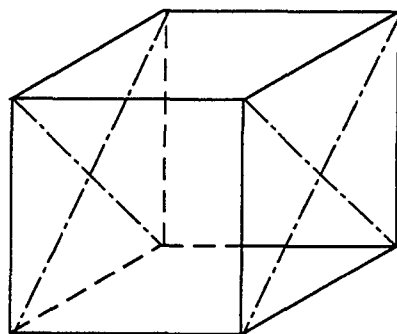
As shown in figures III-3a - c, the $\{110\}$ planes have 6 possible orientations. Dislocation loops always tend to be circular because of the line tension. If dislocation loops lie on the $\{110\}_\alpha$ planes, with an $[001]_\alpha$ beam direction, the projections of the loops on these $\{110\}_\alpha$ planes will be as shown in figure III-4a. That is, they are either projected as short rods parallel to $[110]_\alpha$ or $[1\bar{1}0]_\alpha$ (when lying on $(110)_\alpha$ or $(1\bar{1}0)_\alpha$ planes) or ellipses with their long axis parallel to the $[100]_\alpha$ (when lying on $(011)_\alpha$ and $(01\bar{1})_\alpha$ planes) or $[010]_\alpha$ directions (when lying on $(101)_\alpha$ and $(10\bar{1})_\alpha$ planes). However, the dislocation loops in figure 3.14 are oriented as shown in figure III-4b, which have the long axes of the ellipses parallel to the $[110]$ direction. Therefore, these loops must be in the zone $[110]$ and will be lying on $\{11L\}_\alpha$ planes where L does not equal to 0. That is, they do not lie on $\{110\}_\alpha$ planes.



(a) (110) and $(1\bar{1}0)$ planes

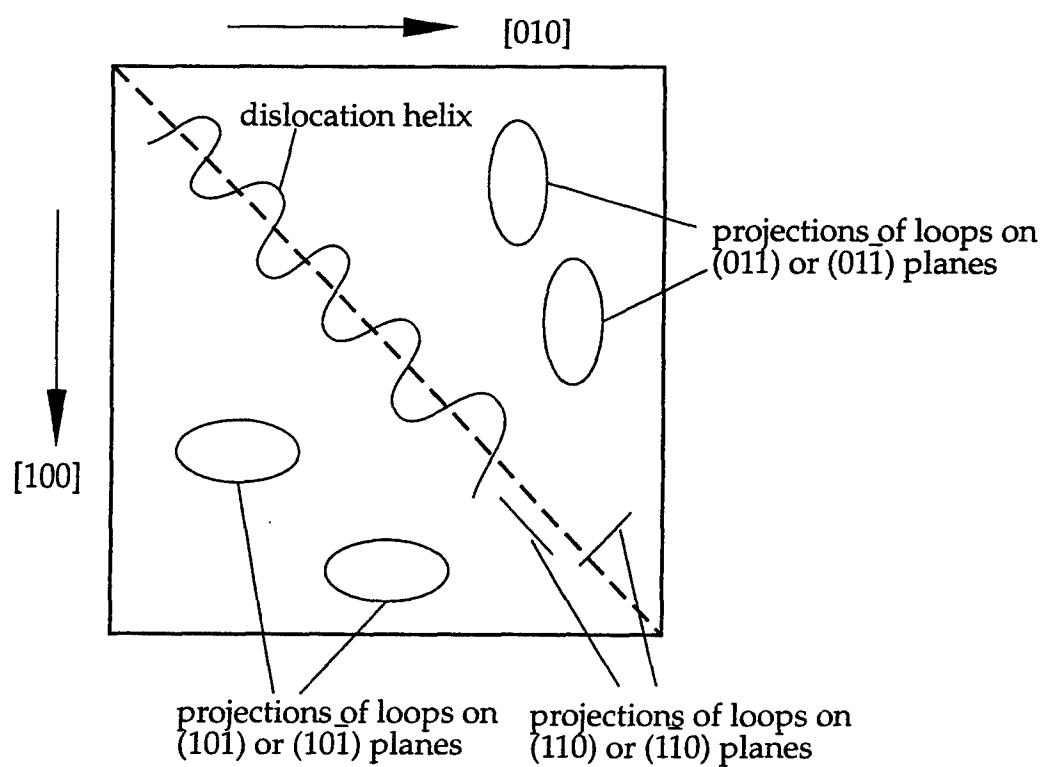


(b) (011) and $(01\bar{1})$ planes

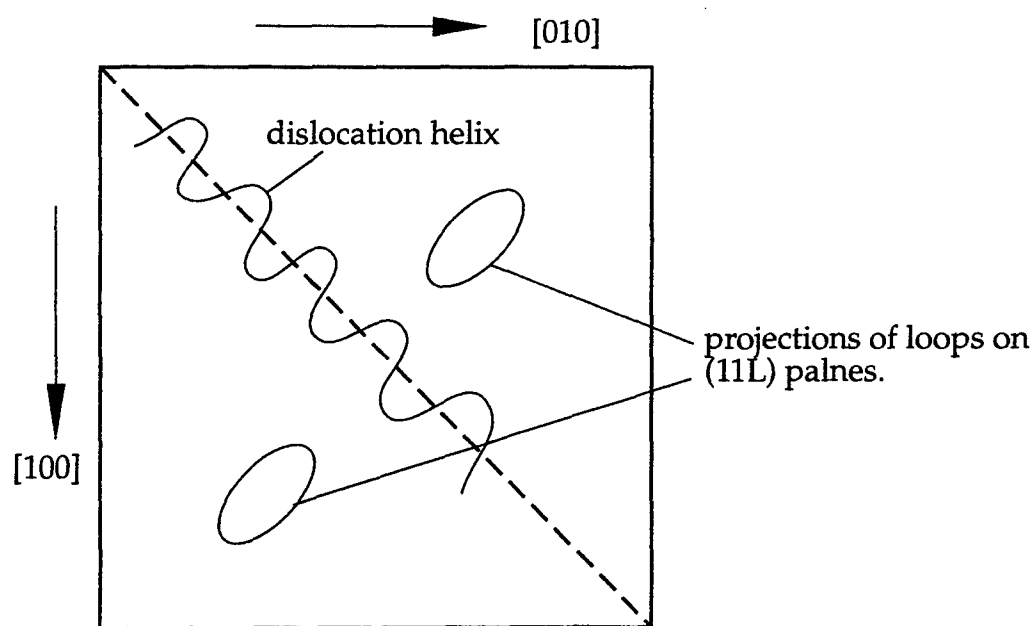


(c) (101) and $(10\bar{1})$ planes

Figure III-3 $\{110\}$ plane orientation.



(a)



(b)

Figure III-4 Projection orientation relationship of dislocation loops on $\{110\}$ planes and $\{11L\}$ planes. $[B] = [001]$

VITA

Xiaoli Tang was born [REDACTED] She received her Bachelor's degree in Engineering from Wuhan Institute of Hydraulic and Electric Engineering, Hubei, China, in July 1982, and her Master's degree in Engineering from University of Science and Technology, Beijing, China, in December 1985. She was a lecturer in Beijing Polytechnic University, Beijing, China, from December 1985 to July 1990. She then went to The Pennsylvania State University to pursue her Ph.D. in Materials Science and Engineering. Xiaoli Tang is a joint student member of ASM/TMS. Her scholarly publications are listed as follows:

- X. Tang and P. R. Howell, "A Quantitative Study of the δ' (Al₃Li) Phase in an Al-Li-Cu-Mg-Zr Alloy", *Solid to Solid Phase Transformations in Inorganic Materials*, TMS-AIME, Warrendale, PA, 1994, p285.
- X. Tang and P. R. Howell, "A Microstructural Study of the Dislocation and Precipitation Distributions in an Al-Li-SiC Composite during Aging at 190°C", *Developments and Applications of Ceramics and New Metal Alloys - Proc. International Symposium*, Quebec City, Quebec, Canada, Aug. 29 - Sept. 2, 1993, p157.
- X. Tang and P. R. Howell, "Microstructural Development of a Spray Formed Aluminum/Lithium/SiC Composite during Aging - Preliminary Report", *Proc. American Society for Composites - 7th Technical Conference*, University Park, PA, Oct. 13-15, 1992, p22.
- X. Tang, M. H. Tosten and P. R. Howell, "The Precipitation of Plate-like Phases in Al-Based and other Alloys", *Proc. 3rd International Conference on Aluminum Alloys - Their Physical and Mechanical Properties*, NTH/SINTEF, Norway, June 22 - 26, Vol.II, 1992, p3.
- Y. Zuo, D. Qiu and X. Tang, "The Application of Microcomputers in the Heat Treatment of Steels", *Electronic Technology (in Chinese)*, No.3, 1990, p36.